



MSc Thesis Mechanical Engineering

Integrating sensor and material modeling to interpret eddy current sensor readings.

Wiard van der Weijden

Supervisors: dr. Habil. C. Soyarslan, dr.ir. R. van Tijum,
prof.dr.ir. A.H. van den Boogaard, dr.ing. A. Nijhuis

May 22, 2023

Department of Nonlinear Solid Mechanics
Faculty of Engineering Technology,
High Tech Systems and Materials

Preface

The work presented in this thesis was carried out between 15th of September 2022 and the 15th of May 2023.

I would like to thank all those who have contributed. Most of all, I want to thank Celal Soyarslan for the seas of time he spend helping me as well as his continuous enthousiasm about my research. It is no exagerration to say many parts of this thesis would not be there without him. Second, I want to thank my second supervisor Redmer van Tijum who acted as the voice of reason. Redmer helped a lot in deciding on the direction and approach of the thesis. Third, I want to thank Egge Rouwhorst and Peter Bax for helping me understand and survive the world of Electromagnetism. Fourth, I want to thank the rest of my colleagues at Philips Drachten for the good times at the office. Fifth, I want to thank Ton van den Boogaard for his help with contacting other people in the field. Sixth, I want to thank Lars-Erik Miedema from KME for the copper samples used in the experiments. Seventh, I want to thank Jos Havinga for suggesting the research topic to me and bringing me into contact with Philips. Eighth, I want tTo thank Arend Nijhuis for making time for providing help in providing feedback on the electromagnetic part.

Finally, I just want to say a short thank you to my family who supported me throughout the thesis. When progress was not so smooth their support meant a lot.

Enschede, May 2023

Wiard van der Weijden

Contents

1. Introduction	3
1.1. Non-destructive testing	3
1.2. Literature and motivation	4
1.3. Goal and outline of the thesis	4
I. Electromagnetic analysis	7
2. Sensor analysis	9
2.1. Introduction	9
2.2. The working principle of the eddy current sensor	9
2.3. Electromagnetic field equations for low-frequency time-harmonic eddy currents	10
2.4. Finite element model details	11
2.5. Winding homogenization	13
2.6. Sensor output computation	13
2.6.1. Definitions	13
2.6.2. Implementation	15
2.6.2.1. Energy method	15
2.6.2.2. Alternative methods	17
2.6.3. Discretization	18
2.6.3.1. Energy method	18
2.6.3.2. Alternative methods	19
2.6.4. Validation	19
2.7. Sensor signal interpretation	20
2.8. Validation cases	21
2.8.1. No strip	21
2.8.2. Copper strips	21
2.8.3. AISI 420 strips	21
2.9. Field line distributions	23
2.10. Parameter studies	26
2.10.1. Eddy current mode results	26
2.10.2. Permeance results	28
2.11. Summary	29
3. Magnetic homogenization	31
3.1. Introduction	31
3.2. Micromagnetic properties	31
3.3. RVE creation	32
3.4. Homogenization theory	32
3.5. Results	34

II. Mechanics	35
4. Mechanical homogenization	37
4.1. Introduction	37
4.2. Micromechanical properties	37
4.3. RVE creation	38
4.4. Homogenization theory	40
4.5. Effect of carbides on mechanical properties	41
4.6. Effect of stress on magnetic properties	43
4.6.1. Domain wall theory	43
4.6.2. Interpreting inductance during cyclic loading	45
4.7. Summary	48
III. Correlations and discussions	49
5. Correlations	51
5.1. Magnetic to mechanical	51
5.2. Conclusion	52
5.3. Future research	53
. Literature	54
A. Validation	61
A.1. Benchmark 1: Two coils in free space	61
A.2. Benchmark 2: Sensor	62
B. Discretization of inductance computations	65
B.1. Flux method	65
B.2. Electric field method	68
B.3. Current method	69
C. High frequent theoretical inductance calculations	72
C.1. Theoretic expression self-inductance	72
C.2. Theoretic expression mutual inductance	73
D. Low frequent theoretical inductance calculations	75
D.1. Mutual inductance	75
D.2. Self inductance	75
E. Anti-symmetry test	77
F. Phasor notation	78
F.1. Phasor derivation	78
F.2. Power derivation	78
G. The electrical circuit	80
G.1. The hardware	80
G.2. Deriving the transfer function	81
H. Fitting simulated curves	82

Abstract

The demand for recycled metals is growing exponentially, making it imperative for industries to adapt to sustainable practices. However, the use of recycled metals can pose challenges due to their unpredictable behavior. To address this, significant efforts have been made in the field of Eddy Current testing to monitor the material properties of recycled metals. Nonetheless, interpreting Eddy Current sensor signals to estimate the mechanical properties remains a challenge. Previous studies have focused on individual aspects of Eddy Current testing, such as magnetic homogenization or coil winding modeling, without providing a comprehensive framework to relate the sensor signal to the mechanical properties of the sheet. The primary objective of this thesis is to present a modeling framework that relates the Eddy Current sensor signal to the mechanical properties of the sheet. Achieving this objective entails a detailed study of inductance calculations and Eddy Current sensor modeling. The models developed in this study are validated with experiments and used to describe the relationship between the sensor signal and the magnetic properties of the sheet. In addition, the study employs mechanical and magnetic homogenization techniques to investigate the relationship between the magnetic and mechanical properties of AISI420. By providing a comprehensive framework for relating Eddy Current sensor signals to mechanical properties, this study addresses a significant challenge faced by industries seeking to use recycled metals. The proposed models and techniques have the potential to revolutionize the field of Eddy Current testing and provide a more sustainable approach to the use of metals in industrial applications.

1. Introduction

1.1 Non-destructive testing

In recent years, there has been a significant push to use recycled metals in manufacturing. The use of recycled metals can reduce production costs and the environmental footprint. However, recycled materials often contain higher levels of impurities, leading to less predictable material behavior. This lack of predictability can pose significant problems for many industries because processing parameters need to be calibrated for each incoming batch of material. For instance, Philips Drachten produces shaving caps with very strict specifications on geometrical tolerances. The deep drawing dies are designed to meet these tolerances for specific incoming sheets with certain properties. Deviations in material properties affect each processing step during deep drawing, making it difficult to predict the resulting geometry [1]. Therefore, monitoring incoming materials is crucial to maintain consistent product quality.



Figure 1.1: The deep drawing process of the shaving caps in Philips Drachten.

Conventional methods to characterize materials, such as transmission electron microscopy, scanning electron microscopy, optical microscopy, tensile testing, and hardness testing [2], have significant limitations, including high manual labor, small sample sizes, and slow feedback time. Given these limitations, extensive research has been conducted on inline non-destructive testing [NDT] methods. A well worded description of inline NDT is given in [3]: "*Evaluation of material determined completely autonomously utilizing the test electronics requiring no operator intervention/interaction once the system has been set up.*" Ultrasonic testing, x-ray radiographic testing, and eddy current testing are among the

most commonly used inline NDT methods [4]. This thesis focuses on the eddy current sensor, which is the only sensor capable of determining magnetic permeability and conductivity [4]. By measuring these properties, the microstructure can be characterised, revealing information about the mechanical properties. Figure 1.2 illustrates this concept.

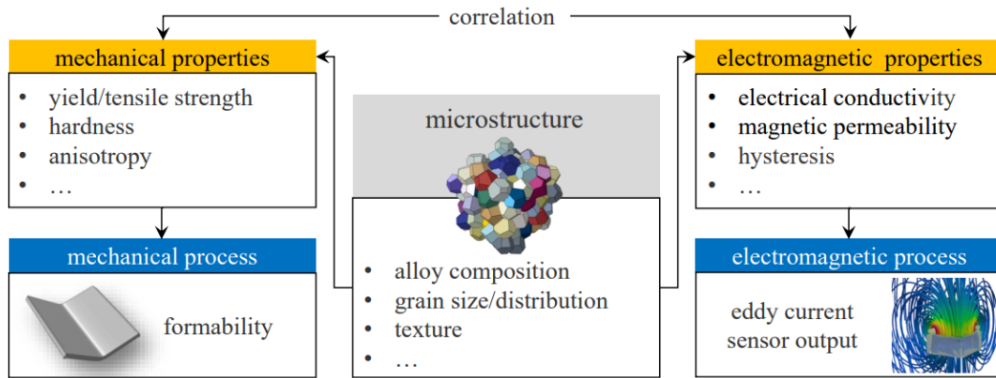


Figure 1.2: An illustration of the playing field of the research, reproduced from [5].

1.2 Literature and motivation

Several introductory books on magnetization have been written, including those by R. Bozorth [6], S. Chikazumi [7] and B. D. Cullity [8]. Besides these introductory books, an overview of the other relevant works will be given including their limitations. Several studies have discussed inductance computations, as demonstrated in [9] [10] [11] [12] [13] [14]. However, none of these papers address the determination of the real and imaginary parts of self and mutual inductance. Similarly, there are several works on eddy current sensor modeling, including those presented in [12] [13] [15] [16] [17] [18] [19]. There are two missing aspects in these works. The first aspect is an experimental validation of the complex behavior of mutual inductance at high frequencies. The second aspect, is the inverse fitting of the sensor response to obtain the magnetic permeability and conductivity of the sheet. Furthermore, there are numerous papers discussing the magnetic homogenization [5] [20] and mechanical homogenization [21] [22] [23]. However, the combined mechanical and magnetic homogenization required to establish a relationship between mechanical and magnetic properties has not been adequately addressed. Finally, the Villari reversals during cyclic loading have been frequently studied, as shown in [24] [25] [26] [27]. Nevertheless, crystal plasticity simulations are missing to support the theories described in these studies. This paper aims to address these gaps in the literature.

1.3 Goal and outline of the thesis

The purpose of this thesis is to provide a framework for relating the mechanical properties to the measurements by the eddy current sensor. To do this, several mechanisms in the magnetic and mechanical domain are studied on both micro and macro-scale. The start of the thesis will focus on the macroscopic modeling of the sensor to relate the measured curve to the permeability and conductivity of the sheet. This is followed by a study on the micro

scale to investigate how the permeability depends on the microstructure. In the subsequent part of the thesis, a study is conducted on the relationship between the microstructure and the mechanical properties. A small side step will be made where it is studied what happens during cyclic loading. The final part of the thesis brings together the findings from the previous sections, presenting a relationship between microscopic mechanical and magnetic properties while also summarizing all other relationships discovered during the research. The contributions made throughout this work are listed below.

- With regards to macroscopic eddy current modeling: (i) A derivation, implementation and validation of several inductance calculations in EM-FE [Electromagnetic - Finite Element] simulations is performed. (ii) An EM-FE model is described to simulate the measured inductance. The model is validated with experimental measurements. (iii) The eddy current sensor response has been simulated for many different sheet properties. The results can be used to relate the characteristics of the inductance curve to the permeability and conductivity of the sheet.
- Mechanical and magnetic homogenization are used to show the relation between magnetic and mechanical properties.
- The thesis presents full-field crystal plasticity finite element simulations to support the theories on Villari reversals during cyclic loading.

The research conducted in this thesis provides valuable insight into the relationship between mechanical and magnetic properties, particularly in the context of eddy current measurements. These findings can help improve the accuracy and efficiency of non-destructive testing techniques in the field of mechanical engineering.

Part I.

Electromagnetic analysis

2. Sensor analysis

2.1 Introduction

The upcoming chapter delves into the electromagnetic finite element model of the sensor, starting with Sections 2.2 to 2.6. These sections thoroughly discuss the model's boundary conditions, coil homogenization, and inductance calculation, emphasizing their importance in the accurate representation of the sensor's behavior. In Section 2.7 an electrical circuit is described that can be used to interpret the inductance curve. Moving forward, Section 2.8 provides a comparative analysis of the experimental results with those obtained from the EM-FE model. The objective is to assess the model's accuracy and limitations. Finally, Sections 2.9 and 2.10 unveil the outcomes obtained using the sensor model. These sections discuss the magnetic field lines, as well as the effects of width, thickness, conductivity, and permeability on the inductance.

2.2 The working principle of the eddy current sensor

Figure 2.1 illustrates the working principle of eddy current sensors. A current is imposed on a transmitting coil, creating a magnetic field (blue arrow). This leads to eddy currents in the sheet beneath the sensor (dotted black lines). The eddy currents create a new magnetic field (red arrow) that opposes the initial field. The resulting magnetic field is measured by the receiver coil. The magnitude of the magnetic field depends on the conductivity and magnetic permeability of the sheet.

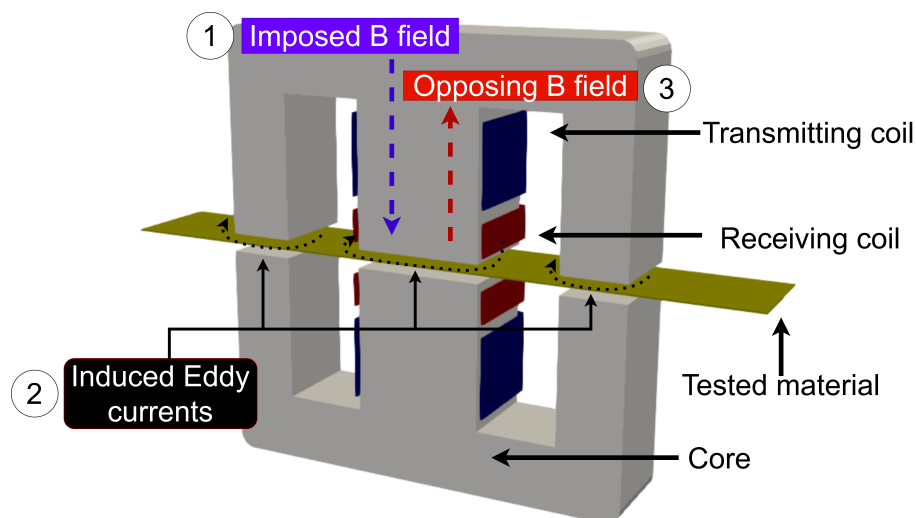


Figure 2.1: An illustration of the principle behind eddy current sensors.

The two transmitting coils can be used in two different modes. In the first mode, the transmitting coils create a magnetic field in the same direction. This is called the eddy current mode because it creates eddy currents in the material that oppose the applied magnetic field. This mode is generally used to measure the influence of eddy currents and high-frequency phenomena. In the second mode, the coils create opposing magnetic fields. This causes the magnetic flux to be parallel to the sheet. The sensor response is thus mainly related to the permeability of the material. This is called the permeance mode and is mainly used at lower frequencies. An overview of the magnetic flux directions in both modes is given in Figure 2.2. It should be noted that only coils 1A, 1B, 3A and 3B are used during the experiments in this thesis.

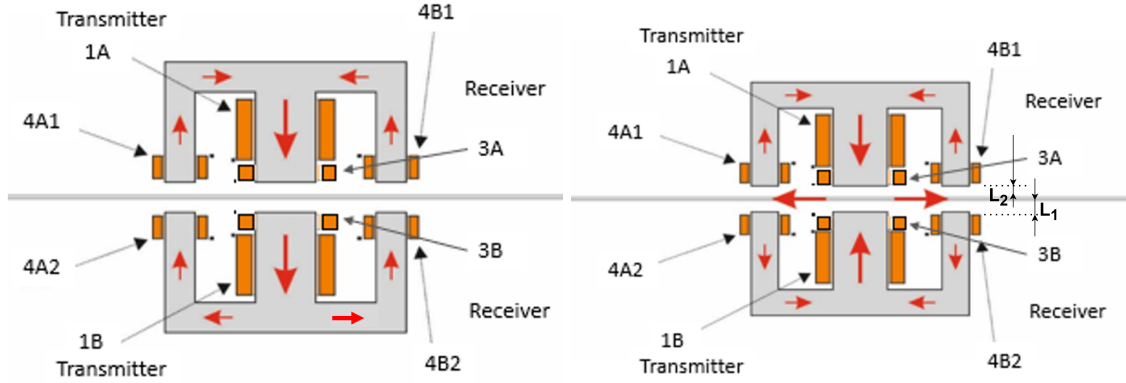


Figure 2.2: The direction of the magnetic field in the EC mode (left). The direction of the magnetic field in the permeance mode (right), reproduced from [28]. The transmitting coils are 1A and 1B. The receiving coils are 3A, 3B, 4A1, 4A2, 4B1 and 4B2.

2.3 Electromagnetic field equations for low-frequency time-harmonic eddy currents

Before any postprocessing calculations are carried out, a brief overview of the theory and assumptions in EM-FE simulations is provided. Let the problem domain be represented by material points $\mathbf{x} = x_i \mathbf{e}_i$, where \mathbf{e}_i for $i = 1, 2, 3$ denote Cartesian basis vectors and Einstein's summation convention is used. In the context of time-dependent phenomena, the electromagnetic field can be represented by four vector fields: the electric field intensity $\mathbf{E}(\mathbf{x}, t)$, the electric flux density $\mathbf{D}(\mathbf{x}, t)$, the magnetic field density $\mathbf{H}(\mathbf{x}, t)$, and the magnetic flux density $\mathbf{B}(\mathbf{x}, t)$. In addition, consider the electric current density $\mathbf{J}(\mathbf{x}, t)$ and the scalar electric charge density $\rho(\mathbf{x}, t)$. Considering that ∇ gives the gradient operator and “ \cdot ” and “ \times ” respectively denote scalar and cross products, two independent Maxwell's equations relating these time- and space-varying electromagnetic fields can be chosen as follows [29, 30]

$$\nabla \times \mathbf{E} = -\frac{d\mathbf{B}}{dt}, \quad (2.1)$$

$$\nabla \times \mathbf{H} = \frac{d\mathbf{D}}{dt} + \mathbf{J}, \quad (2.2)$$

Eqs. (2.1,2.2) correspond to Faraday's law and Maxwell-Amp'ere law, respectively. Both equations will be expressed in terms of the magnetic vector potential, \mathbf{A} . Equation (2.1)

can be rewritten by defining the magnetic vector potential as $\mathbf{B} = \nabla \times \mathbf{A}$ and applying Ohm's law, $\mathbf{J} = -\sigma \cdot \mathbf{E}$, which gives

$$\mathbf{J} = -\sigma \cdot \frac{d\mathbf{A}}{dt}. \quad (2.3)$$

In this thesis time harmonic fields are considered in which case all fields can be rewritten in terms of their phasors. A detailed derivation and explanation of phasors is given in Section 2.6.1. In short a phasor is the complex amplitude of a time harmonic expression. Expressing Equation 2.3 in terms of the phasor and utilizing Equation 2.12 gives

$$\tilde{\mathbf{J}} = -\sigma \cdot \tilde{\mathbf{A}}\omega i. \quad (2.4)$$

Where $\tilde{\mathbf{J}}$ and $\tilde{\mathbf{A}}$ are the phasors of \mathbf{J} and \mathbf{A} . In a low-frequency time-harmonic eddy current problem, the electric current density field admits an additive decomposition in an induced part, $\tilde{\mathbf{J}}_e$, and an impressed part, $\tilde{\mathbf{J}}_{\text{imp}}$. This can be used together with (2.4) to obtain

$$\tilde{\mathbf{J}} = \tilde{\mathbf{J}}_e + \tilde{\mathbf{J}}_{\text{imp}} = -\sigma \cdot \tilde{\mathbf{A}}\omega i + \tilde{\mathbf{J}}_{\text{imp}}. \quad (2.5)$$

The next step is to rewrite (2.2). The initial step in this process is to disregard the displacement current term, $d\mathbf{D}/dt$. This is a critical assumption since the displacement current is responsible for the observed capacitance [31]. Disregarding this term leads to a substantial discrepancy between the theoretical and experimental results at higher frequencies, as will be discussed in detail later in this study. Nonetheless, this assumption is prevalent in all commercial finite element eddy current analysis methods, such as Ansys, Abaqus, and Comsol, and is thus deemed acceptable. After omitting the displacement current term and applying $\tilde{\mathbf{B}} = \mu \cdot \tilde{\mathbf{H}}$, as well as substituting (2.5), Equation (2.2) may be restructured as follows

$$\nabla \times [\mu^{-1} \cdot \nabla \times \tilde{\mathbf{A}}] + i\omega \sigma \cdot \tilde{\mathbf{A}} = \tilde{\mathbf{J}}_{\text{imp}}. \quad (2.6)$$

Multiplying both sides by a virtual magnetic vector potential term $d\tilde{\mathbf{A}}$, and integrating over the volume with the application of standard tensor calculus operations result in the following variational form

$$\begin{aligned} \int_{\mathcal{V}} \nabla \times d\tilde{\mathbf{A}} \cdot [\mu^{-1} \cdot \nabla \times \tilde{\mathbf{A}}] dV + i\omega \int_{\mathcal{V}} d\tilde{\mathbf{A}} \cdot \sigma \cdot \tilde{\mathbf{A}} dV \\ = \int_{\mathcal{V}} d\tilde{\mathbf{A}} \cdot \tilde{\mathbf{J}}_{\text{imp}} dV + \int_{\partial\mathcal{V}} d\tilde{\mathbf{A}} \cdot \tilde{\mathbf{K}} dS, \end{aligned} \quad (2.7)$$

where $\tilde{\mathbf{K}}$ represents the tangential surface current density. Note that the variational form given in Eq. (2.7) considers the complex magnetic vector potential $\tilde{\mathbf{A}}$ and its real (in-phase) and imaginary (out-of-phase) components. This enables the derivation of other field variables and sensor data output, such as the phase of inductance.

2.4 Finite element model details

The simulations of the sensor are performed using the time-harmonic eddy current analysis in Abaqus Electromagnetic. It should be noted that doing simulations in this environment

has some important limitations. First of all, the displacement currents are neglected. This means that capacitance can not be taken into account. Secondly, magnetic hysteresis cannot be defined for the material, which is only possible in transient eddy current analysis. To reduce the number of elements, symmetry is used to model the sensor, employing one-eighth of the model, as shown in Figure 2.3.

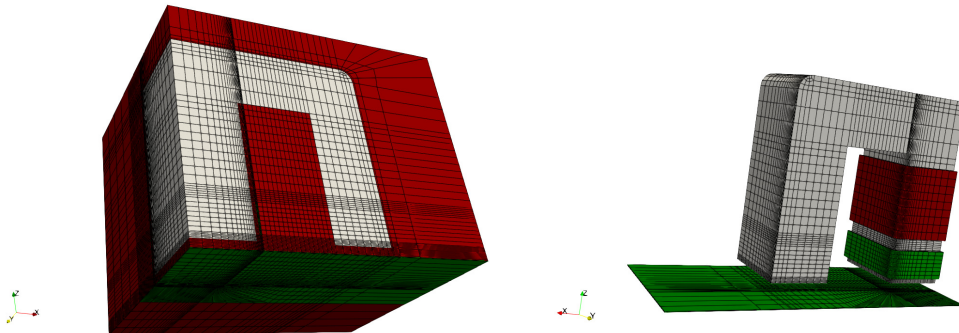


Figure 2.3: The mesh of the model used in the simulations. It can be recognized only one-eighth of the sensor is modeled.

It is crucial to define appropriate boundary conditions to account for the use of symmetry. On the one hand, for the permeance mode, the magnetic potential for each surface can be set to zero. The reason is that in each plane there is either symmetry or the magnetic field has decayed far enough. On the other hand, for the eddy current mode, there is anti-symmetry between the coils. A good description of anti-symmetry and symmetry conditions is given in [32]. An overview of the electric and magnetic fields near the surface is given in Table 2.1. In this table \parallel relates to the tangential component and \perp to the

Table 2.1: The electrical and magnetic field near symmetric and anti-symmetric boundary conditions.

	E_{\perp}	E_{\parallel}	B_{\perp}	B_{\parallel}
Symmetry	free	zero	zero	free
Anti-symmetry	zero	free	free	zero

perpendicular component. Anti-symmetric boundary conditions can be defined in Abaqus by defining no boundary condition for that surface. In Appendix E it is shown this results in anti-symmetry.

It should be noted that the symmetry assumptions are not fully accurate. In the actual sensor set-up the sheet rests on a supporting surface which is at the same height for each measurement. Consequently, for thicker sheets, they will be positioned closer to one ferrite core than the other, as is evident from L_1 being smaller than L_2 in Figure 2.2. Another simplification is done on the horizontal position, which is in reality not exactly in the center of the sensor. Empirical observations indicate that the horizontal position affects the measurement significantly. Hence, the horizontal alignment of the sheet is carefully managed to ensure accuracy.

Apart from the boundary conditions, various parameters require careful consideration in the simulations. For the coils it is chosen to use a low conductivity. The reason is that otherwise the resistance used in the calculations for the voltage in Section 2.7 need to be corrected for the skin effect. This is not straightforward [33]. Rather than a conductivity

of 0 a conductivity of 1 S/m is used which allows calculating the inductance using the current method, see Section 2.6. The relative permeability of the core that is used is 3000 based on the data sheet of ferroxcube 3C95. The conductivity of the core is 0.2 [S/m] as can be seen on the datasheet of ferroxcube 3C95. The permeability of the sheet varies per simulation, the conductivity is set at 2×10^{-6} based on conductivity measurements. An overview of the used parameters is shown in Table 2.2.

Table 2.2: The parameters used during the simulation.

	Transmitter	Receiver	Core	Air	Sheet
Relative permeability	1	1	3000	1	varies
Conductivity	1	1	0.2	0	2×10^6

2.5 Winding homogenization

Due to the constraints on mesh size, it is often infeasible to model all individual windings of a coil. Thus, the common practice is to consider the coil as a homogeneous sheet with a specific current density [34]. The current density is chosen to match that in real experiments and is calculated using

$$J = I_{\text{experiment}} N_{\text{windings}} / A_{\text{cross-section}}. \quad (2.8)$$

It should be noted that three important effects are ignored when modeling the coil as a homogeneous sheet. These effects are listed below.

- The proximity effect which is the redistribution of current towards the sides of the wires due to nearby windings. This effect is illustrated on the left side of Figure 2.4 as the large blue circles.
- The skin effect is the redistribution of the current density towards the surface of the wire. This is illustrated as the small blue circles on the left side in Figure 2.4.
- The capacitive effect is the interaction of electric fields of closely spaced conductors that leads to displacement currents between the coils.

These effects are illustrated on the right side of Figure 2.4. In [34] an extensive description is given of homogenization methods to include the proximity effects, skin effects, and capacitive effects. Many of the methods rely on modeling the discrete windings, obtaining an equivalent impedance and reluctivity, and then using this in the homogeneous coil. Implementing this into Abaqus electromagnetic is, however, not straightforward because assigning some equivalent impedance or complex conductivity is not readily available and should be implemented using user subroutines.

2.6 Sensor output computation

2.6.1 Definitions

Consider a coil that is subjected to a current placed near a magnetic and conductive medium, as depicted in the left side of Figure 2.5. When the current flows through the

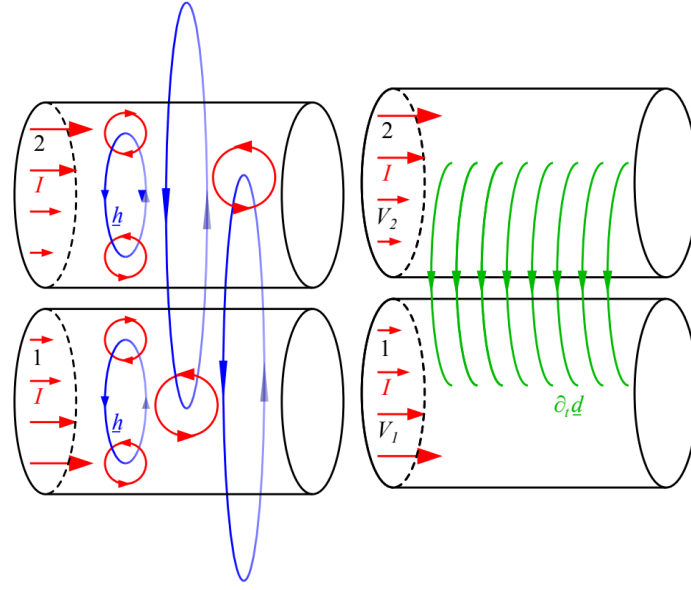


Figure 2.4: An illustration of the skin, proximity and capacitive effects, reproduced from [34]. $\delta_t \underline{d}$ is the electric charge displacement rate. \underline{h} is the magnetic field.

coil, the conductive medium induces eddy currents, which in turn cause an opposing voltage to develop in the coil. This phenomenon can be characterized by employing a complex inductance, denoted by \mathcal{L}_c , as illustrated in the center of Figure 2.5. The complex induc-

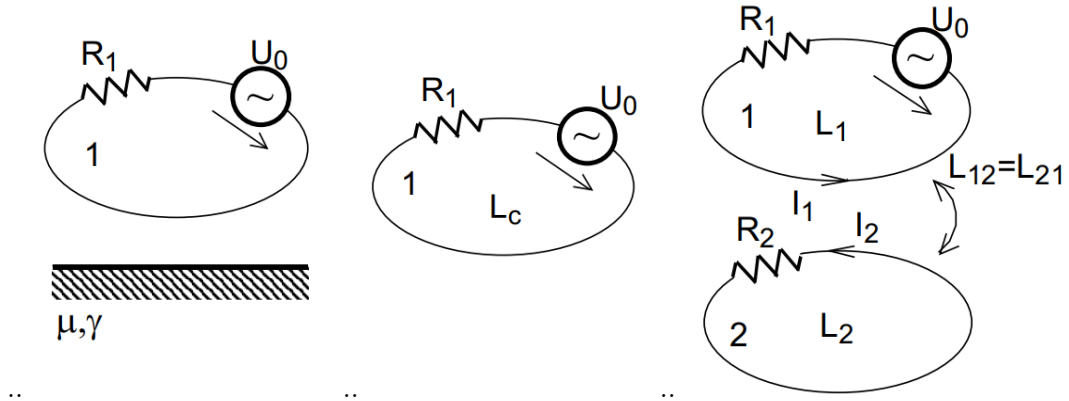


Figure 2.5: An illustration of some electric circuit, reproduced and modified from [35].

tance describes the relationship between the excitation current and the resulting voltage in the coil, expressed as follows

$$\mathcal{U}_{1c} = j\omega \mathcal{L}_c \mathcal{I}_1. \quad (2.9)$$

In eddy current testing, a slightly different scenario arises due to the presence of two coils, as shown on the right side of Figure 2.5. In this case, the complex mutual inductance, denoted by \mathcal{M}_c , is employed to describe the relationship between the current in the transmitting coil, \mathcal{I}_1 , and the voltage in the receiving coil, \mathcal{U}_{2c}

$$\mathcal{U}_{2c} = j\omega \mathcal{M}_c \mathcal{I}_1. \quad (2.10)$$

Since many of the variables used to calculate the inductance are time-harmonic, some notes regarding notation are in order. The notation adheres to the conventions described in [35] and [36]. Time-harmonic variables can be expressed in phasor notation as shown in Appendix F. An arbitrary variable \mathbf{X} can be expressed in phasor notation as follows

$$\mathbf{X}(x, y, z, t) = \text{Re} [\mathbf{X}_0(\mathbf{r})e^{j\alpha}e^{j\omega t}] = \text{Re} [\tilde{\mathbf{X}}(\mathbf{r})e^{j\omega t}]. \quad (2.11)$$

Here, $\tilde{\mathbf{X}}(\mathbf{r})$ represents the complex phasor, which is equal to $\mathbf{X}_0(\mathbf{r})e^{j\alpha}$. One of the advantages of phasor notation is that taking derivatives is straightforward, as shown below

$$\frac{d}{dt}\mathbf{X}(x, y, z, t) = \frac{d}{dt}\text{Re} [\tilde{\mathbf{X}}(\mathbf{r})e^{j\omega t}] = \text{Re} [\tilde{\mathbf{X}}(\mathbf{r})j\omega e^{j\omega t}]. \quad (2.12)$$

2.6.2 Implementation

2.6.2.1 Energy method

The inductance of a circuit can be calculated by comparing the power supplied by the circuit to the power consumed by the field. The power supplied by the circuit can be written analogous to the equation at the top of page 32 in [36].

$$P = \tilde{I} \cdot \tilde{I}^* (\mathcal{L}_{\text{re}j} - \mathcal{L}_{\text{im}}) \omega \quad (2.13)$$

Where \tilde{I} and \tilde{I}^* are the phasor of the current and the complex conjugate of the phasor of the current, respectively. The power consumed by the field, P_f , can be described by Equation 2.14. This is done analogous to Equation 1-68 in [36].

$$P_f = P_r + P_d + j2\omega(W_m + W_e) \quad (2.14)$$

Where P_r is the power leaving the region, P_d is the dissipated power, W_m is the power stored in the magnetic field and W_e is the electric energy of the field. In practice, P_r can be neglected since no power is leaving the domain. W_e can also be ignored as it is related to the capacitance, which is not considered in the simulations. The remaining variables, W_m and P_d can be calculated using Equation 2.15. It should be noted that these are the instantaneous power and energies as described under Equation 1-68 of [36].

$$P_d = \int \sigma |\mathbf{E}(\mathbf{r}, t)|^2 dV \quad \text{and} \quad W_m = \frac{1}{2} \int \mu |\mathbf{H}(\mathbf{r}, t)|^2 dV \quad (2.15)$$

The next goal will be to rewrite the time-dependent expressions in terms of their phasors. This rewriting is done in Section F.2. The result from this derivation shows that the expressions can be rewritten as

$$|\mathbf{E}(\mathbf{r}, t)|^2 = \frac{1}{2} [\tilde{\mathbf{E}} \cdot \tilde{\mathbf{E}}^*] \quad \text{and} \quad |\mathbf{H}(\mathbf{r}, t)|^2 = \frac{1}{2} [\tilde{\mathbf{H}} \cdot \tilde{\mathbf{H}}^*]. \quad (2.16)$$

Where $\tilde{\mathbf{E}}$ and $\tilde{\mathbf{H}}$ are the complex phasors of the electric field and applied magnetic field. When no magnetic hysteresis is considered, i.e., when conductivity and permeability are real, Equation 2.16 can be rewritten as

$$\sigma |\mathbf{E}(\mathbf{r}, t)|^2 = \frac{1}{2} [\tilde{\mathbf{J}} \cdot \tilde{\mathbf{E}}^*] \quad \text{and} \quad \mu |\mathbf{H}(\mathbf{r}, t)|^2 = \frac{1}{2} [\tilde{\mathbf{B}} \cdot \tilde{\mathbf{H}}^*]. \quad (2.17)$$

Combining Equations 2.13, 2.14, 2.15 and 2.17 gives the following equality

$$\tilde{I} \cdot \tilde{I}^* (\mathcal{L}_{re} j - \mathcal{L}_{im}) \omega = \int_{\tilde{\sim}} \tilde{\mathbf{J}} \cdot \tilde{\mathbf{E}}^* dV + 2j\omega \frac{1}{2} \int_{\tilde{\sim}} \tilde{\mathbf{B}} \cdot \tilde{\mathbf{H}}^* dV. \quad (2.18)$$

The two integral terms $\int_{\tilde{\sim}} \tilde{\mathbf{J}} \cdot \tilde{\mathbf{E}}^* dV$ and $\int_{\tilde{\sim}} \tilde{\mathbf{B}} \cdot \tilde{\mathbf{H}}^* dV$, are real, as can be confirmed by Equation 2.35. Using this property, the expressions for the real and imaginary inductance are obtained as

$$\mathcal{L}_{im} = -\frac{\int_{\tilde{\sim}} \tilde{\mathbf{J}} \cdot \tilde{\mathbf{E}}^* dV}{\omega \tilde{I} \cdot \tilde{I}^*} \quad \text{and} \quad \mathcal{L}_{re} = \frac{\int_{\tilde{\sim}} \tilde{\mathbf{B}} \cdot \tilde{\mathbf{H}}^* dV}{\tilde{I} \cdot \tilde{I}^*}. \quad (2.19)$$

The next step is to derive an expression for the mutual inductance. For the sake of simplicity, the expressions for the real part of the mutual inductance will be derived. It is assumed that no magnetic hysteresis is present, in which case the derivations can be taken from [37]. Consider a situation in which the transmitting coil is excited with a current \tilde{I}_1 and the receiving coil is excited with a current \tilde{I}_2 . The resulting energy of the circuits is given by Equation 2.20, which is taken from Equation 10 in [38]:

$$W = \frac{1}{2} \mathcal{L}_{11} \tilde{I}_1 \cdot \tilde{I}_1^* + \mathcal{M} \tilde{I}_1 \cdot \tilde{I}_2^* + \frac{1}{2} \mathcal{L}_{22} \tilde{I}_2 \cdot \tilde{I}_2^* \quad (2.20)$$

The next step is to examine the energy of the field. The total magnetic field, \mathbf{H} , is caused by the current in the transmitting and receiving coil. This can be decomposed into the magnetic field due to the current in the transmitting coil, \mathbf{H}_1 , and the current in the receiving coil, \mathbf{H}_2 . Similar to Equation 7 in Section 8.03 in [37], the expression for the energy of the field is given by

$$W_m = \frac{1}{2} \int \mu (\mathbf{H}_1 + \mathbf{H}_2) \cdot (\mathbf{H}_1 + \mathbf{H}_2) dV \quad (2.21)$$

$$W_m = \frac{1}{2} \mu \left(\int \mathbf{H}_1^2 dV + 2 \int \mathbf{H}_2 \cdot \mathbf{H}_1 dV + \int \mathbf{H}_2^2 dV \right) \quad (2.22)$$

Appendix F.2 can then be used to write the mutual energy of the magnetic field in terms of the phasors $\tilde{\mathbf{H}}_1$ and $\tilde{\mathbf{H}}_2$.

$$W_m = \frac{1}{2} \mu \left(\int \tilde{\mathbf{H}}_1^2 dV + 2 \int \tilde{\mathbf{H}}_2 \cdot \tilde{\mathbf{H}}_1 dV + \int \tilde{\mathbf{H}}_2^2 dV \right) \quad (2.23)$$

By comparing Equation 2.20 with Equation 2.22, the mutual energy terms can be identified as $\mathcal{M} \tilde{I}_1 \cdot \tilde{I}_2^*$ and $\int \tilde{\mathbf{H}}_2 \cdot \tilde{\mathbf{H}}_1 dV$ [37]. Using the principle of conservation of energy, the energy used by the field must be equal to the energy supplied by the circuit, resulting in Equation 2.24. Rewriting this equation and utilizing $\tilde{\mathbf{B}} = \mu \tilde{\mathbf{H}}$ gives Equation 2.25.

$$\mathcal{M}_{re} \tilde{I}_1 \cdot \tilde{I}_2^* = \mu \int \tilde{\mathbf{H}}_2 \cdot \tilde{\mathbf{H}}_1 dV \quad (2.24)$$

$$\mathcal{M}_{re} = \frac{\int \tilde{\mathbf{H}}_2 \cdot \tilde{\mathbf{B}}_1 dV}{\tilde{I}_1 \cdot \tilde{I}_2^*} \quad (2.25)$$

The same derivations can be performed to obtain the imaginary part of the mutual inductance. The resulting expression for the real and imaginary part of the self and mutual inductance are given by the following expressions.

$$\boxed{\mathcal{L}_{\text{re}} = \frac{\int \tilde{\mathbf{H}}_1 \cdot \tilde{\mathbf{B}}_1^* dV}{\tilde{I}_1 \cdot \tilde{I}_1^*}} \quad \text{and} \quad \boxed{\mathcal{M}_{\text{re}} = \frac{\int \tilde{\mathbf{H}}_2 \cdot \tilde{\mathbf{B}}_1^* dV}{\tilde{I}_1 \cdot \tilde{I}_2^*}}, \quad (2.26)$$

$$\boxed{\mathcal{L}_{\text{im}} = \frac{\int \tilde{\mathbf{E}}_1 \cdot \tilde{\mathbf{J}}_1^* dV}{\tilde{I}_1 \cdot \tilde{I}_1^*}} \quad \text{and} \quad \boxed{\mathcal{M}_{\text{im}} = \frac{\int \tilde{\mathbf{E}}_2 \cdot \tilde{\mathbf{J}}_1^* dV}{\omega \tilde{I}_1 \cdot \tilde{I}_2^*}}, \quad (2.27)$$

where $\tilde{\mathbf{H}}_2$ is the contribution of \tilde{I}_2 to the applied field, $\tilde{\mathbf{B}}_1$ is the contribution of \tilde{I}_1 to the magnetic field, $\tilde{\mathbf{E}}_2$ is the contribution of \tilde{I}_2 to the electric field and $\tilde{\mathbf{J}}_1$ is the contribution of \tilde{I}_1 to the current field. The resulting expressions will be referred to as the IEM in accordance with literature [39].

2.6.2.2 Alternative methods

The inductance can be calculated in several other ways. In all cases, the inductance can be related to the induced voltage using

$$\mathcal{L} = \frac{\tilde{\mathcal{U}}}{\tilde{I}\omega i} \quad (2.28)$$

In the next part, three different methods will be shown to obtain the voltage in the coil. In Figure 2.6 an overview is given of which domains the methods are integrated over.

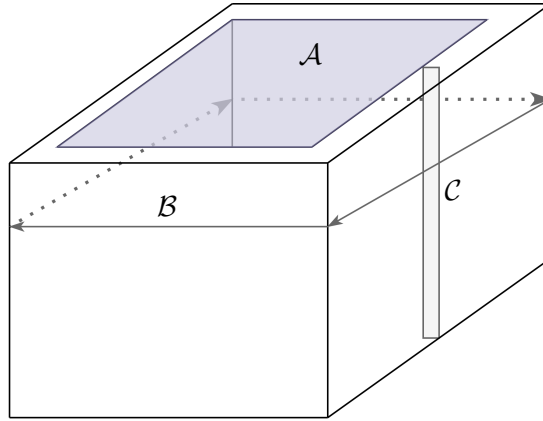


Figure 2.6: An overview of the domains of integration.

- The flux method which uses the magnetic field. Equation 2.29 follows directly from Faraday's law. The domain of integration is the volume inside of the coil and indicated as \mathcal{A} in Figure 2.6.

$$\tilde{\mathcal{U}} = -j\omega \int_{\mathcal{A}} \tilde{\mathbf{B}} \cdot d\mathbf{A}. \quad (2.29)$$

- The electric method which uses the electric field. Equation 2.30 follows from the definition of the voltage [40]. The domain of integration is a loop around the coil and indicated as \mathcal{B} in Figure 2.6.

$$\mathcal{U}_{\sim} = \int_{\mathcal{B}} \mathbf{E}_{\sim} \cdot d\mathbf{l} \quad (2.30)$$

- The current method which uses the current field. The voltage in the coil can also be defined using the current density as shown in Equation 2.31. The domain of integration is the cross-section of the coil and indicated as \mathcal{C} in Figure 2.6.

$$\mathcal{U}_{\sim} = R \int_{\mathcal{C}} \mathbf{J}_{\sim} \cdot d\mathbf{A} \quad (2.31)$$

2.6.3 Discretization

In this part it will be shown how the incremental energy method, flux method, electric method and current method can be implemented into EM-FE simulation software such as Abaqus.

2.6.3.1 Energy method

Below an example is given on how the imaginary part of the mutual inductance is calculated. The initial expression is given by Equation 2.27 and repeated below for convenience

$$\mathcal{M}_{\text{im}} = \frac{\int \mathbf{E}_2 \cdot \mathbf{J}_1^* dV}{\omega I_1 \cdot I_2^*} \quad (2.32)$$

Now some work will be done to rewrite the expression $\mathbf{E}_2 \cdot \mathbf{J}_1^*$. To do this the dot product rule $a \cdot b = b \cdot a$ is used together with $\mathbf{J} = \sigma \mathbf{E}$ which gives

$$\mathbf{E}_2 \cdot \mathbf{J}_1^* = [\mathbf{E}_2^{re} + j\mathbf{E}_2^{im}] \cdot [\mathbf{J}_1^{re} - j\mathbf{J}_1^{im}] \quad (2.33)$$

$$\mathbf{E}_2 \cdot \mathbf{J}_1^* = \mathbf{E}_2^{re} \cdot \mathbf{J}_1^{re} + j\mathbf{E}_2^{im} \cdot \mathbf{J}_1^{re} - j\mathbf{J}_1^{im} \cdot \mathbf{E}_2^{re} + \mathbf{E}_2^{im} \cdot \mathbf{J}_1^{im} \quad (2.34)$$

$$\mathbf{E}_2 \cdot \mathbf{J}_1^* = \mathbf{E}_2^{re} \cdot \mathbf{J}_1^{re} + \mathbf{E}_2^{im} \cdot \mathbf{J}_1^{im} \quad (2.35)$$

Discretizing the expression and writing out all the components of the field variables gives the expression for the mutual inductance that can be implemented into Abaqus.

$$\mathcal{M}_{\text{im}} = \sum_{i=0}^{N_{\text{el}}} \left(\left[\hat{J}_{12,i}^{re} \hat{E}_{11,i}^{re} + \hat{J}_{22,i}^{re} \hat{E}_{21,i}^{re} + \hat{J}_{32,i}^{re} \hat{E}_{31,i}^{re} \right] V_i \right) / \left(\omega I_1 \cdot I_2^* \right) \quad (2.36)$$

$$+ \sum_{i=0}^{N_{\text{el}}} \left(\left[\hat{J}_{12,i}^{im} \hat{E}_{11,i}^{im} + \hat{J}_{22,i}^{im} \hat{E}_{21,i}^{im} + \hat{J}_{32,i}^{im} \hat{E}_{31,i}^{im} \right] V_i \right) / \left(\omega I_1 \cdot I_2^* \right) \quad (2.37)$$

The subscripts are explained as follows, consider $E_{k,j,l}^{im}$, in this case, k refers to the component of the field (eg. if $k = 1$ it means that E_x is analyzed), j refers to the simulation in which coil number j is excited, l refers to the number of the element. Furthermore, N_{el} refers to the number of elements in the simulation.

2.6.3.2 Alternative methods

To implement the Flux, Electric, and Current methods into Abaqus the expressions in Equations 2.29, 2.30 and 2.31 are rewritten as summations of element volumes and field values. This makes implementation into Abaqus much easier as these variables are readily available. The full derivations are shown in Appendix B and the resulting expressions can be seen in Table 2.3. Where N_W is the number of windings, L_p is the coil perimeter, $N_{el,c}$

Table 2.3: The real part of the inductance, \mathcal{L}_{re} , and the imaginary part of the inductance, \mathcal{L}_{im} , for the current, flux and electric method.

Method	Expression	\mathcal{L}_{re}	\mathcal{L}_{im}
Flux	$A = \frac{N_W}{h_{coil}\mathcal{I}} \left[\sum_{j=1}^{N_{el,ic}} (B_j V_j) - \sum_{k=1}^{N_{el,c}} \left(\frac{t_{coil}-t_k}{t_{coil}} B_k V_k \right) \right]$	Re(A)	Im(A)
Electric	$A = \frac{L_p N_W}{N_{el,c} \omega \mathcal{I}} \sum_{j=1}^{N_{el,c}} E_{ ,j}$	Im(A)	Re(-A)
Current	$A = \frac{k_{sym} N_W}{\mathcal{I} A_C \sigma \omega} \sum_{j=1}^{N_{el,c}} J_{ ,j} V_j$	Im(A)	Re(-A)

is the number of elements in the coil, \mathcal{I} is the excitation current, h_{coil} is the axial depth of the coil, σ is the conductivity of the coil, ω is the radial frequency of excitation, A_C is the cross-sectional area of the coil, k_{sym} is the symmetry multiplier of the model and t_{coil} refers to the thickness of the coil. Furthermore, the subscript $||$ refers to the components of the field values parallel to the winding direction. Also, it should be noted that the summation over $B_j V_j$ is done over the elements inside the coil whereas the summation over $B_k V_k$ is done over the elements in the coil itself. The summations of the Electric and Current method are done over the elements in the coil. For all these methods the self inductance is calculated by performing the summation over the elements corresponding to the transmitting coil. The mutual inductance is determined by performing the summation over all elements relating to the receiving coil.

2.6.4 Validation

In order to evaluate the accuracy of the inductance calculation methods, a validation benchmark is employed. This benchmark involves the determination of mutual inductance for two free coils. The resulting curves are presented in Figure 2.7, which also includes the curve for the theoretically calculated inductance based on the analysis in Appendix D and C. As can be observed from the figure, all the methods yield accurate results. For a more comprehensive explanation, please refer to section A.1. Additionally, an investigation is carried out to examine the resulting inductance curves for the actual eddy current sensor simulation, as detailed in section A.2. It is found that all the inductance calculation methods provide comparable results when a high coil conductivity is employed. However, for a low coil conductivity in the model, significant differences are observed among the methods. Thus, caution should be exercised in selecting an appropriate inductance calculation method. In the rest of this work it is chosen to use the IEM method because this provides feasible results for a low coil conductivity and high stabilization factor. The coil

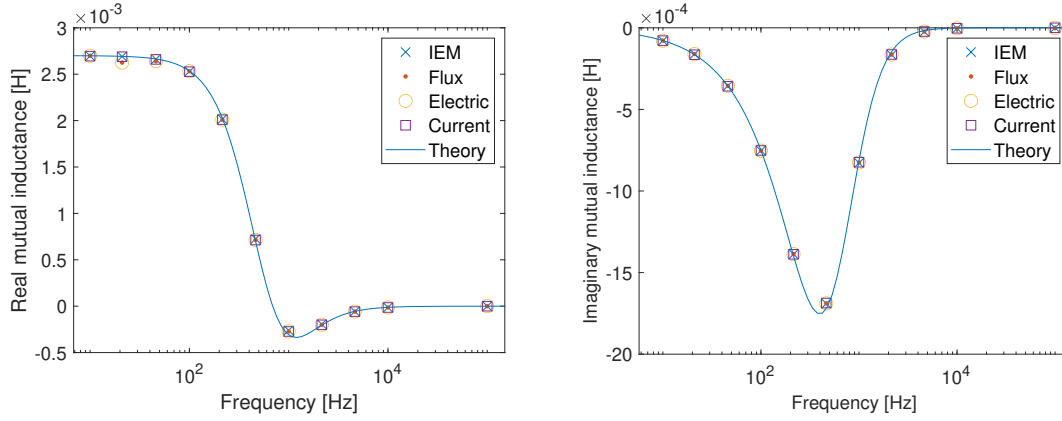


Figure 2.7: Figure showing the resulting values for the real and imaginary part of the mutual inductance calculated .

conductivity is set to 1 [S/m] to avoid skin effects in the coil as mentioned earlier. The stabilization factor is set to 1e6 to improve stability and solving speed.

2.7 Sensor signal interpretation

In the experiments used in this thesis the voltage in the receiver, \mathcal{U}_{rec} , and the current in the transmitter, \mathcal{I}_{ref} , are used to calculate the gain and phase of the inductance. The expressions for the phase and gain of the inductance are given in Equation 2.38 based on the derivations in Appendix I.

$$\left| \frac{\mathcal{U}_{\text{rec}}}{\mathcal{I}_{\text{ref}}} \right| = \mathcal{M}_c \quad \angle \mathcal{U}_{\text{rec}} - \angle \mathcal{I}_{\text{ref}} = \angle \mathcal{M}_c - 90 \quad (2.38)$$

It is emphasised that \mathcal{M}_c can be calculated using the derivations done in Section 2.6. In literature, many different models are available to describe the phase and gain in an eddy current sensor. However, often some resistance is assumed for the receiver [41]. In Table 6-1 in [15] two models for open circuits are mentioned, but these only consider non-ferromagnetic materials. For this reason, a previously developed model by Shiyu Zeng is used. This model is based on the simplified electrical circuit shown in Figure 2.8.

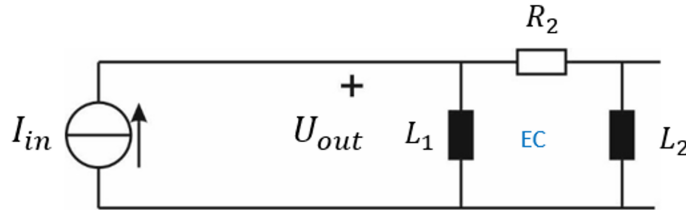


Figure 2.8: The electrical circuit as proposed by [28].

Based on derivations done in Section G.2 of the Appendix it can be shown that the gain and phase can be described by

$$\left| \frac{\mathcal{U}_{\text{rec}}}{\mathcal{I}_{\text{ref}}} \right| = j\omega \mathcal{L}_{11} \frac{1 + j\omega\tau_n}{1 + j\omega\tau_p} \quad \text{and} \quad \angle \mathcal{U}_{\text{rec}} - \angle \mathcal{I}_{\text{ref}} = \arctan \left(\frac{1 + \omega^2\tau_n\tau_p}{\omega(\tau_n - \tau_p)} \right), \quad (2.39)$$

where $\tau_n = \mathcal{L}_2/\mathcal{R}_2$ and $\tau_p = (\mathcal{L}_1 + \mathcal{L}_2)/\mathcal{R}_2$.

2.8 Validation cases

2.8.1 No strip

The first validation case is the sensor without a strip. The self inductance for the transmitting coil, $\mathcal{L}_{11,\text{trans}}$, and receiving coil, $\mathcal{L}_{11,\text{rec}}$, as well as the mutual inductance, \mathcal{M} , are shown in Table 2.4. As can be seen, there is a difference of approximately 10% between the model and experiments. This error can have different reasons such as mesh refinement but is acceptable.

Table 2.4: The measured and modeled self and mutual inductances.

	$\mathcal{L}_{11,\text{trans}}$ [μH]	$\mathcal{L}_{11,\text{rec}}$ [μH]	\mathcal{M} [μH]
Model	335.0	43.7	43.7
Experiment	359.5	43.1	40.5

2.8.2 Copper strips

The second validation case concerns the simulation of copper strips. The advantage of copper strips is that their relative permeability and conductivity are known quite precisely to be 1 and 58.14×10^6 [S/m], respectively. The experimental measurements are compared to the simulated results in Figure 2.9. It can be seen that the simulation matches the measurements relatively well. It should be noted that the match with experiments was only obtained after making some improvements to the experimental set-up which are discussed in Appendix G.1.

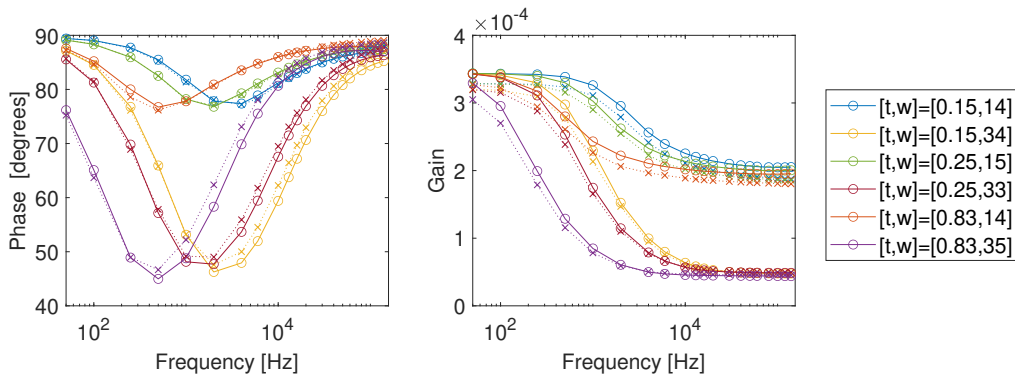


Figure 2.9: Comparison of the phase (left) and gain (right) from resulting from simulations and experiments. The experimentally measured curves are indicated by "x" markers. The simulated curves are indicated by "o" markers. The dimensions of the thickness and width and thickness in the legend are [mm].

2.8.3 AISI 420 strips

To test whether the model also provides reasonable results in case a ferromagnetic material is modeled two scenarios are analyzed. In the first scenario, the measured low frequent gain is compared to the simulated low frequent gain. This is shown in the left side of Figure

2.10. In the second scenario, the measured phase is compared to the simulated phase. The results can be seen on the right side of Figure 2.10. A relative permeability of 108.4, based on experiments performed by Egge Rouwhorst in [42], is used in all simulations. Examining the left side of Figure 2.10, an offset between the simulated and measured

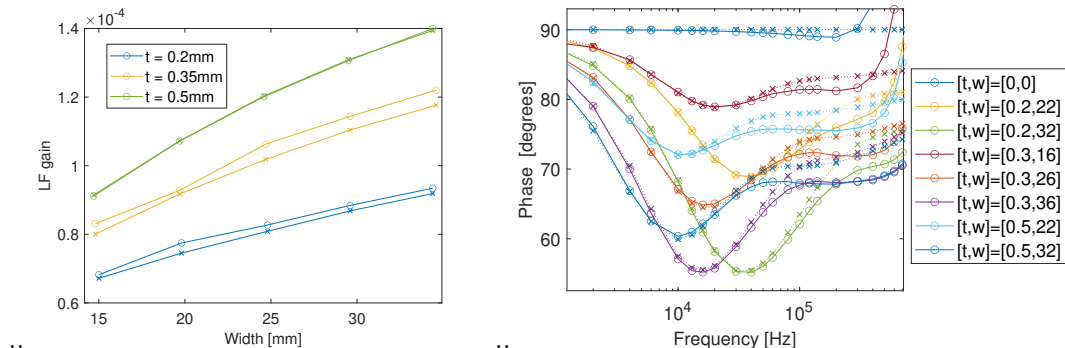


Figure 2.10: Comparison of the simulated low frequent gain ($-x$ marker) with the measured low frequent gain ($-o$ marker) (left). Comparison of the simulated phase ($-x$ marker) with the measured phase ($-o$ marker) (right). The dimensions of the thickness and width and thickness in the legend are [mm].

curves is observed for some thicknesses. This offset can be attributed to the fact that the relative permeability of 108.4 measured in [42] is specific to a strip from a certain coil. When a strip is taken from a different coil, the relative permeability will likely differ, resulting in slightly different measured gain. Furthermore, the right side of Figure 2.10 demonstrates that at higher frequencies, the match between simulation and experiment is not perfect, which is likely caused by capacitance [28]. Fortunately, at the frequency where the phase is minimum, the simulation matches experiments relatively well. This means this point can be used for further analysis.

It is important to note that the magnetization of the strip greatly influences the match between simulations and experiments. Three different magnetization treatments can be applied before measuring with the sensor: (i) as received, (ii) demagnetization, i.e., slowly moving the strip through an alternating field, and (iii) magnetization, i.e., keeping the strip in a field of constant strength. In the experiments in this work, demagnetization was performed using a decaying AC field. In Table 2.5 an overview is given on for which magnetization treatment the simulated phase and gain match with experiments. The de-

	As received	Demagnetized	Magnetized
Gain	yes	no	yes
Phase	yes	yes	yes

Table 2.5: Overview of for which magnetization treatment the simulations match with experiments.

viation between the measured gain and the simulated gain for the demagnetized samples can be explained by referring to the description in [43]. For low fields, the magnetic properties depend on the magnetic history because different demagnetization procedures result in varying domain structures at zero net magnetization. For example, demagnetization using decaying AC fields results in higher permeability compared to the permeability after thermal demagnetization or compared to the DC-permeability.

2.9 Field line distributions

In order to evaluate the validity of the sensor simulations, field line distributions for an eddy current mode simulation are presented for four different frequencies. The frequencies and corresponding phases are depicted in Figure 2.11. The field line plots are generated using

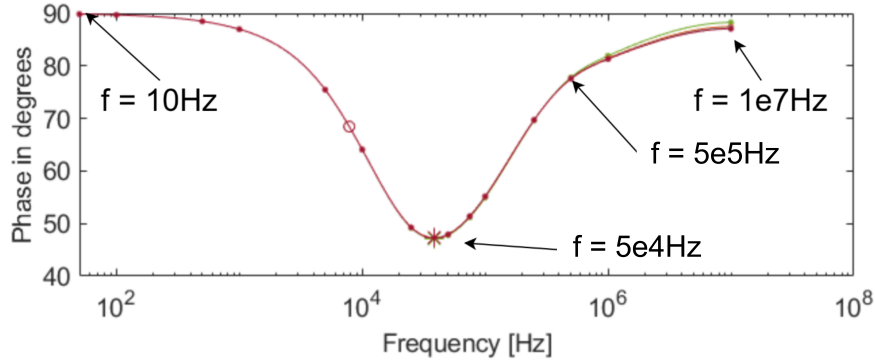
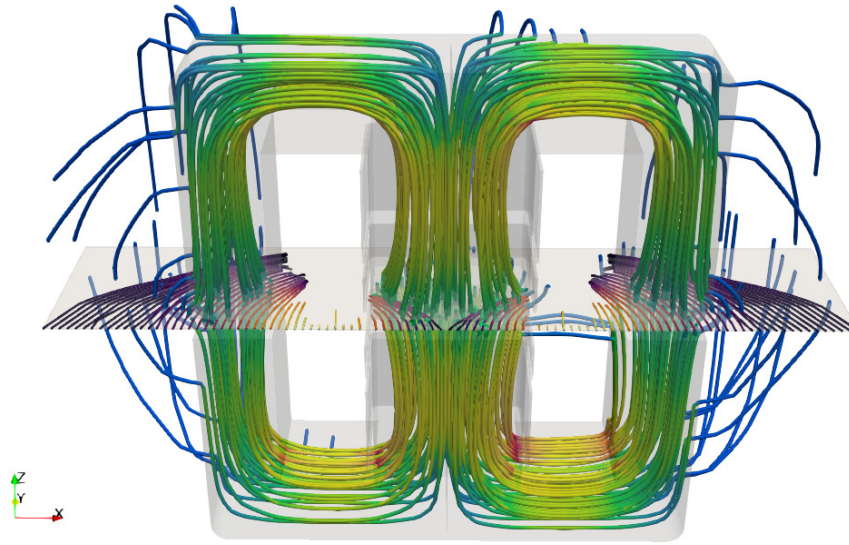


Figure 2.11: The field lines for the EC mode when the frequency is 10 Hz.

ParaView software, by converting the Abaqus-generated database into an unstructured grid file with the aid of C. Soyarslan's scripts ¹. In all figures, the core, sheet, and coils appear as gray regions with low opacity. Additionally, the applied current is denoted as EMCDA, the magnetic field as EMB, and the induced currents as EMCD. As depicted in Figure 2.12, at low frequencies, the magnetic field lines are perpendicular to the sheet, as the eddy currents are small and do not create a significant opposing magnetic field. However, as the frequency increases, the magnetic field lines become parallel to the sheet, as illustrated in Figure 2.14. This can be attributed to an increase in eddy currents in the sheet, which bend the magnetic field lines. At even higher frequencies, as shown in Figures 2.13 and 2.15, the magnetic field penetrates the air due to even higher eddy currents in the sheet.

¹The streamtracer filter is used to plot the streamlines of the fields. The tube filter is used to give the streamlines some radius. Furthermore, the reflect feature is used together with symmetry to show half of the sensor.





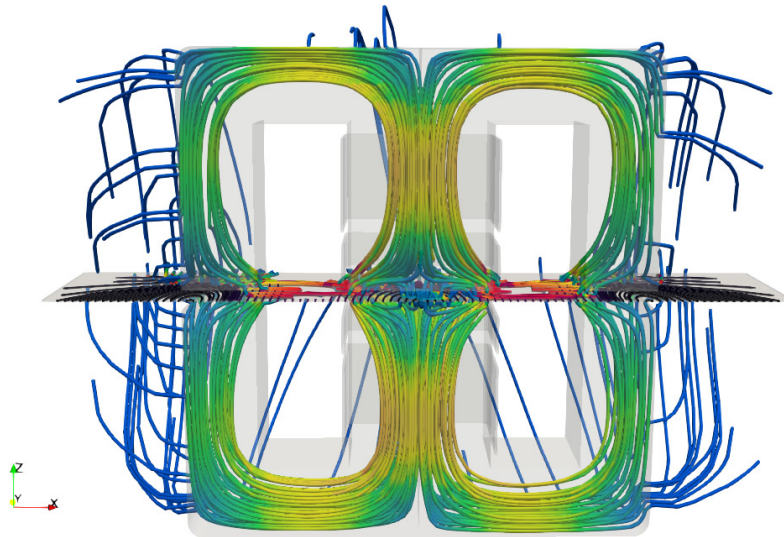
Magnetic flux density: min  max
 Eddy current density: min  max

Figure 2.12: The field lines for the EC mode when the frequency is 50 Hz. $EMCD_{max} = 2.8 \times 10^3$ $min = 0$, $EMB_{max} = 7.6 \times 10^{-2}$, $min = 0$.





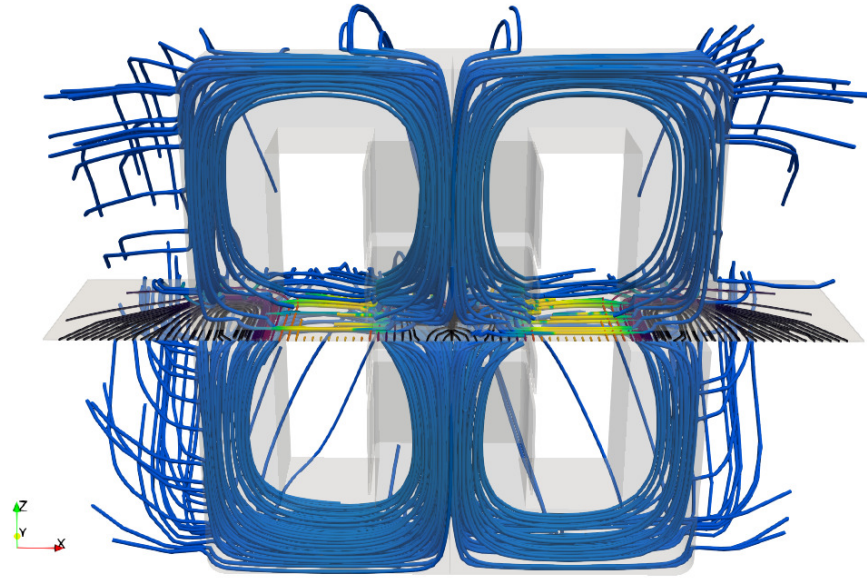
Magnetic flux density: min  max
 Eddy current density: min  max

Figure 2.13: The field lines for the EC mode when the frequency is 5×10^4 Hz. $EMCD_{max} = 2.8 \times 10^3$ $min = 9.5 \times 10^{-2}$, $EMCD_{max} = 2.6 \times 10^7$, $min = 0$





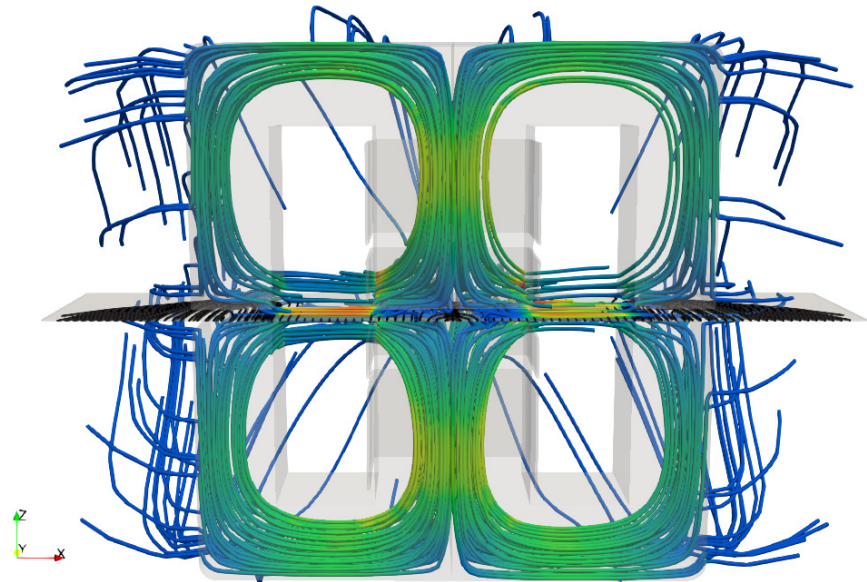
Magnetic flux density: min  max
 Eddy current density: min  max

Figure 2.14: The field lines for the EC mode when the frequency is 5×10^5 Hz. $EMB \max = 1.8 \times 10^{-1}$ $\min = 5.5 \times 10^{-7}$, $EMCD \max = 3.3 \times 10^7$, $\min = 0$





Magnetic flux density: min  max
 Eddy current density: min  max

Figure 2.15: The field lines for the EC mode when the frequency is 1×10^7 Hz, $EMB \max = 2.8 \times 10^{-2}$ $\min = 5.5 \times 10^{-6}$, $EMCD \max = 8.6 \times 10^7$, $\min = 0$

2.10 Parameter studies

2.10.1 Eddy current mode results

This section presents an analysis of the influence of thickness, width, permeability and conductivity on the inductance curve in the eddy current mode. The transmitter is excited with a range of frequencies, and the phase and gain of the inductance at each frequency are determined using the method described in Section 2.6. The phase and gain are then fitted using the equivalent circuit explained in Section 2.7.

In the appendix in Figure H.1 the resulting curves are shown when the τ_p and τ_n are fitted based on phase using least squares curve fitting. What can be seen is that the fitted curves are poor. For this reason, it is chosen to fit the values of τ_p and τ_n such that the magnitude and frequency of the minimum phase are equal to the minimal phase that results from cubic spline interpolation. The resulting fits can be seen for the most extreme sheet properties in Figure 2.16 as well as in the Appendix Figures H.2, and H.3.

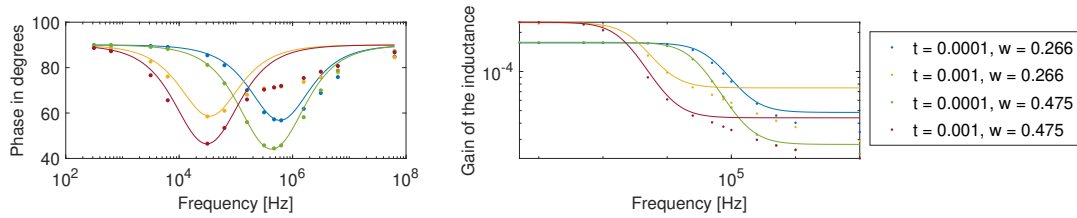


Figure 2.16: The differences between the fit of the electrical circuit and the fem model.

From the fitted values of τ_p and τ_n the values of \mathcal{R}_2 and \mathcal{L}_2 are determined. To look if the curve fitting makes sense simulations are done in which μ and σ are varied. The results are shown in Figures 2.17 and 2.19. In these figures, it can be easily recognized that \mathcal{L}_2 exclusively depends on μ and \mathcal{R}_2 exclusively depends on σ . This is expected because \mathcal{L}_2 is the inductance and \mathcal{R}_2 the resistance as defined in Section 2.7.

The next step is to derive an expression that can predict \mathcal{L}_2 . From Figure 2.17 it can be seen it is easy to describe the relation between \mathcal{L}_2 and μt . The relation between \mathcal{L}_2 and w , see Figure 2.18, is more complex as it depends on the thickness. For this reason, a new parameter ζ is introduced. ζ is defined as

$$\zeta = \left(\frac{w}{w_0}\right)^\alpha \left(\frac{t}{t_0}\right)^\beta, \quad (2.40)$$

where $w_0 = 1$ [m] and $t_0 = 1$ [m] are the reference width and thickness. Fitting α and β in order to get a correlation coefficient as close to one as possible gives $\alpha = -4.851$ and $\beta = 0.184$. Plotting \mathcal{L}_2 against ζ in Figure 2.17 shows a slope independent of thickness. This is confirmed by overlaying the curves by subtracting the mean value for each thickness as $\mathcal{L}_2 - \bar{\mathcal{L}}_2$ in Figure 2.17. Based on these plots it is assumed that \mathcal{L}_2 has the form of Equation 2.41.

$$\mathcal{L}_2 = K_1 \mu t + K_2 \zeta + C_1 \quad (2.41)$$

Where K_1 , K_2 and C_1 are coefficients with units [1/m], [] and [], respectively. The constant C_1 can be found using the values of \mathcal{L}_2 , t , w and μ for some measurements. The resulting

expression is shown in Equation 2.42.

$$\mathcal{L}_2 = 0.00101\mu t + 4.40 \times 10^{-12}\zeta + 4.75 \times 10^{-5} \quad (2.42)$$

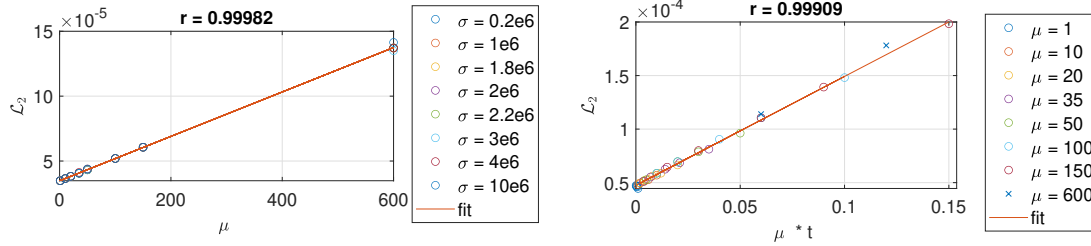


Figure 2.17: The value of \mathcal{L}_2 for varying permeability and conductivity (left). The value of \mathcal{L}_2 plotted against the product of μ and t (right).

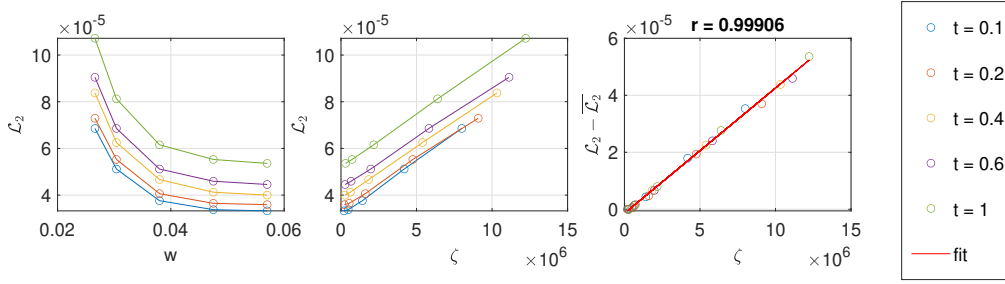


Figure 2.18: The value of \mathcal{L}_2 against the width(left). It can be hard to see, however, the relation is not linear. The value of \mathcal{L}_2 against ζ (center). The curves of \mathcal{L}_2 against ζ overlaid on top of each other (right). The thickness in the legend and width on the x-axis have the units of [mm].

The next step is to describe how \mathcal{R}_2 depends on the different sheet properties. In Figure 2.19 a relation can be recognized between the logarithm of \mathcal{R}_2 and the logarithm of wt as well as the logarithm of σ .

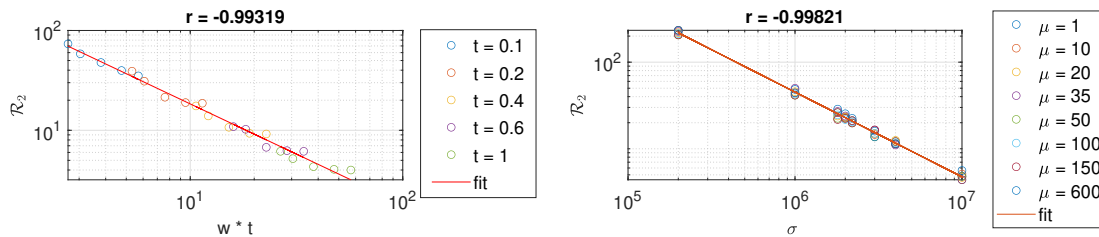


Figure 2.19: The relation between \mathcal{R}_2 and the product of w and t (left). The relation between \mathcal{R}_2 and σ including the fit (right). The thickness and width have the units of [mm].

Both of the relations can be fitted and summed together. The resulting expression is shown in Equation 2.43.

$$\log(\mathcal{R}_2) = -1.01 \log(wt) - 0.979 \log(\sigma) + C_2 \quad (2.43)$$

The slopes of -1.01 and -0.979 are rounded off to -1 for sake of simplicity. Fitting the value of C_2 using the entire expression for several combinations of width, thickness, and conductivity gives

$$\mathcal{R}_2 = 369 \frac{1}{wt\sigma}. \quad (2.44)$$

To check whether the predicted values make sense they are plotted against the fitted values of \mathcal{L}_2 and \mathcal{R}_2 in Figure 2.20. It can be seen the prediction is accurate based on the correlation coefficients, r , which are shown in the title of the figure.

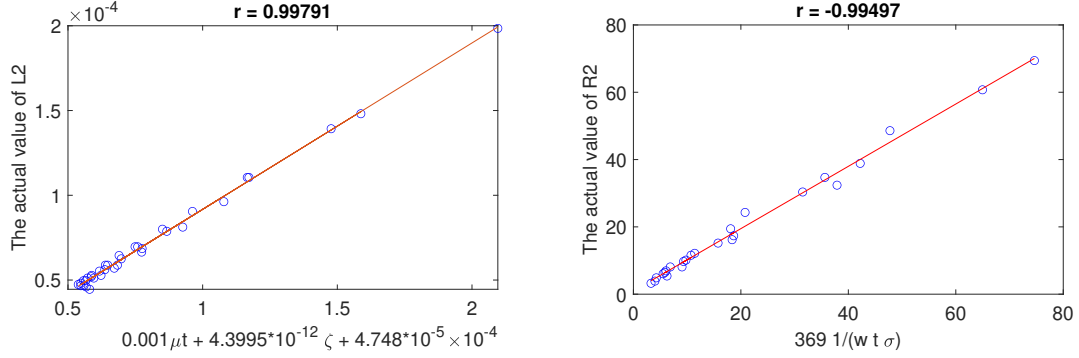


Figure 2.20: The predicted value of \mathcal{L}_2 (x-axis) against the value resulting from the simulation (y-axis) (left). The predicted value of \mathcal{R}_2 (x-axis) against the value resulting from the simulation (y-axis) (right).

Now the relations for \mathcal{R}_2 and \mathcal{L}_2 have been given they can be inverted. The results are shown below.

$$\mu = \frac{\mathcal{L}_2 - 4.40 \times 10^{-12}\zeta + 4.75 \times 10^{-5}}{0.00101t} \quad (2.45)$$

$$\sigma = 369 \frac{1}{\mathcal{R}_2 t w} \quad (2.46)$$

2.10.2 Permeance results

The gain can be fitted using Equations 2.47 and 2.48. It has been chosen to make two different equations for different ranges of width. The reason for this is that around 0.023 mm the width of the sheet is similar to that of the core, which means the dependence on width changes. This can be recognized as the kink in Figure 2.21. To look at which form the equations should be the statistical programming language R is used. The different inputs for the equation are compared based on their significance value in Table 2.6. From

Table 2.6: The P-values for different inputs are used for the prediction of the gain in the permeance mode. Note that lower p-values indicate stronger relations. Also, note that μ is the relative permeability.

Significance (P) value	$\sqrt{\mu t w}$	$\mu t w^2$	$\mu t^2 w$	$\mu^2 t^2 w^2$
w > 23mm	2×10^{-16}	0.0048	2×10^{-16}	0.0081
w < 23mm	2×10^{-16}	2×10^{-16}	1.28×10^{-9}	Not used

this table, the two most significant contributions are taken which gives Equations 2.47 and 2.48.

$$\mathcal{L}_{w < 0.023} = 0.00185 \sqrt{\mu t w} + 0.742 \mu t w^2 + 3.079 \times 10^{-5} \quad (2.47)$$

$$\mathcal{L}_{w > 0.023} = 0.00261 \sqrt{\mu t w} + 7.15 \mu t^2 w + 2.059 \times 10^{-5} \quad (2.48)$$

The predicted value of the gain is compared to the value resulting from the simulation in Figure 2.21. The average error between the resulting simulated values and the predicted

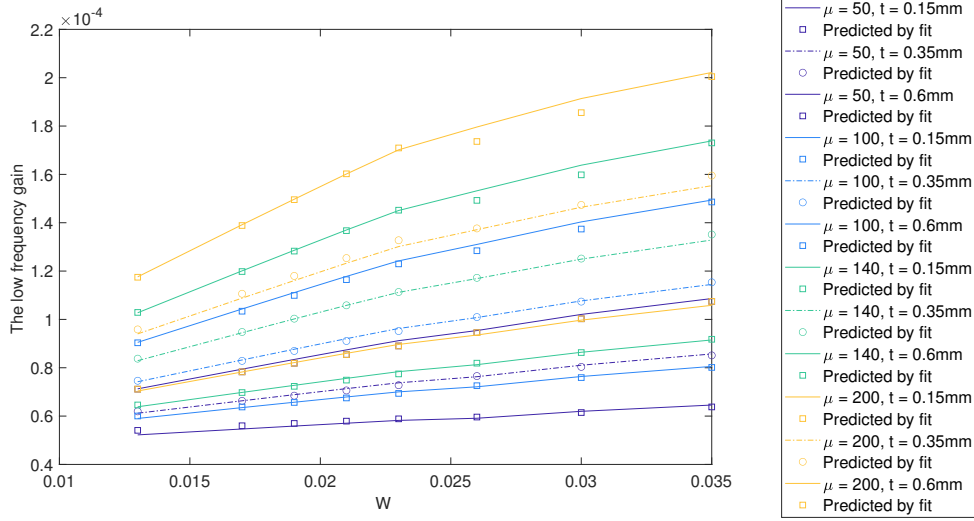


Figure 2.21: The predicted value for the gain based on Equations 2.47 and 2.48. The solid lines are the gains resulting from the simulations and the square markers are the predicted gains.

values is 0.9%. The fit is most poor around a width of 0.023 mm. An improvement to the model could be made by modeling more widths and expanding the prediction model.

2.11 Summary

This study aimed to investigate the use of an electromagnetic finite element (EM-FE) model to predict the inductance curve of an eddy current sensor. The results indicate that the model can accurately predict the shape of the inductance curve, but a correction must be made at higher frequencies due to the capacitance of the experimental set-up, which is difficult to model in the EM-FE model. The field line distribution images obtained from the simulations clearly show the origin of the shape of the inductance curve, where at low frequencies, the magnetic flux is perpendicular to the sheet, and as the frequency increases, the flux becomes parallel to the sheet, and eventually goes through the air. Finally, the study shows that the permeability and conductivity of the sheet can be obtained from the inductance curves using appropriate fitting methods.

3. Magnetic homogenization

3.1 Introduction

The preceding chapter has examined the correlation between the sensor readings and the mean microscopic properties. In this chapter, the emphasis shifts to demonstrating how the average magnetic properties can be determined from the microstructure characteristics. The magnetic homogenization theory for AISI420 will be presented, and the generation of the microstructures will be explained. Finally, the outcomes of the homogenization process for AISI420 will be presented. This chapter aims to provide a comprehensive understanding of how the magnetic properties of materials can be evaluated based on their microstructures.

3.2 Micromagnetic properties

This thesis focuses on the analysis of AISI420, an alloy comprised of chromium, carbon, and iron. The equilibrium phases for this alloy are depicted in Figure 3.1. Based on internal documents annealing is done below 800 degrees Celsius to prevent hardening [44]. During annealing at this temperature a mixture of ferrite (α , iron) and $M_{23}C_6$ carbides (C_1) are formed [45]. The carbides have a relative permeability of 1 since they are paramagnetic. The relative permeability of the ferrite is more difficult to obtain since it strongly depends on the impurities present in the iron [46] [47]. The relative permeability of iron ranges from 1 to 60000, depending on its composition [46]. In this thesis a relatively arbitrary value of 250 is assumed based on the measured permeability for low fields in [46] and [47].

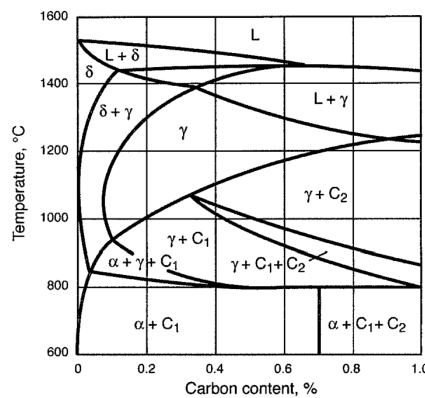


Figure 3.1: The phase diagram of Carbon, Iron, Chromium [45]

3.3 RVE creation

The process of homogenizing a microstructure involves the creation of a representative volume element (RVE) that captures the magnetic behavior of the entire material. In the case of AISI420, the microstructure comprises of ferrite grains and carbide particles, which ideally require modeling the effect of both on the magnetic properties. However, the homogenization method employed in this thesis does not account for the orientation of the grains, rendering their incorporation into the RVE impractical. Several studies propose techniques for including the effect of grains on the magnetic properties, such as solving the energy potential function by finding the equilibrium of elastic, anisotropic, and exchange energy through three consecutive algorithms, as demonstrated in [48]. Although these approaches are promising, their implementation in Abaqus, the finite element analysis software used in this thesis, is non-trivial and requires further research. Therefore, the RVE is modeled as a homogeneous ferrite matrix with embedded carbide particles. To homogenize AISI420, the images of the carbide particles are binarized, as shown in Figure 3.2. This is done using ImageJ software¹. The results from this binarization can be seen in Figure 3.3.

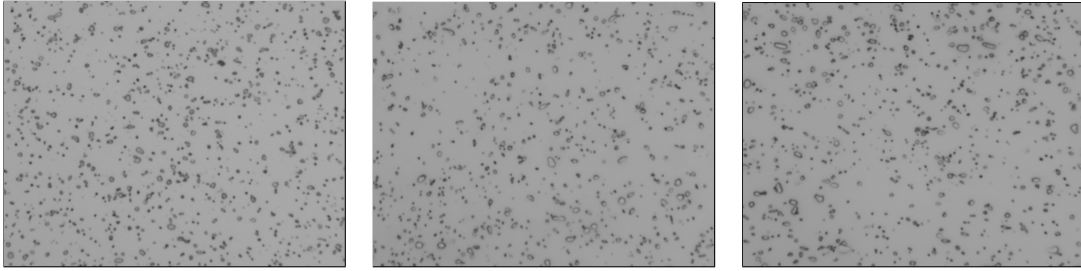


Figure 3.2: The pictures are taken from the microstructure.

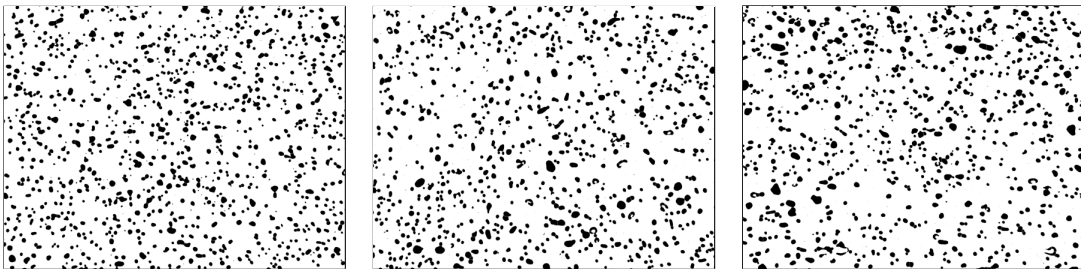


Figure 3.3: The processed binary images of the microstructures shown in Figure 3.2. Black corresponds to the carbides and white to the ferrite.

3.4 Homogenization theory

In this thesis, the homogenization will be explained based on the work in [5]. A more detailed description of the theory can be found in [49]. In literature, several different

¹The filters that are used in chronological order are: (i) Subtract background (ii) Bandpass filter (iii) Threshold(Yen dark) (iv) Fill holes (v) WaterShed.

models can be found to relate permeability to the inclusion volume fraction. The simplest estimates are that of Voigt and Reuss, denoted by μ_V^* and μ_R^* . These estimates are

$$\mu_V^* = \phi_1 \mu_1 + \phi_2 \mu_2, \text{ and} \quad (3.1)$$

$$\mu_R^* = [\phi_1 \mu_1^{-1} + \phi_2 \mu_2^{-1}]^{-1}, \quad (3.2)$$

where ϕ_1 and ϕ_2 are the volume fraction of the first and second phase, respectively. Furthermore, μ_1 and μ_2 are the permeability of the first and second phase, respectively. The actual effective permeability will lie somewhere between μ_V^* and μ_R^* . Several other estimates of permeability estimations are mentioned in Equations 3, 4, and 5 in [5]. In Figure 3.4 some of the analytical methods are compared to the numerical work done as well as the numerical methods used in this work. The model used to estimate the effective per-

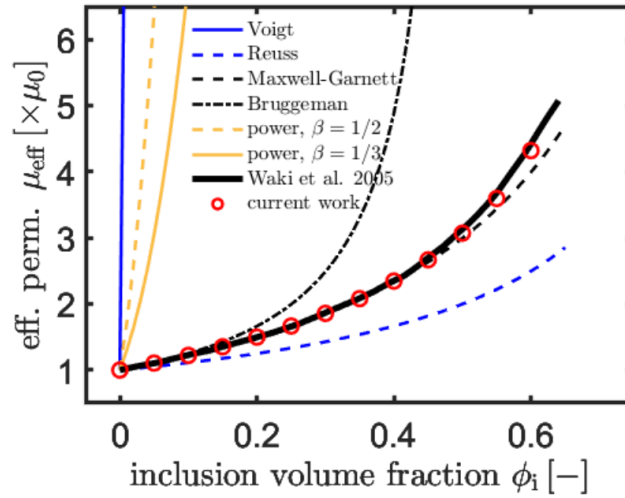


Figure 3.4: Comparison of the different inductance calculation methods, reproduced from [50]

meability assumes magnetostatic conditions. This means free currents can be ignored and the vector fields do not depend on time [5]. These assumptions can be used to obtain the equations described in Equation 3.3. When comparing Equation 3.3 and 3.4 it can be seen that the equations for magnetostatics have the same form as the equations for electrostatics.

$$\nabla \cdot \mathbf{B} = 0 \quad \mathbf{B} = \boldsymbol{\mu} \cdot \mathbf{H} \quad \mathbf{H} = -\nabla \phi \quad (3.3)$$

$$\nabla \cdot \mathbf{J} = 0 \quad \mathbf{J} = \boldsymbol{\sigma} \cdot \mathbf{E} \quad \mathbf{E} = -\nabla \phi \quad (3.4)$$

Where \mathbf{J} is electric current density, \mathbf{E} is the electric field, $\boldsymbol{\sigma}$ is the conductivity and ϕ is the electrical scalar potential. This similarity is used to model all simulations in the electrostatic packages in Abaqus because this offers more possibilities than the magnetostatic package. The element type that is used is DC2D4E, these are four-node linear coupled thermal-electric elements. The solution gives the resulting values of \mathbf{H} and \mathbf{B} in every cell, $\mathbf{H}^{(0)}$ and $\mathbf{B}^{(0)}$ respectively. These values can then be used to determine the behavior at the macroscale, M , using:

$$^M \mathbf{H} = \frac{1}{|\mathcal{V}|} \int_{\mathcal{V}} \mathbf{H}^{(0)} dV \quad ^M \mathbf{B} = \frac{1}{|\mathcal{V}|} \int_{\mathcal{V}} \mathbf{B}^{(0)} dV \quad (3.5)$$

${}^M\mathbf{H}$ and ${}^M\mathbf{B}$ can be used to determine the effective permeability using ${}^M\mathbf{B} = \boldsymbol{\mu}^* \cdot {}^M\mathbf{H}$. To determine all components of the 3 by 3 permeability tensor, $\boldsymbol{\mu}^*$, three different load cases must be analyzed. In each of the three different load cases an external gradient in the applied magnetic field, \mathbf{H} , is imposed in one direction. Component μ_{xx} is determined using the gradient of $\mu_{xx} = {}^M\mathbf{B}_x / {}^M\mathbf{H}_x$, where ${}^M\mathbf{B}_x$ and ${}^M\mathbf{H}_x$ are the effective magnetic and applied field in x-direction

3.5 Results

In the left side of Figure 3.5 the carbide particles are shown in black and the ferrite matrix in grey. In the right side of Figure 3.5 the resulting magnetic flux density can be seen. The results are presented using the evenly spaced streamlines 2D filter from ParaView, which is based on the algorithm described in [51].

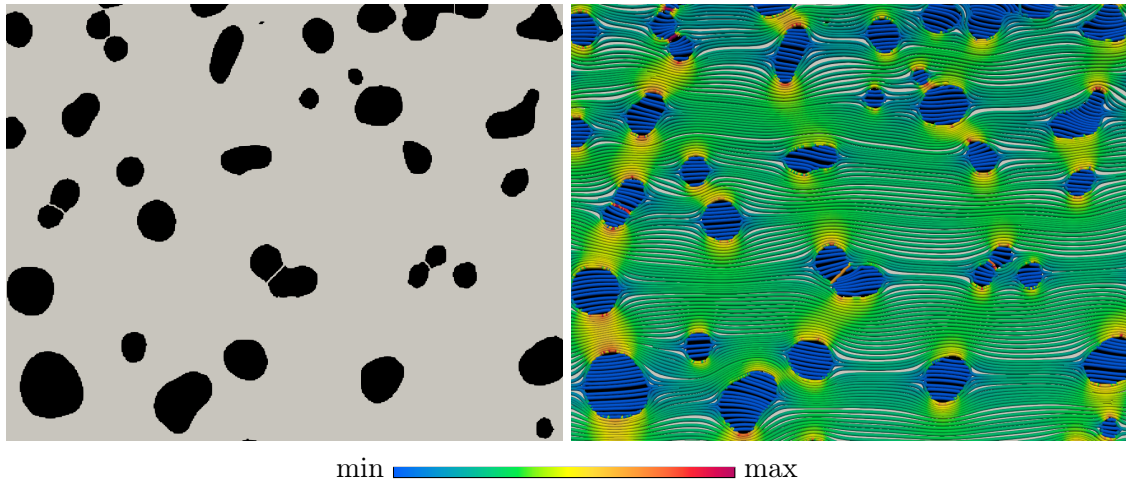


Figure 3.5: An illustration of the carbide particles (left) and the magnetic flux density (right). Colorbar is the magnetic flux density with $\max = 200$, $\min = 1$.

In Figure 3.6 the resulting permeability is plotted against different properties of the carbide particles. Interestingly enough it seems as if the volume fraction of the particles has the most influence on the resulting permeability. This means that the Equation 3.1 will describe the effective permeability relatively well.

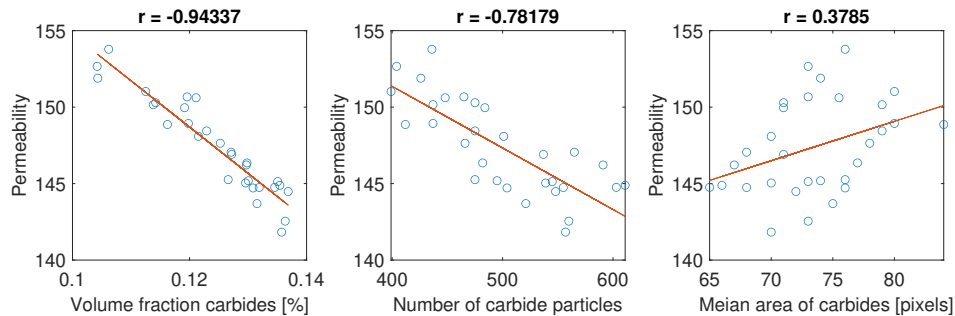


Figure 3.6: The results of the homogenization of permeability.

Part II.

Mechanics

4. Mechanical homogenization

4.1 Introduction

This chapter provides a comprehensive account of the steps used in the mechanical homogenization of AISI420. The chapter begins with a detailed description of the mechanical properties of the phases and a description of microstructure generation, followed by the postprocessing of stress and strain. The second part of the chapter presents the results of mechanical homogenization. Specifically, the relationship between mechanical properties and carbide volume fraction is analyzed. Additionally, the stresses and strains at the micro level during cyclic loading are studied.

4.2 Micromechanical properties

To accurately model the mechanical behavior of a material, it is essential to have reliable estimates of the mechanical properties of its constituent phases. In this regard, the analysis presented in [21] is employed to determine the mechanical properties of both the carbides and the ferritic matrix. The mechanical properties are repeated in Table 4.1. While alternative models, such as the one presented in [22], exist for estimating the mechanical properties of bcc-ferrite, the current study relies on the model from [21] due to the superior documentation and comprehensiveness of the model.

Table 4.1: The mechanical properties of ferritic AISI420, taken from [21].

Parameter	symbol	Ferrite	Carbide
Lattice	-	bcc	fcc
number of slip systems	N	12	12
Elastic modulus [GPa]	C_{11}, C_{12}, C_{44}	233,135,128	472,216,135
Reference shear [MPa]	$\dot{\gamma}_0$	10^{-6}	10^{-6}
Stress exponent	n_{slip}	62.4	200
Plastic shear stress [MPa]	$\tau_{C,0}$	72.5	1200
Saturation shear stress [MPa]	τ_{sat}	241.0	2000
Reference hardening [MPa]	h_0	2659.9	20
Hardening parameter	a	2.832	1.1
Strengthening coef [MPa m ^{1/2}]	k_y	0.783	-

It should be noted that in Damask 3 the initial slip resistance and saturated slip resistance are denoted using ξ_0 and ξ_c . In general, these values can be assumed to be equivalent to the initial and saturation shear stresses, τ_0 and τ_c , respectively. This assumption is supported by comparing the material configuration files available on [52] with the corresponding literature, such as [23].

4.3 RVE creation

The microstructure of the material being studied comprises two components, namely, the ferritic grains and the carbide particles. The ferritic grains can be observed through electron backscatter diffraction [ESBD] imaging, while atomic force microscopy [AFM] measurements are used to visualize the carbide particles. The ESBD and AFM measurements for the AISI420 alloy analysed in this thesis can be seen in Figure 4.1.

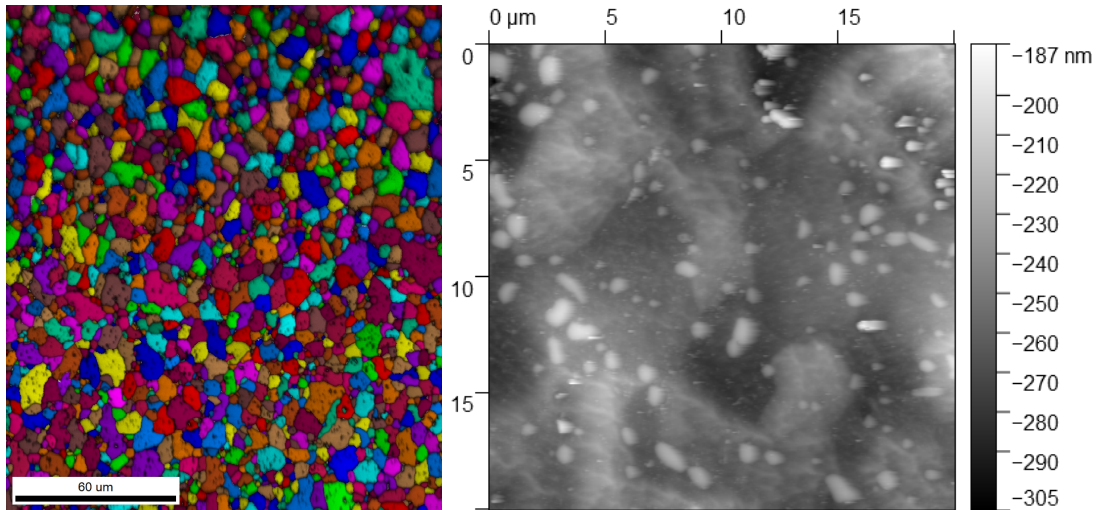


Figure 4.1: The microstructure visualized using ESBD (left) and AFM (right) [42].

To model the mechanical behavior of materials, it is common practice to create a representative volume element [RVE] that captures the characteristics of the material in question. Various techniques exist for generating RVEs, and one such method is described in [21], where RVEs are produced using DREAM 3D software, which allows for the recreation of grain size distributions with a high degree of similarity. In this study, an alternative method for generating RVEs is adopted, namely the utilization of a power diagram, also referred to as the Laguerre-Voronoi diagram. The power diagram technique has been demonstrated to be highly effective in creating RVEs that closely resemble the microstructure of actual materials [53]. Figure 4.2 serves to illustrate this concept, providing a visual comparison between the Voronoi diagram and the Laguerre-Voronoi diagram.

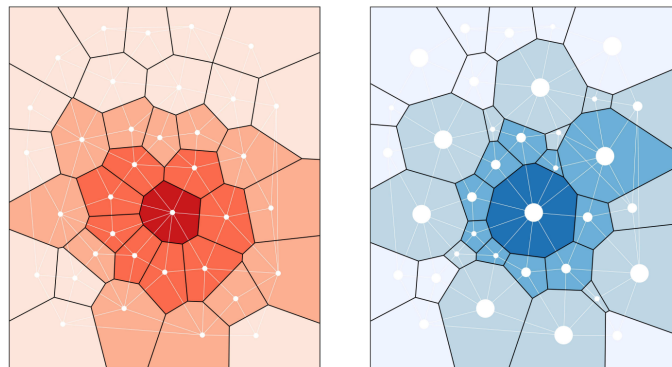


Figure 4.2: Normal Voronoi diagram (left) vs a Laguerre Voronoi diagram (right), reproduced from [54].

The implementation of the power diagram is done using [55]. A modified normal distribution is chosen for the weights of the power diagram, which is defined as

$$y = k \frac{1}{\sigma\sqrt{2\pi}} \exp \left[-\frac{(x - \mu)^2}{2\sigma^2} \right]. \quad (4.1)$$

The values of μ , k , and σ are fitted using `fmincon` based on the measured grain size distribution and are found to be 2.0, $1.287 \cdot 10^{-4}$ and 4.87, respectively. An example of a microstructure generated with a power diagram and normal Voronoi construction is shown in 4.3. The grain size distribution resulting from Voronoi tessellation and power diagram generation is shown in Figure 4.4.

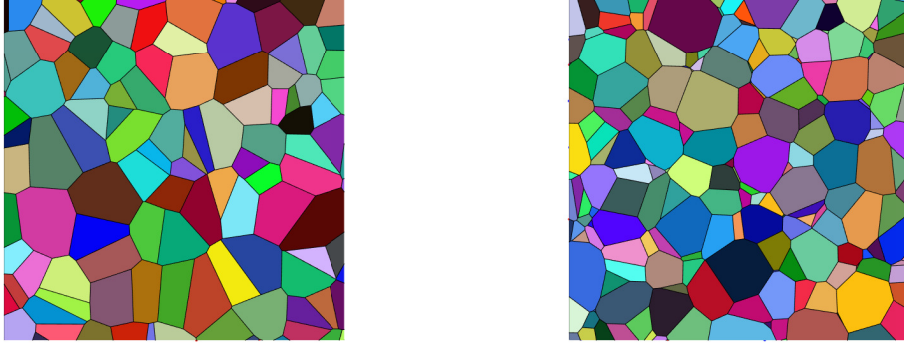


Figure 4.3: The grain structure resulting from Voronoi generation (left) and the grain structure resulting from Power diagram generation (right).

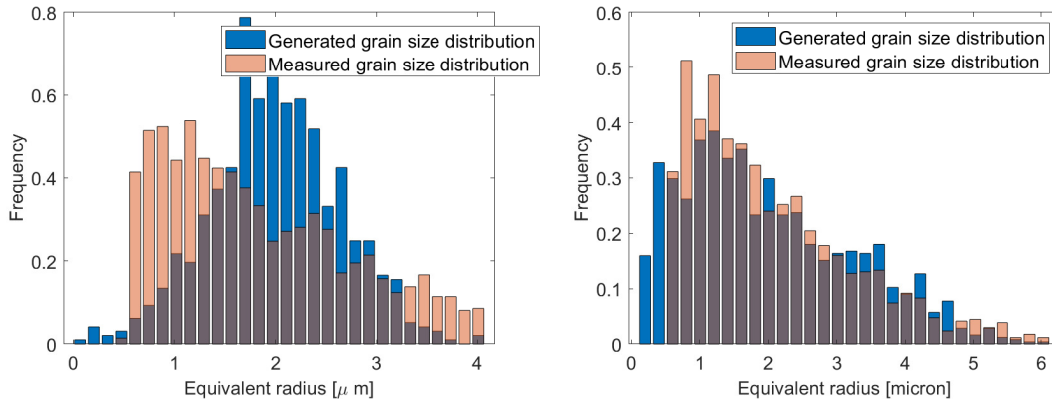


Figure 4.4: The histogram of the grain size distribution produced using Voronoi generation (left) and the histogram of the grain size distribution resulting from power diagram generation (right).

In this study, the effect of carbide distribution on the mechanical properties of AISI420 is investigated. Several Representative Volume Elements (RVEs) are created with varying carbide distributions while keeping the grain structure and grain orientation constant. Figure 4.5 presents the ferrite grains on the left and overlaid with carbide particles on the right.

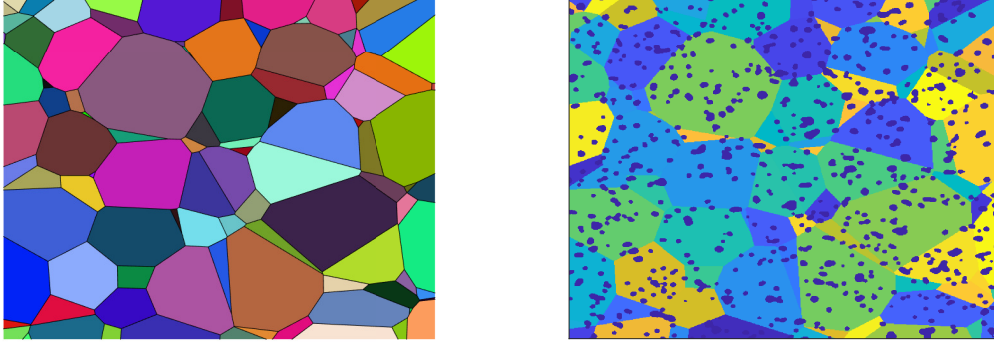


Figure 4.5: The grains generated using the power diagram generator (left). The grains overlaid with the carbides (right).

4.4 Homogenization theory

Several different strain and stress measures can be extracted from Damask to calculate the true stress and strain. The true stress is given by the Cauchy-stress tensor, \mathbf{T} , which can be directly obtained from Damask. The Cauchy-stress tensor is a function of the First-Piola-Kirchoff stress tensor, \mathbf{P}_a , Greens deformation tensor, \mathbf{F}^e , according to

$$\boldsymbol{\sigma}_a = \frac{1}{J} \mathbf{P}_a \cdot \mathbf{F}^e. \quad (4.2)$$

Where $J = \det(\mathbf{F}) > 0$ corresponds to the volume ratio. All strain measures in Damask are part of the Seth-Hill family. In this family, the strain is described as

$$\mathbf{E}_{(m)} = \frac{1}{2m} (\mathbf{U}^{2m} - \mathbf{I}) \quad m \neq 0 \quad (4.3)$$

$$\mathbf{E}_0 = \ln \mathbf{U} \quad m = 0. \quad (4.4)$$

From this formula, it can be chosen to use the Green-Langranian, Biot, logarithmic strain, or Almansi strain by using a value of 1, 0.5, 0, and -1 for m , respectively. This can be confirmed by reading the source code [56] which uses the definitions from [57]. In this case, the logarithmic strain must be used, which means that m is set to 0. The logarithmic strain is referred to as \mathbf{E} . The stress and strain can be averaged using the following equation as can be read in [58]

$$T_{11}(t) = \frac{1}{|\mathcal{V}|} \int_{\mathcal{V}} T_{11}(t) dV \quad E_{11}(t) = \frac{1}{|\mathcal{V}|} \int_{\mathcal{V}} E_{11}(t) dV, \quad (4.5)$$

where V and \mathcal{V} represent the deformed volume. The undeformed volume, v , can be utilized along with the Jacobian, $J = dV/dv$, to obtain Equation 4.6. Rewriting this expression gives Equation 4.7.

$$T_{11}(t) = \frac{\sum_{i=1}^N T_{11,i} J_i v_i}{\sum_{i=1}^N J_i v_i} \quad E_{11}(t) = \frac{\sum_{i=1}^N E_{11,i} J_i v_i}{\sum_{i=1}^N J_i v_i} \quad (4.6)$$

$$T_{11}(t) = \frac{\sum_{i=1}^N T_{11,i}(t) J_i}{\sum_{i=1}^N J_i} \quad E_{11}(t) = \frac{\sum_{i=1}^N E_{11,i}(t) J_i}{\sum_{i=1}^N J_i} \quad (4.7)$$

Besides the postprocessing of stress and strain, it is important to use the appropriate boundary conditions. For uni-axial tension the boundary conditions in Damask are normally defined using the deformation gradient as defined in Equation 4.8, as can be read in [59], [60], [61] and [62]. After integrating the resulting stress it can be seen that the resulting macroscopic shear stresses are non-zero. This is not desirable. For this reason, the deformation gradient shown in Equation 4.9 is imposed. It can be seen that the resulting stress state is more purely uniaxial.

$$\mathbf{F}_{ij} = \begin{bmatrix} 1.01 & 0 & 0 \\ 0 & * & 0 \\ 0 & 0 & * \end{bmatrix} \quad \mathbf{T}_{ij} = \begin{pmatrix} 304.3674 & 6.3322 & 2.1923 \\ 6.3322 & -0.0027 & 3.0041 \\ 2.1923 & 3.0041 & -0.0107 \end{pmatrix} \text{ [MPa]} \quad (4.8)$$

$$\mathbf{F}_{ij} = \begin{bmatrix} 1.01 & 0 & * \\ * & * & 0 \\ 0 & * & * \end{bmatrix} \quad \mathbf{T}_{ij} = \begin{pmatrix} 303.9733 & -0.0019 & 0.0003 \\ -0.0019 & -0.0030 & 0.0002 \\ 0.0003 & 0.0002 & -0.0099 \end{pmatrix} \text{ [MPa]} \quad (4.9)$$

Where \mathbf{F}_{ij} corresponds to the deformation gradient aim and \mathbf{T}_{ij} corresponds to the first Piola-Kirchoff stress tensor. In these Equations, * corresponds to an undefined deformation and 1.01 means the material is strained 1%. To test whether the described model accurately represents the real life phenomena an experimental validation is performed. In Figure 4.6 the experimentally measured stress-strain curve is compared to the simulated stress-strain curve. It should be noted that the true strain on the x-axis is subtracted by the strain at the yield point. This yield point has been determined with the 0.2% offset method in which the intersection has been determined using [63]. It can be seen there is a good match between the simulation and experiments.

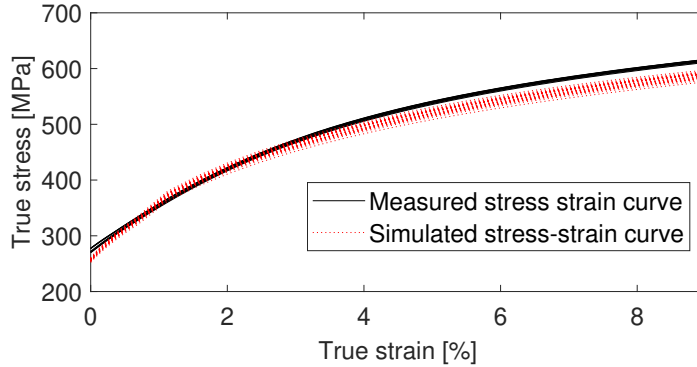


Figure 4.6: The true stress and strain curve plotted for multiple heat treatments of AISI420 (black lines). The true stress strain curve plotted for multiple carbide distributions (red dotted lines).

4.5 Effect of carbides on mechanical properties

Prior to discussing the simulations on the mechanical behavior of AISI420 some literature is given on the experimentally observed mechanical behavior of AISI420. A detailed study of the effect of carbides on the strain development in annealed AISI420 is done in [64]. The strain development in this article was studied using kernel average misorientation (KAM) measurements and image quality maps (IQ) which quantify the amount of localized plastic strain. The results can be seen in Figure 4.7. In this article the following phenomena were

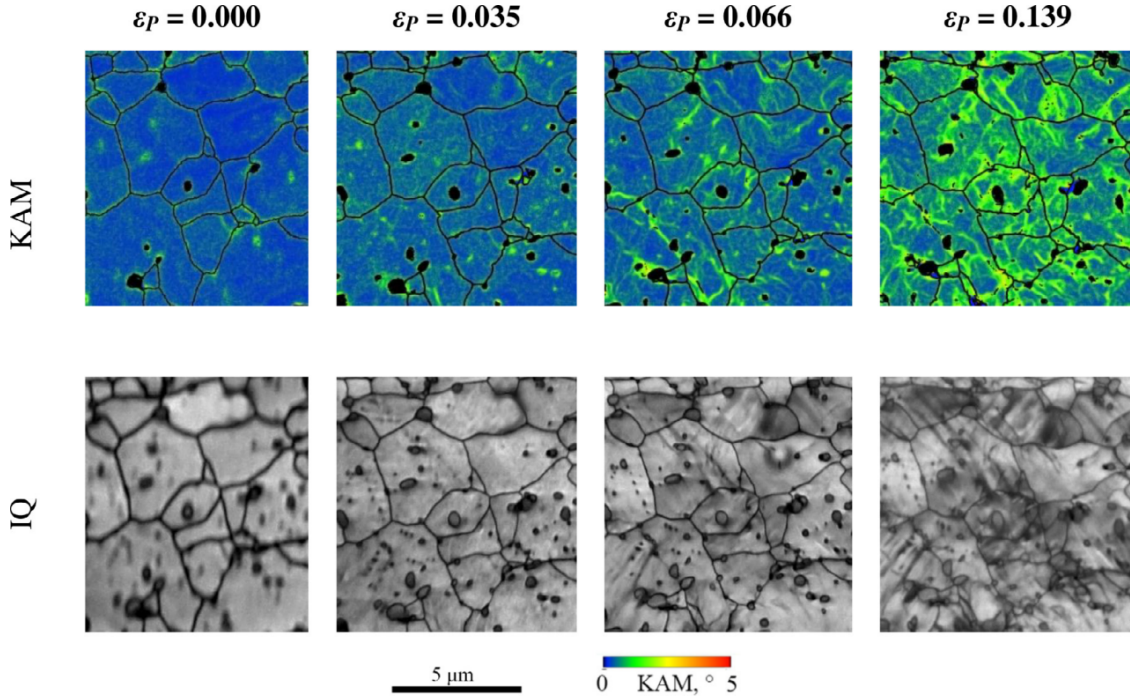


Figure 4.7: The KAM measurements over the strain range, reproduced from [64].

observed (i) From the KAM measurements it can be seen that at low strains the strain developments are governed by long-distance interactions, which means the influence of carbides is large. At higher strains short range dislocation interactions become dominant and the influence of carbides decreases [64]. (ii) Before any loading is applied there exists local plastic strain around the carbides. This is expected to be due to the difference in thermal expansion coefficients. (iii) The shear bands start to develop at $\epsilon_p = 0.066$ as can be seen from the IQ maps. Also, it can be observed that the shear bands do not necessarily form where the KAM values are high.

This thesis aims to investigate the impact of carbides on the mechanical properties by employing crystal plasticity simulations in the DAMASK software. Numerous tensile tests are simulated for a variety of carbide distributions, as defined in Section 4.3, while adhering to the boundary conditions specified in Section 4.4. To assess the effect of carbide distribution on yield strength, Figure 4.8 presents a plot of yield strength against several carbide distribution properties. The results demonstrate a strong relationship between the yield strength and the volume fraction of carbides.

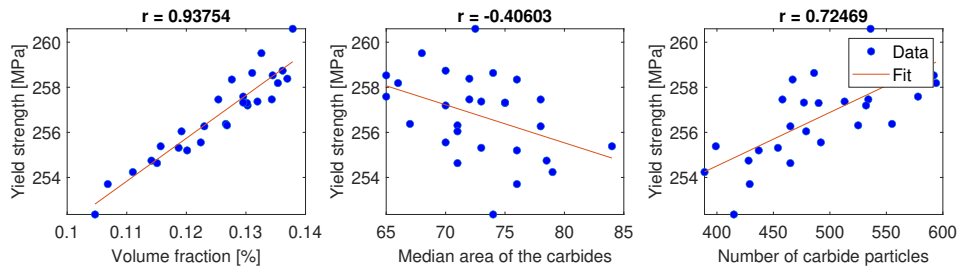


Figure 4.8: The effect of carbides on the yield strength of the material. In the title, the coefficient of correlation is given for each different relation.

Other important parameters in the deep drawing process are the hardening properties. An overview of the different hardening laws is given below, based on the work done in [65].

$$\sigma = C\varepsilon^n \quad (4.10)$$

$$\sigma = C(\varepsilon_0 + \varepsilon)^n \quad (4.11)$$

$$\sigma = A + B\varepsilon^n \quad (4.12)$$

$$\sigma = A + B[1 - \exp(-C\varepsilon)] \quad (4.13)$$

Equations 4.10, 4.11, 4.12 and 4.13, refer to the Hollomon, Swift, Ludwik, and Voce strain hardening models. In this thesis, the Voce equation will be used. For this study, the Voce equation is chosen based on the analysis conducted in [66], which showed that it properly describes the hardening behavior of a wide range of metals, including ferritic stainless steels. In the Voce equation, the yield strength is represented by A , the amount of strain hardening at strain saturation is represented by B , and the strain hardening exponent is represented by C . A higher value of C indicates a faster increase of stress with strain. In the literature, it is well-known that a low hardening exponent can result in the formation of cracks near the punch radius, while high hardening exponents tend to transfer the local hardening to larger regions. Therefore, high hardening exponents are generally preferred for the deep drawing process. Equation 4.13 can be fitted for all stress-strain curves, which provides a hardening exponent for all carbide distributions. It should be noted that the fitting has been done using a strain range between 3 and 10 %. This is not optimal, a more ideal strain range would be between 10 and 20 % [67]. From Figure 4.9 it can be seen that the volume fraction has a higher influence on the plastic behaviour compared to the elastic behaviour. The hardening exponent varies $\sim 10\%$ compared to a variation of $\sim 2\%$ in the Young's modulus.

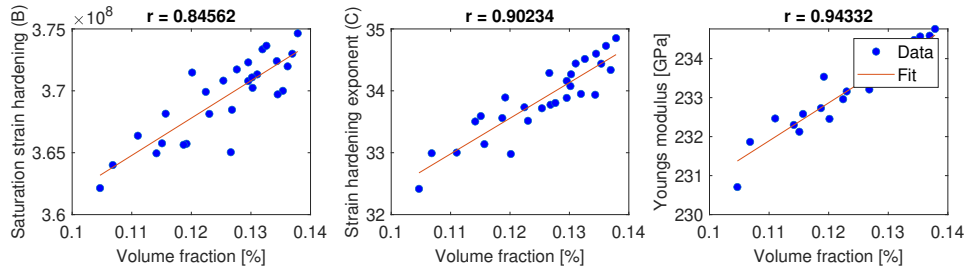


Figure 4.9: The generated grain structure (left). The grain structure overlaid with the carbide particles (right).

4.6 Effect of stress on magnetic properties

This subsection will analyze the interaction between stress and magnetic properties. To understand this, the theory of magnetic domains and domain walls will be explained first, based on the work in [24]. Afterward, this knowledge will be used, along with plasticity simulations, to interpret inductance curves during cyclic loading.

4.6.1 Domain wall theory

A ferromagnetic material exists out of many magnetic domains in which the direction of the magnetic moment of the atoms is constant. The space of approximately 100 atoms between

the domains, where the magnetic moment direction changes, is known as the domain wall [7]. For ferromagnetic materials, it holds that when there is no external magnetization magnetic domains have random orientations. On the other hand, when there is some external magnetization the domains with a favorable orientation will grow or rotate and the sample will become magnetized.

There are two ways in which domains can grow or rotate, as explained in [27]. An hysteretic magnetization is the first, in which domain walls are free to move to their thermodynamic equilibrium state and are not impeded by pinning sites. The movement of domain walls is reversible, and they move back to their original position when the external field is removed. The second is non-anhysteretic magnetization, in which the movement of the domain walls is inhibited by pinning sites, such as dislocations and impurities, for which domain walls need extra energy to overcome. This non-anhysteretic domain wall movement is irreversible. Below a list will be given on the factors influencing the behavior of magnetic domains.

- *Grains*: Larger grains lead to bigger magnetic domains and thus higher permeability [2]. The relationship between grain size and permeability is described by a Hall-Petch type of relationship. The effect of crystal anisotropy is described in detail in [6]. The anisotropy is important because it costs energy to turn the magnetization vector from the easy axis to the direction of the applied field.
- *Magnitude of the stress*: Stress affects magnetization, as explained based on a simple tensile test. Residual stresses present in the sample before the test affect the stress field and the energy of impurities and dislocations [27]. Impurities and dislocations are referred to as pinning sites as they block domain wall movement. Compressive stresses increase the energy of pinning sites and thereby reduce domain wall mobility [27]. When a tensile load is applied, compressive stresses decrease. The decrease in compressive stresses leads to decreased energy of the pinning sites. At some point the energy of the pinning sites is low enough that they no longer obstruct domain wall motion. This is called the anhysteretic state. Based on this analysis it would seem permeability increases with stress up to some value. However, there is a second effect. The anhysteretic curve itself can decrease with stress, which is indicated by the magnetostrictive coefficient illustrated in Figure 4.10. This means that when increasing stress is applied it is possible that the magnetization first increases due to the increasingly anhysteretic state and then decreases due to the effects of stress on the anhysteretic curve. This effect is generally referred to as Villari reversal. This idea is confirmed by experiments from which the results are shown in Figure 4.10. A description of the effect is given by the following equation [26].

$$\frac{dM}{d\sigma} = \frac{\sigma}{E\zeta}(M_{\text{an}} - M) + c \frac{dM_{\text{an}}}{d\sigma} \quad (4.14)$$

Where E is the modulus of elasticity, ζ a coefficient that has the dimension of energy per volume, M_{an} is the anhysteretic component of magnetization and c represents the ratio of initial anhysteretic magnetic susceptibility and initial magnetic susceptibility.

Similar to the permeability the effective conductivity is also affected by stress, which is described in [68]. The relationship between conductivity and stress can be expressed mathematically as:

$$\frac{\Delta\sigma}{\tau_c} = \frac{1}{2}(K_{\parallel} + K_{\perp}), \quad (4.15)$$

where $\Delta\sigma$ and τ_c are the change in conductivity and stress and K_{\parallel} and K_{\perp} are the parallel and normal electro-elastic coefficients. It should be noted that the net effect for most materials is too small to detect, which is used to neglect it for the rest of this work.

- *Plastic strain*: Isolated dislocations and small dislocation tangles are surmountable by domain walls [26]. However, as plastic strain is increased the isolated dislocation density, as well as the dislocation tangles, increase [69]. These form strong pinning sites for domain wall motion [2] [26]. The permeability decreases sharply with the onset of plastic deformation and decreases more slowly with higher degrees of plastic deformation.
- *Cyclic loading*: For cyclic loading the effects can be seen in Figure 4.11 based on the work done in [70]. The peaks in the magnetic field are caused by the Villari reversal effect. The reversals during unloading (tail reversals) vary less per cycle than those during loading.

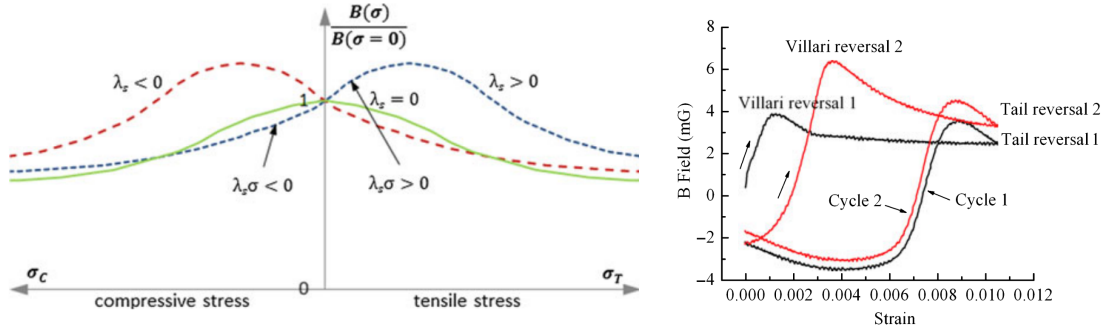


Figure 4.10: The effect of stress on permeability (left), reproduced from [71] and the permeability for two cycles of loading (right), reproduced from [70].

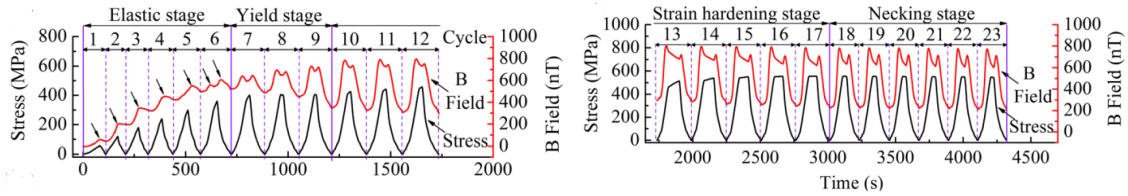


Figure 4.11: The variation of the inductance for cyclic loads, reproduced from [26].

4.6.2 Interpreting inductance during cyclic loading

Cyclic tensile tests were performed in which the inductance was measured simultaneously. The results can be seen in Figure 4.12. Simulations are done to explain the observed phenomena from a microstructural points of view. The loading conditions that are used for elastic loading, plastic loading, and releasing are as follows

$$\text{Elastic loading} \quad \dot{F}_{ij} = \begin{bmatrix} 1e-3 & 0 & * \\ * & * & 0 \\ 0 & * & * \end{bmatrix} \quad P_{kl} = \begin{bmatrix} * & * & 0 \\ 0 & 0 & * \\ * & 0 & 0 \end{bmatrix} \quad (4.16)$$

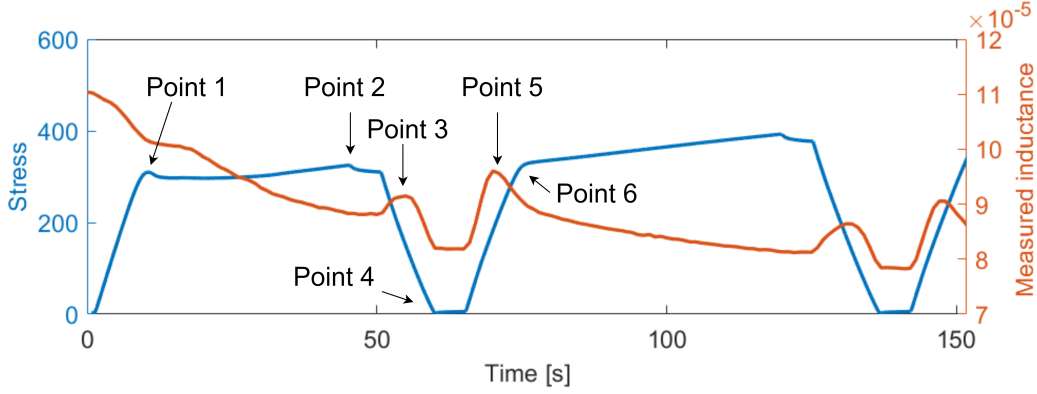


Figure 4.12: The figure illustrating the cyclic loading done in the experiments (left) [42].

$$\text{Plastic loading} \quad \mathbf{F}_{ij} = \begin{bmatrix} \varepsilon_{\text{desired}} & 0 & * \\ * & * & 0 \\ 0 & * & * \end{bmatrix} \quad \mathbf{P}_{kl} = \begin{bmatrix} * & * & 0 \\ 0 & 0 & * \\ * & 0 & 0 \end{bmatrix} \quad (4.17)$$

$$\text{Releasing} \quad \mathbf{F}_{ij} = \begin{bmatrix} * & 0 & * \\ * & * & 0 \\ 0 & * & * \end{bmatrix} \quad \mathbf{P}_{kl} = \begin{bmatrix} * & * & 0 \\ 0 & 0 & * \\ * & 0 & 0 \end{bmatrix} \quad (4.18)$$

Where $\varepsilon_{\text{desired}}$ is the amount of plastic strain for that cycle. The reason a strain rate is chosen for elastic loading is that if an absolute strain is imposed of for example 0 high forces are needed to remove the residual stresses, which is not desirable.

Now that the boundary conditions have been established the results are analyzed. The results will be shown for the points in Figure 4.12. For all points the following results are plotted: (i) The plastic strain (ii) The directions of the eigenvectors corresponding to the maximum, medium, and minimum principal stresses¹. (iii) The hydrostatic stress, which is calculated as follows

$$\sigma_{av} = \frac{\sigma_1 + \sigma_2 + \sigma_3}{3}, \quad (4.19)$$

where σ_1, σ_2 and σ_3 are the principal stresses, respectively. All the resulting fields are shown in Figures 4.13 to 4.17. Note that in Figure 4.13 compressive stresses are blue and tensile stresses red.

Now that all of the different loading situations have been analyzed the curve of the permeability can be explained using the theory from Section 4.6.1. The explanation for each point is as follows: *Point 1*: Here plastic strain and thus dislocation density are low. Furthermore, stress is oriented rather homogeneously. This is expected to lead to high permeability. *Point 2*: The decrease in permeability is likely to be related to an increase in plastic strain and thus dislocations. *Point 3*: There is a decrease in external stresses which affects the anhysteretic magnetization curve through the magnetostrictive coefficient. This is expected to lead to the observed increase in permeability. *Point 4*: The

¹The streamline images are created using the following steps (i) Slice filter normal to plane (ii) Use calculator filter: "phase/mechanical/v_max(sigma)/1_X"*iHat+ "phase/mechanical/_ (sigma)/1_Y"*jHat. (iii) Apply cell data to the points filter. (iv) Use evenly spaced streamlines 2D filter (v) If this filter crashes, change the value of "closed loop maximum distance". (vi) Apply tube filter.

externally applied stress decreases, which changes the energy of the pinning sites. This is expected to lead to a decrease in permeability. *Point 5*: Permeability increases due to an anhysteretic state (see point 3). *Point 6*: Permeability reduces due to the magnetostrictive effect (see point 2).

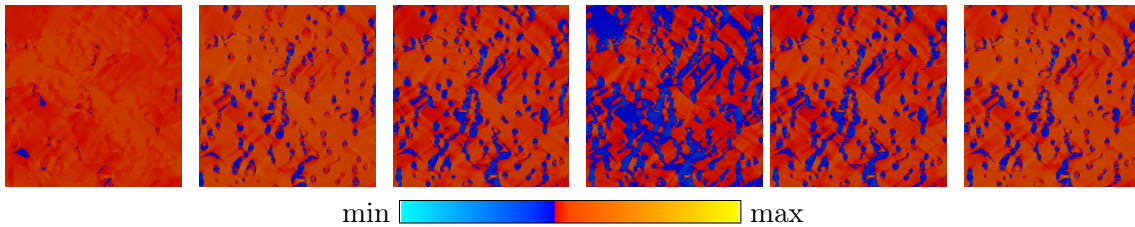


Figure 4.13: The hydrostatic stress, red indicates tensile, blue indicates compressive. The figures corresponds from left to right to points 1 to 6 in Figure 4.12.

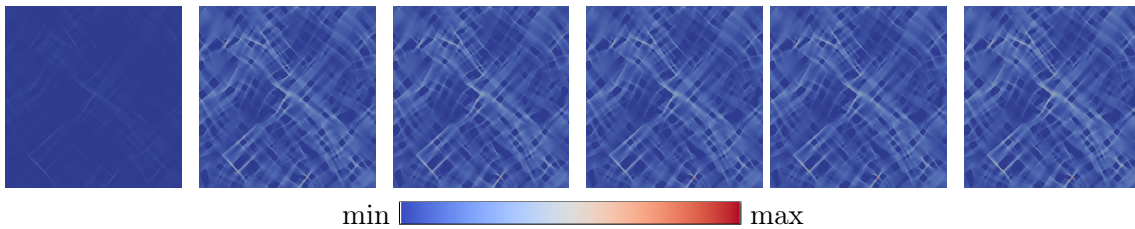


Figure 4.14: The plastic true strain, max is $1.6e-1$ min is 0. The figures corresponds from left to right to points 1 to 6 in Figure 4.12.

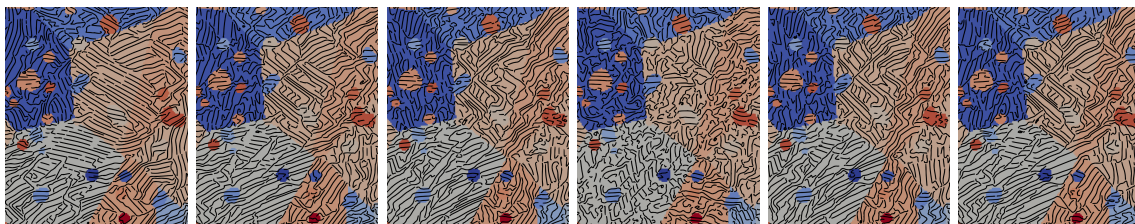


Figure 4.15: The eigenvector directions relating to the maximum principal stress. The figures corresponds from left to right to points 1 to 6 in Figure 4.12.

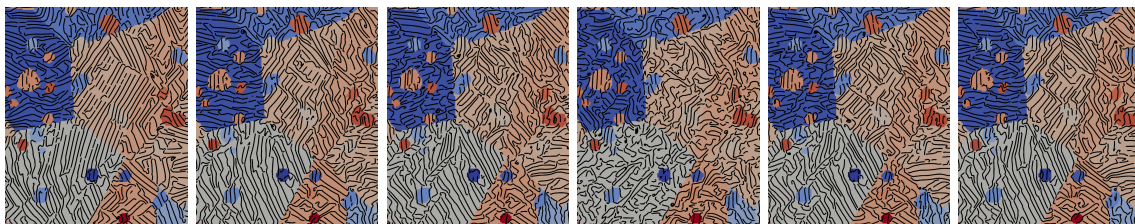


Figure 4.16: The eigenvector directions relating to the median principal stress. The figures corresponds from left to right to points 1 to 6 in Figure 4.12.

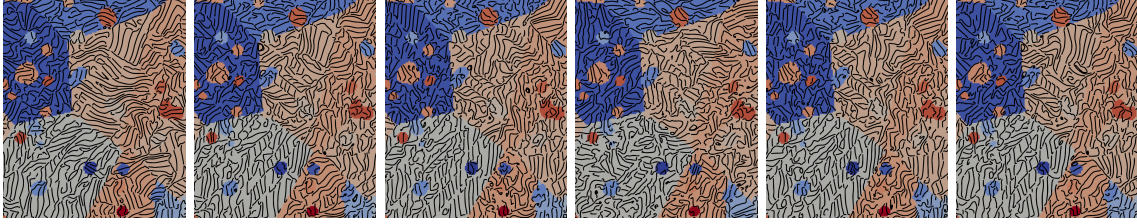


Figure 4.17: The eigenvector directions relating to the minimum principal stress. The figures corresponds from left to right to points 1 to 6 in Figure 4.12.

4.7 Summary

In this chapter, it has been shown how the mechanical behavior of AISI420 can be accurately modeled in Damask. The simulated stress-strain curves are validated against experimental data, demonstrating the accuracy of the model. The study reveals that the volume fraction of carbides significantly affects many mechanical properties. This is a hopeful finding as the permeability in the previous chapter was also strongly related to the volume fraction of carbides. Furthermore, the chapter presents a thorough analysis of the magnetic and mechanical phenomena that occur during cyclic loading. It is found that the spikes in permeability are caused by Villari reversals and the overall decrease is caused by an accumulation of dislocations.

Part III.

Correlations and discussions

5. Correlations

5.1 Magnetic to mechanical

The correlations between mechanical and magnetic properties are investigated in many papers. Studies on the experimental correlation are done in [72], [73], [74], [75] and [2]. The most important experimental findings are as follows: (i) Magnetic homogeneity can be used to predict mechanical homogeneity [73]. (ii) In [2] it was shown the magnetic properties could be related to microstructure properties such as phase fraction, illustrated on the left of Figure 5.1. More recently, neural networks have been employed to relate magnetic and mechanical properties [76] [77]. Neural networks are not able to predict the mechanical properties very accurately yet, see the right of Figure 5.1. It is found that when using four magnetic properties the error in the mechanical property estimation becomes around 10%, depending on the mechanical property [77]. It should be noted that measuring these four magnetic properties inline may be impossible. Interestingly, the combined homogenization of both mechanical and magnetic properties is not commonly discussed in the literature. Typically, the homogenization steps are carried out separately, as demonstrated in [78] for magnetic homogenization and [21] for mechanical homogenization. However, combining these homogenization processes can provide valuable insights into the relationship between magnetic and mechanical properties. In the following section, this combined approach is explored along with the insights it can offer.

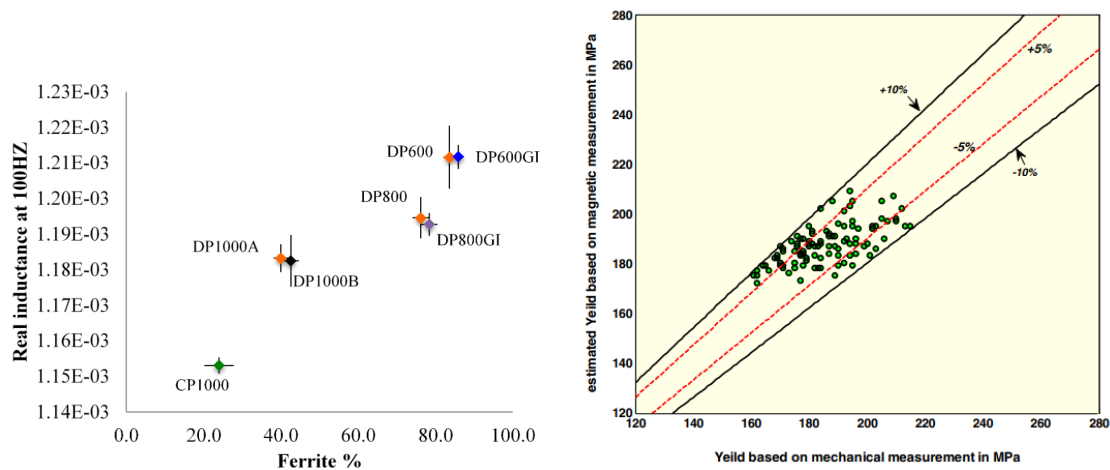


Figure 5.1: The measured inductance against the phase fraction (left), reproduced from [2]. A neural network scheme including input parameters used to predict mechanical properties, reproduced from [77] (right).

Chapter 3 and 4 present two methodologies to calculate the magnetic and mechanical properties of representative volume elements. These methodologies can be used to determine

the correlation between magnetic and mechanical properties. By applying both mechanical and magnetic homogenization to several RVEs, the resulting mechanical properties can be plotted against the resulting magnetic properties, as shown in Figure 5.2. This figure clearly shows a correlation between the magnetic and mechanical properties, confirming the possibility of using magnetic property identification to characterize mechanical properties. This finding is significant as it provides a novel approach to characterizing materials, potentially saving time and resources in the characterization process. The methodologies presented in this study have the potential to be applied to a variety of materials and provide insight into their mechanical properties using magnetic characterization.

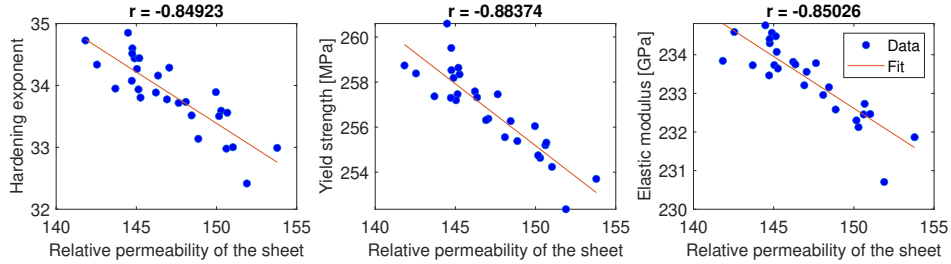


Figure 5.2: The yield strength (left), hardening exponent (center), and elastic modulus (right) against the permeability of the sheet. The coefficient of correlation is stated in the title.

5.2 Conclusion

Below a list is given of the key findings in this work is given separated over the different chapters.

- **Chapter 2. Sensor model:** (i) A derivation, implementation and validation of several inductance calculations in EM-FE simulations is performed. (ii) An EM-FE model is described to simulate the measured inductance. The model is validated with experimental measurements. (iii) The eddy current sensor response has been simulated for many different sheet properties. The results can be used to relate the characteristics of the inductance curve to the permeability and conductivity of the sheet.
- **Chapter 3. Magnetic homogenization:** A novel homogenization model is used to show that for AISI420 the permeability is linearly related to the volume fraction of carbides.
- **Chapter 4. Mechanical homogenization:** (i) The mechanical homogenization of AISI420 is described including experimental validation. (ii) It is shown plastic properties are strongly related to carbide volume fraction. Also it is shown elastic properties are light dependent on carbide volume fraction. (iii) It is shown that the experimentally observed spikes in inductance during cyclic loading are related to Vilari reversals. Furthermore, it is shown the overall decrease in permeability is related to dislocation accumulation.
- **Chapter 5. Correlations and discussions:** Mechanical and magnetic homogenization are used to show that permeability is strongly related to mechanical properties.

Besides these separate contributions to literature it is emphasised that this thesis describes a framework to model the relation between eddy current sensor readings and mechanical properties. This framework is a one of its kind as there are no other articles linking macroscopic sensor modeling with microscopic mechanical and magnetic homogenization. This framework is shown in Figure 5.3 and can be implemented inline is as follows: (i) The sensor readings can be used to find the value of \mathcal{R}_2 and \mathcal{L}_2 or \mathcal{L} . (ii) The results from the sensor simulations can be used to inverse fit the values of μ and σ . (iii) The values of μ and σ can be used to give an estimation for the mechanical properties.

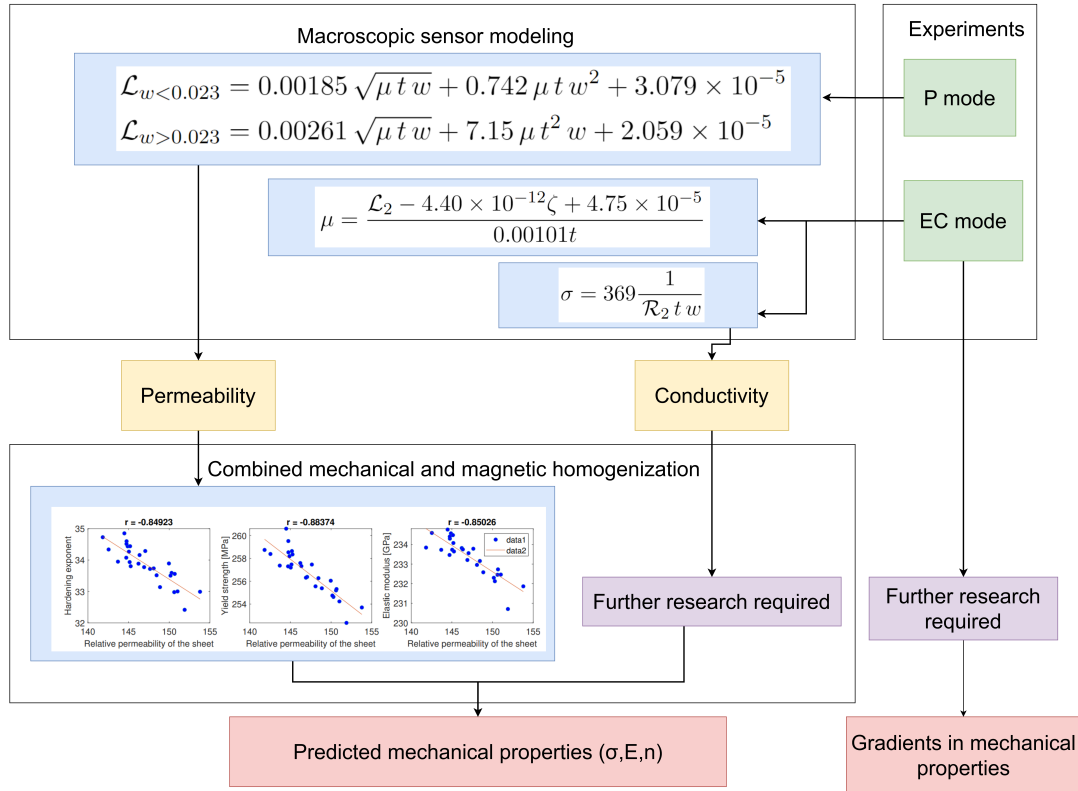


Figure 5.3: The total overview of the problem.

5.3 Future research

As the field of eddy current testing continues to evolve, there are several promising avenues for future research that could lead to new insights and breakthroughs. One area that holds particular promise is the development of coupled simulations that can model both magnetic and mechanical behavior on a micro-scale. These simulations could shed light on the influence of grain structure and residual stresses on the magnetic and mechanical properties of materials, providing a more comprehensive understanding of the underlying physical phenomena. Another area that could benefit from further research is the development of more accurate equivalent electrical circuit models. Such models could incorporate capacitance and provide a deeper understanding of eddy currents, potentially enabling more precise measurements and more sensitive defect detection. Finally, exploring the effects of local permeability gradients on eddy current curves could also yield valuable insights. By studying the impact of these gradients, it may be possible to improve the accuracy and

sensitivity of eddy current testing for detecting local defects. Overall, these areas represent exciting and potentially fruitful directions for future research in the field of eddy current testing. With continued exploration and investigation, it is likely that even more effective and precise techniques for non-destructive testing and evaluation will emerge.

Bibliography

- [1] J. Shen, L. Zhou, W. Jacobs, P. Hunt, and C. Davis, “Real-time in-line steel microstructure control through magnetic properties using an em sensor,” *Journal of Magnetism and Magnetic Materials*, vol. 490, p. 165504, 2019.
- [2] L. Zhou, “Non-destructive characterisation of steel microstructures using electromagnetic sensors,” 2015.
- [3] D. Wright and D. Ward, “Inline non-destructive material property testing; the future of manufacturing,” in *Heat Treat 2021: Proceedings of the 31st ASM Heat Treating Society Conference*, pp. 51–56, 09 2021.
- [4] A. Kumar and W. Arnold, “High resolution in non-destructive testing: A review,” *Journal of Applied Physics*, vol. 132, no. 10, p. 100901, 2022.
- [5] C. Soyarslan, J. Havinga, L. Abelman, and T. van den Boogaard, “Estimation of the effective magnetic properties of two-phase steels,” in *Achievements and Trends in Material Forming- Peer-reviewed extended papers selected from the 25th International Conference on Material Forming, ESAFORM 2022* (G. Vincze and F. Barlat, eds.), Key Engineering Materials, (Switzerland), pp. 2040–2049, Trans Tech Publications Ltd, July 2022. Funding Information: This work was supported by the STW project 15472 of the STW Smart Industry 2016 program. This support is gratefully acknowledged. Publisher Copyright: © 2022 The Author(s). Published by Trans Tech Publications Ltd, Switzerland.; 25th International Conference on Material Forming, ESAFORM 2022, ESAFORM ; Conference date: 27-04-2022 Through 29-04-2022.
- [6] R. M. Bozort, “Ferromagnetism,” *Bell Telephone Laboratories*, 1951.
- [7] C. S. G. CD, *Physics of Ferromagnetism*. Oxford University Press, 1997.
- [8] C. D. G. B. D. Cullity, *Introduction to Magnetic Materials, 2nd Edition*. Wiley-IEEE Press, 2008.
- [9] N. Ida, “Alternative approaches to the numerical calculation of impedance,” *Ndt International*, vol. 21, pp. 27–35, 1988.
- [10] A. Mosallanejad and A. Shoulaie, “Calculation and measurement of coil inductance profile in tubular linear reluctance motor and its validation by three dimensional fem,” *Journal of Electrical Engineering*, vol. 62, no. 4, pp. 220–226, 2011.
- [11] D. Zarko, D. Ban, and R. Klarić, “Finite element approach to calculation of parameters of an interior permanent magnet motor,” *AUTOMATIKA: Journal for Control, Measurement, Electronics, Computing and Communications (korema@fer.hr); Vol.46 No.3-4*, 01 2006.

- [12] Y. L. Bihan, "Lift-off and tilt effects on eddy current sensor measurements: a 3-d finite element study," *European Physical Journal-applied Physics*, vol. 17, pp. 25–28, 2002.
- [13] D. Vasić, I. Rep, D. Å pikić, and M. Kekelj, "Model of magnetically shielded ferrite-cored eddy current sensor," *Sensors*, vol. 22, no. 1, 2022.
- [14] X. Hao, W. Yin, M. Strangwood, A. Peyton, P. Morris, and C. Davis, "Characterization of decarburization of steels using a multifrequency electromagnetic sensor: Experiment and modeling," *Metallurgical and Materials Transactions A*, vol. 40, pp. 745–756, 04 2009.
- [15] M. Luloff, *Numerical Modelling of Eddy Current Probes for CANDU Fuel Channel Inspection*. PhD thesis, University of Groningen, 09 2016.
- [16] T.-O. Kim, G.-S. Lee, H.-Y. Kim, and J.-H. Ahn, "Modeling of eddy current sensor using geometric and electromagnetic data," *Journal of Mechanical Science and Technology*, vol. 21, pp. 465–475, 03 2007.
- [17] A. Rosell and G. Persson, "Modelling of a differential sensor in eddy current non-destructive evaluation," 2011.
- [18] J. Harms and T. A. Kern, "Theory and modeling of eddy current type inductive conductivity sensors," *Engineering Proceedings*, vol. 6, no. 1, 2021.
- [19] P. May and E. Zhou, "Numerical modelling and design of an eddy current sensor," in *Numerical Modelling* (P. Miidla, ed.), ch. 8, Rijeka: IntechOpen, 2012.
- [20] A. Sridhar, M.-A. Keip, and C. Miehe, "Homogenization in micro-magneto-mechanics," *Computational Mechanics*, vol. 58, 07 2016.
- [21] J. Galan-Lopez and J. Hidalgo, "Use of the correlation between grain size and crystallographic orientation in crystal plasticity simulations: Application to aisi 420 stainless steel," *Crystals*, vol. 10, no. 9, 2020.
- [22] M. Diehl, "Damask 2 documentation - 3.1.1. material configuration file, bcc-ferrite," 2013.
- [23] C. Zambaldi, Y. Yang, T. R. Bieler, and D. Raabe, "Orientation informed nanoindentation of alpha-titanium: Indentation pileup in hexagonal metals deforming by prismatic slip," *Journal of Materials Research*, vol. 27, no. 1, pp. 356–367, 2012.
- [24] K. Ara and M. Brakas, "Inverse magnetostrictive sensitivity of martensitic stainless steel aisi-410 and its application to pressure measurements," *IEEE Transactions on Magnetism*, vol. 11, no. 5, pp. 1352–1354, 1975.
- [25] H. Kwun and G. L. Burkhardt, "Effects of grain size, hardness, and stress on the magnetic hysteresis loops of ferromagnetic steels," *Journal of Applied Physics*, vol. 61, no. 4, pp. 1576–1579, 1987.
- [26] S. Bao, M. Fu, Y. Gu, and S. Hu, "Evolution of the piezomagnetic field of ferromagnetic steels subjected to cyclic tensile stress with variable amplitudes," *Experimental Mechanics*, vol. 56, 02 2016.
- [27] D. C. Jiles and D. L. Atherton, "Theory of the magnetisation process in ferromagnets and its application to the magnetomechanical effect," *Journal of Physics D: Applied Physics*, vol. 17, p. 1265, jun 1984.

- [28] F. Shiyu, B. Peter, S. Jan, and D. Jianning, "Characterization of steel material for shaving caps by means of magnetic measurements," 2019.
- [29] J. C. Maxwell, *A Treatise on Electricity and Magnetism*. Oxford University Press, 1783.
- [30] J.-M. Jin, *The Finite Element Method in Electromagnetics*. John Wiley & Sons, 2014.
- [31] D. C. L. Davis, "Lecture notes - university of louisville depertmenet of pyysics - displacement current."
- [32] W. Frei, "Exploiting symmetry to simplify magnetic field modeling," 2014.
- [33] D. Saini, A. Ayachit, and M. Kazimierczuk, "Design and characterization of single-layer solenoid air-core inductors," *IET Circuits, Devices & Systems*, vol. 13, 03 2019.
- [34] C. A. Valdivieso Gomez, R. Vazquez Sabariego, and G. Meunier, "Contribution to the modeling of homogenized windings with the finite element method - eddy-current and capacitive effects," 2021-01-07.
- [35] D. Mayer, "Complex inductance and its computer modelling," in *Journal of ELECTRICAL ENGINEERING*, 2002.
- [36] R. F. Harrington, *Time-Harmonic Electromagnetic Fields*. IEEE-Press, 2001.
- [37] W. R. Smythe, "Static and dynamic electricity," in *Pure and Applied physics*, 1989.
- [38] M. Gyimesi and D. Ostergaard, "Inductance computation by incremental finite element analysis," *IEEE Transactions on Magnetics*, vol. 35, no. 3, pp. 1119–1122, 1999.
- [39] W. E. Rogers, *Introduction to electric fields, a vector analysis approach*. McGraw-Hill New York, 1954.
- [40] S. Vujevic, T. Modric, and D. Lovric, "The difference between voltage and potential difference," in *Proceedings of the Joint INDS 11 and ISTET 11*, pp. 1 – 7, 08 2011.
- [41] K. Mizukami, Y. Watanabe, and K. Ogi, "Eddy current testing for estimation of anisotropic electrical conductivity of multidirectional carbon fiber reinforced plastic laminates," *Composites Part A: Applied Science and Manufacturing*, vol. 143, p. 106274, 2021.
- [42] E. Rouwhorst, "Modelling of em sensor and investigation of aisi 420 microstructure for non-destructive testing.."
- [43] R. C. Jackson, E. W. Lee, and A. G. H. Troughton, "The influence of the method of demagnetization on the reversible permeability of a high-permeability nickel-iron alloy," *British Journal of Applied Physics*, vol. 9, p. 495, dec 1958.
- [44] M. de Vries et al, "Annealing experiments to improve coining micro-formability of aisi 410 and n004," *Philips Internal Report*, 2010.
- [45] Y. Wu, D. Blaine, B. Marx, and C. Schlaefel, "Effects of residual carbon content on sintering shrinkage, microstructure and mechanical properties of injection molded 17-4 ph stainless steel," *Journal of Materials Science*, vol. 37, pp. 3573–3583, 09 2002.

- [46] T. Yensen, "What is the magnetic permeability of iron?," *Journal of the Franklin Institute*, vol. 206, no. 4, pp. 503–510, 1928.
- [47] S. Kawabata, "Magnetic permeability of the iron yoke in high field superconducting magnets," *Nuclear Instruments and Methods in Physics Research Section A: Accelerators, Spectrometers, Detectors and Associated Equipment*, vol. 329, no. 1, pp. 1–8, 1993.
- [48] A. Sridhar, M.-A. Keip, and C. Miehe, "Homogenization in micro-magneto-mechanics," *Computational Mechanics*, vol. 58-1, pp. 151–169, 2016.
- [49] S. Celal, "Asymptotic homogenization in the determination of effective intrinsic magnetic properties of composites," *Results in Physics*, 2022.
- [50] S. Celal, "integrating models and real-time data for zero-defect manufacturing control systems," 2021.
- [51] B. Jobard and W. Lefer, "Creating evenly-spaced streamlines of arbitrary density," *Proceedings of the eight Eurographics Workshop on visualization in scientific computing*, vol. 7, 12 1997.
- [52] C. Z. et al., "Damask - file formats - material configuration - phase - phenopowerlaw _ti," 2013.
- [53] X. Zheng, T. Sun, J. Zhou, R. Zhang, and P. Ming, "Modeling of polycrystalline material microstructure with 3d grain boundary based on laguerreâ€“voronoi tessellation," *Materials*, vol. 15, p. 1996, 03 2022.
- [54] T. J. Yoon, M. Ha, W. Lee, and Y.-W. Lee, "A corresponding-state framework for the structural transition of supercritical fluids across the widom delta," 12 2018.
- [55] F. McCollum, "Power diagrams matlab central file exchange," 2023.
- [56] F. Roters, M. Diehl, P. Shanthraj, P. Eisenlohr, C. Reuber, S. L. Wong, T. Maiti, A. Ebrahimi, T. Hochrainer, H.-O. Fabritius, S. Nikolov, M. Friak, N. Fujita, N. Grilli, K. G. F. Janssens, N. Jia, P. J. J. Kok, D. Ma, F. Meier, E. Werner, M. Stricker, D. Weygand, and D. Raabe, "Source code for damask.mechanics," 2022.
- [57] R. Hill, "On constitutive inequalities for simple materials-1," *Journal of the Mechanics and Physics of Solids*, vol. 16, no. 4, pp. 229–242, 1968.
- [58] D. Tjahjanto, S. Turteltaub, and S. Zwaag, "Modelling of the effects of grain orientation on transformation-induced plasticity in multiphase carbon steels," *Modelling and Simulation in Materials Science and Engineering*, 14 (4), vol. 14, 06 2006.
- [59] F. Qayyum, A. A. Chaudhry, S. Guk, M. Schmidtchen, R. Kawalla, and U. Prahl, "Effect of 3d representative volume element (rve) thickness on stress and strain partitioning in crystal plasticity simulations of multi-phase materials," *Crystals*, vol. 10, no. 10, 2020.
- [60] M. Umar, F. Qayyum, M. U. Farooq, A. Khan, S. Guk, and U. Prahl, "Investigating the effect of cementite particle size and distribution on local stress and strain evolution in spheroidized medium carbon steels using crystal plasticity-based numerical simulations," *steel research international*, vol. 89, 11 2020.

- [61] F. Qayyum, S. Guk, S. Prüger, M. Schmidtchen, I. Saenko, B. Kiefer, R. Kawalla, and U. Prahl, “Investigating the local deformation and transformation behavior of sintered x3crmmni16-7-6 trip steel using a calibrated crystal plasticity-based numerical simulation model,” *International Journal of Materials Research (formerly Zeitschrift fuer Metallkunde)*, vol. 111, pp. 1–13, 04 2020.
- [62] F. Roters, M. Diehl, P. Shanthraj, P. Eisenlohr, C. Reuber, S. Wong, T. Maiti, A. Ebrahimi, T. Hochrainer, H.-O. Fabritius, S. Nikolov, M. Friák, N. Fujita, N. Grilli, K. Janssens, N. Jia, P. Kok, D. Ma, F. Meier, E. Werner, M. Stricker, D. Weygand, and D. Raabe, “Damask - the düsseldorf advanced material simulation kit for modeling multi-physics crystal plasticity, thermal, and damage phenomena from the single crystal up to the component scale,” *Computational Materials Science*, vol. 158, pp. 420–478, 2019.
- [63] NS, “Curve intersections - matlab central file exchange,” 2023.
- [64] J. Hidalgo, M. Vittoriotti, H. Farahani, F. Vercruysse, R. Petrov, and J. Sietsma, “Influence of m23c6 carbides on the heterogeneous strain development in annealed 420 stainless steel,” *Acta Materialia*, vol. 200, pp. 74–90, 2020.
- [65] H. Shin, Y. Ju, M. K. Choi, and D. H. Ha, “Flow stress description characteristics of some constitutive models at wide strain rates and temperatures,” *Technologies*, vol. 10, no. 2, 2022.
- [66] S.-K. Kang, Y.-C. Kim, K.-H. Kim, D. Kwon, and J.-Y. Kim, “Constitutive equations optimized for determining strengths of metallic alloys,” *Mechanics of Materials*, vol. 73, pp. 51–57, 2014.
- [67] E. Doege, T. Hallfeld, Y. Khalfalla, and K. Benyounis, “Metal working: Stretching of sheets,” 12 2016.
- [68] Z. Shao, C. Zhang, Y. Li, H. Shen, D. Zhang, X. Yu, and Y. Zhang, “A review of non-destructive evaluation (nde) techniques for residual stress profiling of metallic components in aircraft engines,” *Aerospace*, vol. 9, no. 10, 2022.
- [69] X. He and Y. Yao, “A dislocation density-based viscoplasticity model for cyclic deformation: Application to p91 steel,” *International Journal of Applied Mechanics*, vol. 10, 06 2018.
- [70] S. Bao, T. Erber, S. Guralnick, and W. Jin, “Fatigue, magnetic and mechanical hysteresis,” *Strain*, vol. 47, 01 2010.
- [71] D. Jackiewicz, M. Kachniarz, and A. Bieńkowski, “Investigation of the magnetoelastic villari effect in steel truss,” in *Recent Global Research and Education: Technological Challenges* (R. Jabłoński and R. Szewczyk, eds.), (Cham), pp. 63–70, Springer International Publishing, 2017.
- [72] K. Verbeken, E. Gomes, J. Schneider, and Y. Houbaert, “Correlation between the magnetic properties and the crystallographic texture during the processing of non oriented electrical steel,” *Solid State Phenomena*, vol. 160, 02 2010.
- [73] J. Mohapatra, S. Mohanty, D. S. Kumar, and I. Tripathy, “Correlation of magnetic properties with mechanical properties of a high tensile grade steel in various heat treated conditions,” *Transactions of the Indian Institute of Metals*, vol. 71, 07 2018.

- [74] Y. Zhang, Z. Wang, Y. Wang, Z. Zhang, and Z. Yisheng, "A study on the relationship between hardness and magnetic properties of ultra-high strength steel," *Advanced Materials Research*, vol. 1063, pp. 78–81, 12 2014.
- [75] T. SASAKI, K. WATANABE, K. NOHARA, Y. ONO, N. KONDO, and S. SATO, "Physical and mechanical properties of high manganese non-magnetic steel and its application to various products for commercial use," *Transactions of the Iron and Steel Institute of Japan*, vol. 22, no. 12, pp. 1010–1020, 1982.
- [76] M. Eftekhari, M. Moallem, S. Sadri, A. Sadeghi, M. A. Ghadamyari, D. Asefi, and H. Monajati, "Predicting mechanical properties of cold rolled low carbon steel based on magnetic parameter measurement using artificial neural network," in *2010 International Conference on Computer Applications and Industrial Electronics*, pp. 677–682, 2010.
- [77] I. Ahadi Akhlaghi, S. Kahrobaee, M. Sekhavat, H. Norouzi Sahraei, and F. Akhlaghi Modiri, "Application of artificial neural network and multi-magnetic nde methods to determine mechanical properties of plain carbon steels subjected to tempering treatment," *International Journal of Engineering*, vol. 34, no. 4, pp. 919–927, 2021.
- [78] X. Hao, W. Yin, M. Strangwood, A. Peyton, P. Morris, and C. Davis, "Modelling the electromagnetic response of two-phase steel microstructures," *NDT & E International*, vol. 43, no. 4, pp. 305–315, 2010.
- [79] K. T. McDonald, "Voltage drop, potential difference and emf," 01 2018.
- [80] S. Makarov, R. Ludwig, and J. Bitar, *Electric Transformer and Coupled Inductors*. Springer, 01 2016.
- [81] F. W. Grover, "Tables for the calculation of the mutual inductance of circuits with circular symmetry about a common axis," *scientific papers for the bureau of standards*, 1924.
- [82] E. B. Rosa and F. W. Grover, "Formulas and tables for the calculation of mutual and self-inductance (revised)," *Bulletin of the Bureau of Standards*, vol. 8, p. 1, 1916.

A. Validation

A.1 Benchmark 1: Two coils in free space

Consider two coils in free space as shown in Figure A.1. For these coils, the mutual inductance and self-inductance will be determined using the different post-processing methods mentioned in Section 2.6. The dimensions of this benchmark problem are given in Table A.1. First of all, the low-frequency mutual and self-inductance are determined from the

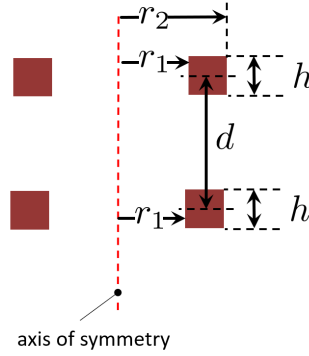


Figure A.1: Schematic overview of the two coils in free space.

Table A.1: The dimensions of the free coils. Note N is the number of windings.

r_1 [m]	r_2 [m]	h [m]	d [m]	N
0.084855	0.085145	0.025	0.07	200

simulations. The resulting inductances from the different post-processing methods will be compared to the theoretical expression for the inductance which is given in D. Based on the equations in D it is found that the theoretical values for self-inductance and mutual inductance are 11.976 [mH] and 2.97133 [mH], respectively. In Figure A.2 the numerically obtained self and mutual inductance, M_n , concerning the theoretical values, M_t , are shown for different levels of mesh refinement.

Second, it is studied whether the frequency dependency for all methods is realistic. This is done based on a theoretical expression for the inductance, which is derived in Appendix C. The resulting mutual and self-inductance for all derived methods are compared in figures A.3 and A.4, respectively.

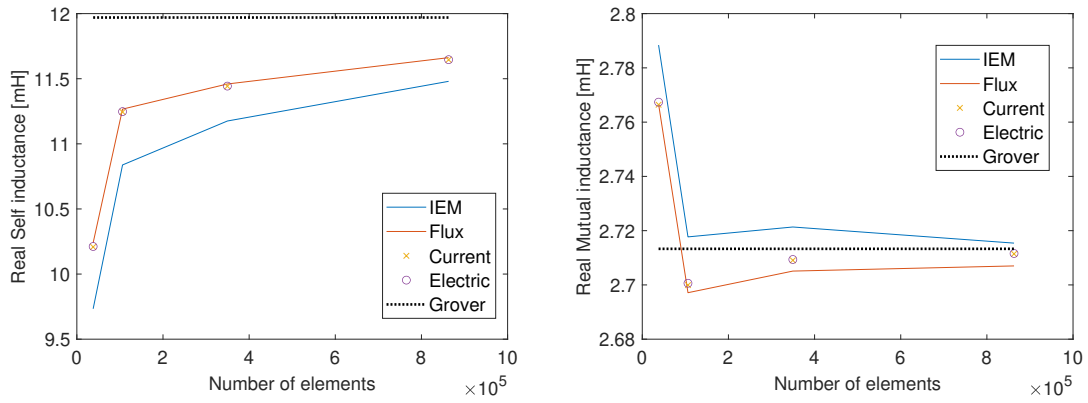


Figure A.2: The convergence of the error during mesh refinement.

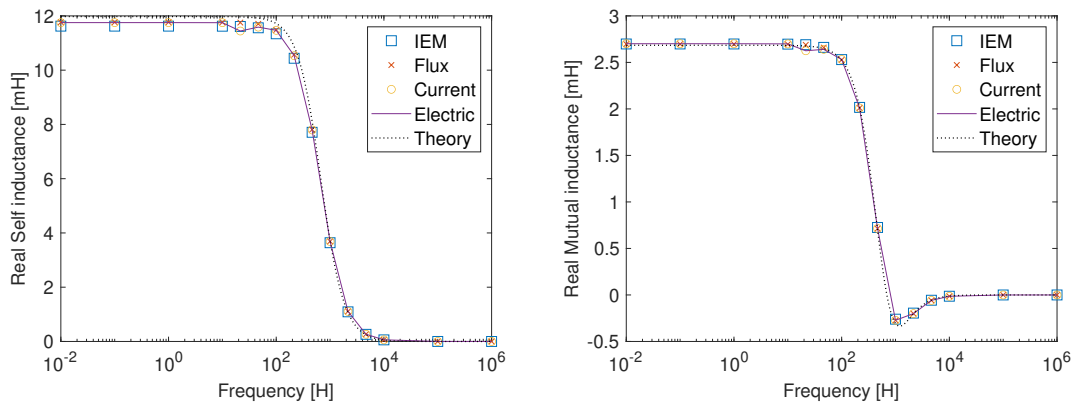


Figure A.3: Figure showing the resulting values for the real part of the mutual and self-inductance for a range of frequencies.

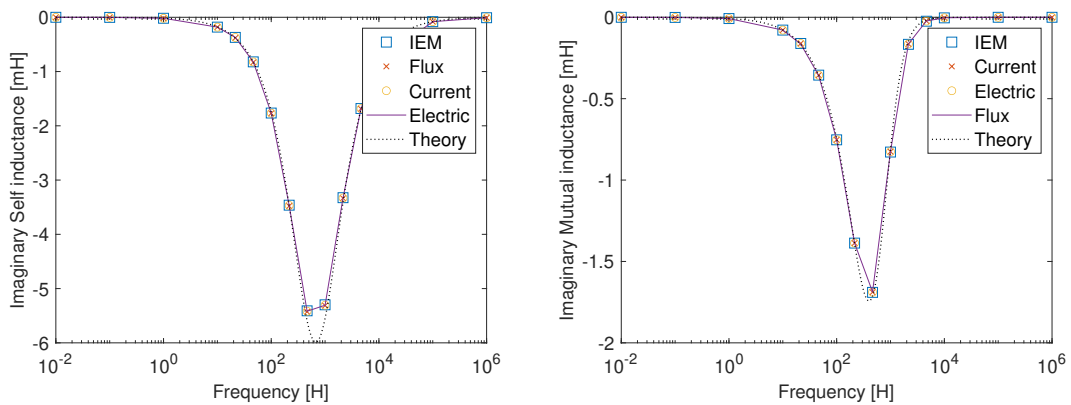


Figure A.4: Figure showing the resulting values for the imaginary part of the mutual and self-inductance for a range of frequencies.

A.2 Benchmark 2: Sensor

In the last test, the results for the different post-processing methods are compared to the actual sensor set-up. Different simulations are done in which the stabilization factor, coil conductivity, and frequency are varied. The results can be seen in Figure A.5, A.6 and

A.7.

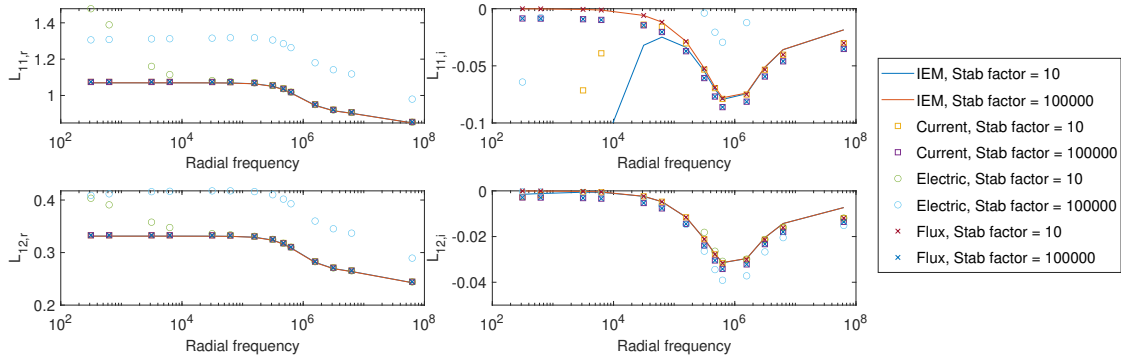


Figure A.5: Inductance calculated for different stabilization factors and methods using a coil conductivity of 1.

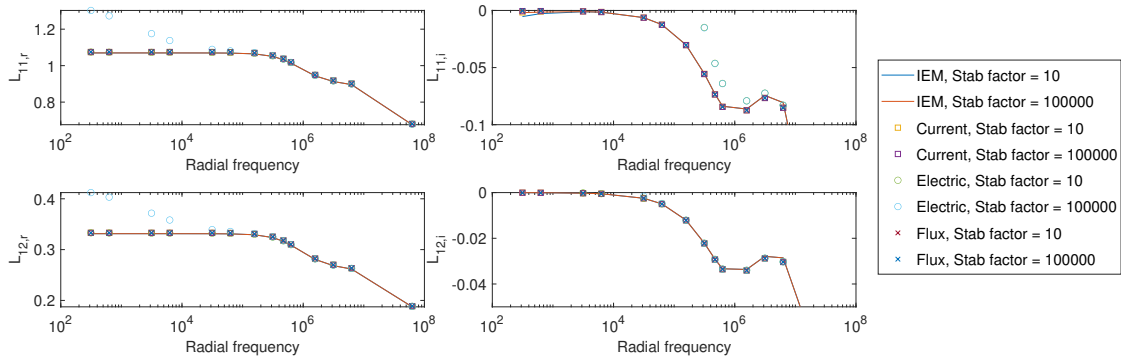


Figure A.6: Inductance calculated for different stabilization factors and methods using a coil conductivity of 58.14e6.

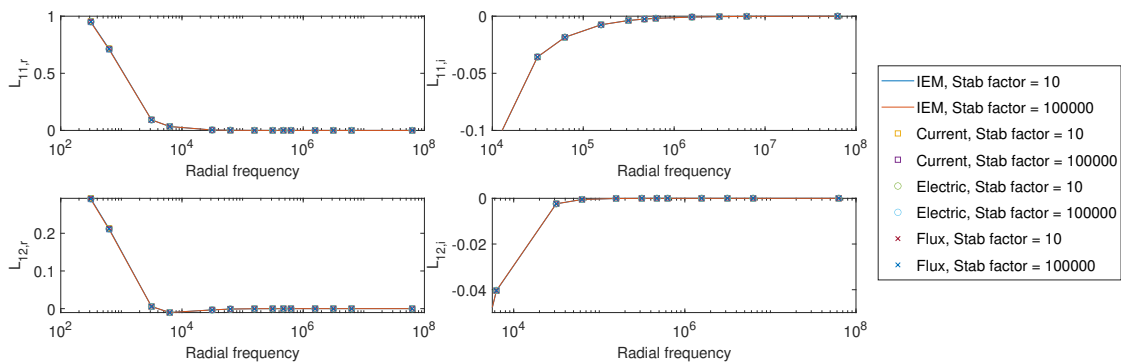


Figure A.7: Inductance calculated for different stabilization factors and methods using a coil conductivity of 58.14e6.

It can be seen that when the coil conductivity of the coil is high all methods provide generally similar results. However, when the coil conductivity is very low this is not the case. In Figure A.5 it can be seen that there are large differences between the methods. The right solution is assumed to be given by both the IEM method at a stabilization

factor of $1e6$ and the Flux and Current method at a stabilization factor of 10. The reason is that these solutions lie exactly on top of each other even though they cover completely different domains. Additionally, the shape of the curves is as expected. A summary of which methods are appropriate in for which frequencies is given below.

σ_{coil} [S/m]	$k_{\text{stabilization}}$	IEM method	Flux method	Electric method	Current method
1	10	HF	all	none	all
1	$1e6$	all	none	none	HF
500	100	all	all	all	all
500	$1e6$	all	all	none	all
$58.14e6$	10	all	all	all	all
$58.14e6$	$1e6$	all	all	all	all

Table A.2: A table giving an overview for which frequencies the different methods provide accurate results depending on the conductivity of the coils, σ_{coil} , and the stabilization factor, $k_{\text{stabilization}}$, used in the simulations.

B. Discretization of inductance computations

In this chapter, four different post-processing methods will be shown to obtain the mutual and self-inductance from the simulation results. In the subsections of this chapter the time dependent variables and phasors of the time dependent variables are represented in the same way. Whether the variable is a phasor or not is clear from the context.

B.1 Flux method

Consider the image shown in B.1 in which two half of two coils are shown. A schematic overview of this picture is given in Figure B.2. The set of elements in the volume inside the coil will be referred to as Ω , illustrated in Figure B.1 as the grey volume and in Figure B.2 indicated. The induced electromotive force, \mathcal{U} , in the segment of the coil around Ω

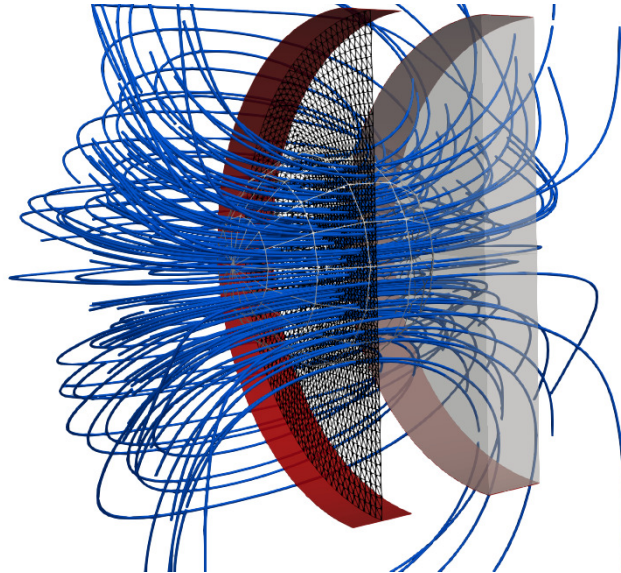


Figure B.1: An illustration of where the integration is done. The black lines show the elements of set Ω . The grey volume shows in which region the integration is done.

can be described using

$$\mathcal{U}_{\Omega} = \int_{\mathcal{C}} \mathbf{E} \cdot d\mathbf{l} = -\frac{d}{dt} \int_{\mathcal{A}_{ic}} \mathbf{B} \cdot d\mathbf{A}. \quad (\text{B.1})$$

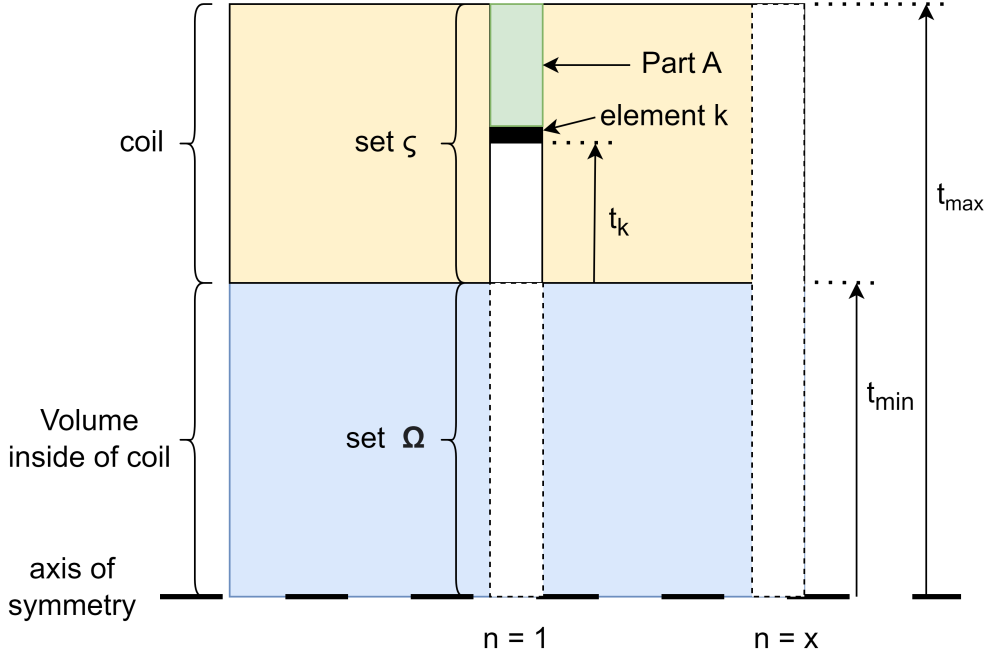


Figure B.2: Figure illustrating loop of interest.

When it is assumed that the response is time-harmonic it means that $d\mathbf{B}/dt = i\omega\mathbf{B}$. This can be used to rewrite Equation B.1 into

$$\mathcal{U}_\Omega = -i\omega \int_{A_{ic}} \mathbf{B} \cdot d\mathbf{A}. \quad (\text{B.2})$$

In footnote 19 in [79] it is explained that for some continuous surface the integral can be obtained using the centroidal element values. Discretization and assuming that the element length in the axial direction of the elements is constant the equation can be rewritten to

$$\mathcal{U}_\Omega = -i\omega \sum_{j=1}^{N_\Omega} B_j \frac{V_j}{h_j} = -i\frac{\omega}{h_j} \sum_{j=1}^{N_\Omega} B_j V_j. \quad (\text{B.3})$$

Where h_j is the axial length of an element and V_j is the volume for each element. The actual voltage in the coil will be higher because the magnetic field in the coil will also produce an electromotive force. Consider some element inside of the coil, k , this element will only induce a current in the 'outer' part of the coil, which will be referred to as part A. See figure B.2. The induced current in part A can be found using equation B.4, which is given by

$$\mathcal{I}_{\text{ind,A}} = \frac{\mathcal{EMF}}{\mathcal{R}_A} = \frac{\mathcal{EMF}}{(t_{\text{max}} - t_{\text{min}})/(t_{\text{max}} - t_k)\mathcal{R}_{\text{coil}}} = \frac{t_{\text{max}} - t_k}{t_{\text{max}} - t_{\text{min}}} \frac{\mathcal{EMF}_k}{R_{\text{coil}}}. \quad (\text{B.4})$$

Equation B.3 can be used to get $\mathcal{EMF}_k = -i\omega/h_k \sum_{k=1}^{N_\Omega} B_k V_k$. Combining this with Ohms law gives the expression for the voltage induced by the elements in the coil, \mathcal{U}_ζ ,

$$\mathcal{U}_\zeta = i\frac{\omega}{h_j} \sum_{k=1}^{N_\zeta} \left(\frac{t_{\text{max}} - t_k}{t_{\text{coil}}} B_k V_k \right), \quad (\text{B.5})$$

where t_{coil} is $t_{\text{max}} - t_{\text{min}}$ and N_{ζ} is the number of elements in the coil. The total voltage, \mathcal{U} , can be obtained by summing \mathcal{U}_{Ω} and \mathcal{U}_{ζ} to obtain

$$\mathcal{U} = -i \frac{\omega}{h_j} \left[\sum_{j=1}^{N_{\Omega}} (B_j V_j) - \sum_{k=1}^{N_{\zeta}} \left(\frac{t_{\text{max}} - t_k}{t_{\text{coil}}} B_k V_k \right) \right], \quad (\text{B.6})$$

The average voltage over all the cross sections of the coil can be averaged analogous to [14]. In Figure B.2 two of these cross sections are illustrated (cross-section number 1 and cross-section number x). The resulting expression for the average voltage is given by

$$\mathcal{U}_{\text{av}} = \frac{1}{N_{\text{loops}}} \sum_{n=1}^{N_{\text{loops}}} \mathcal{U}_n. \quad (\text{B.7})$$

Combining Equations B.6, B.7 and using that the height of the coil is given by $h_{\text{coil}} = N_{\text{loops}} h_j$ gives

$$\mathcal{U} = -i \frac{\omega}{h_j} \left[\sum_{j=1}^{N_{\text{el,ic}}} (B_j V_j) - \sum_{k=1}^{N_{\text{el,c}}} \left(\frac{t_{\text{max}} - t_k}{t_{\text{coil}}} B_k V_k \right) \right], \quad (\text{B.8})$$

where $N_{\text{el,ic}}$ is the number of elements in the volume inside the coil and $N_{\text{el,c}}$ is the number of elements of the coil. The relation between the amplitudes of the voltage and the magnetic potential can be found using $\mathcal{U} = d\Phi/dt$. This means that the amplitudes of both signals are related through

$$\mathcal{U} = i\omega\Phi. \quad (\text{B.9})$$

Combining Equations B.9 and B.8 gives

$$\Phi = \frac{1}{h_{\text{coil}}} \left[\sum_{j=1}^{N_{\text{el,ic}}} (B_j V_j) - \sum_{k=1}^{N_{\text{el,c}}} \left(\frac{t_{\text{max}} - t_k}{t_{\text{coil}}} B_k V_k \right) \right]. \quad (\text{B.10})$$

Using $\mathcal{L} = \Phi/\mathcal{I}$ and incorporating the number of windings of the coil into the equation gives

$$\mathcal{L} = \frac{N_w}{h_{\text{coil}} \mathcal{I}} \left[\sum_{j=1}^{N_{\text{el,ic}}} (B_j V_j) - \sum_{k=1}^{N_{\text{el,c}}} \left(\frac{t_{\text{max}} - t_k}{t_{\text{coil}}} B_k V_k \right) \right]. \quad (\text{B.11})$$

This is the expression for the real part of the inductance. Doing the same for the imaginary part of the inductance gives the following expressions

$$\mathcal{L}_{\text{Re}} = \text{Re} \left(\frac{N_w}{h_{\text{coil}} \mathcal{I}} \left[\sum_{j=1}^{N_{\text{el,ic}}} (B_j V_j) - \sum_{k=1}^{N_{\text{el,c}}} \left(\frac{t_{\text{max}} - t_k}{t_{\text{coil}}} B_k V_k \right) \right] \right) \quad \text{and} \quad (\text{B.12})$$

$$\mathcal{L}_{\text{Im}} = \text{Im} \left(\frac{N_w}{h_{\text{coil}} \mathcal{I}} \left[\sum_{j=1}^{N_{\text{el,ic}}} (B_j V_j) - \sum_{k=1}^{N_{\text{el,c}}} \left(\frac{t_{\text{max}} - t_k}{t_{\text{coil}}} B_k V_k \right) \right] \right), \quad (\text{B.13})$$

where the self-inductance can be obtained by taking the values of $\sum_{i=1}^{N_{\text{el,ic}}} B_i V_i$ in the actuating coil. On the other hand, the mutual inductance can be obtained by taking the values of $\sum_{i=1}^{N_{\text{el,ic}}} B_i V_i$ in the coil that is not excited.

B.2 Electric field method

Consider a loop of elements in a coil as shown in black in Figure B.3. The elements in this set will be called Ψ . The voltage over some loop can be related to the electric field in this

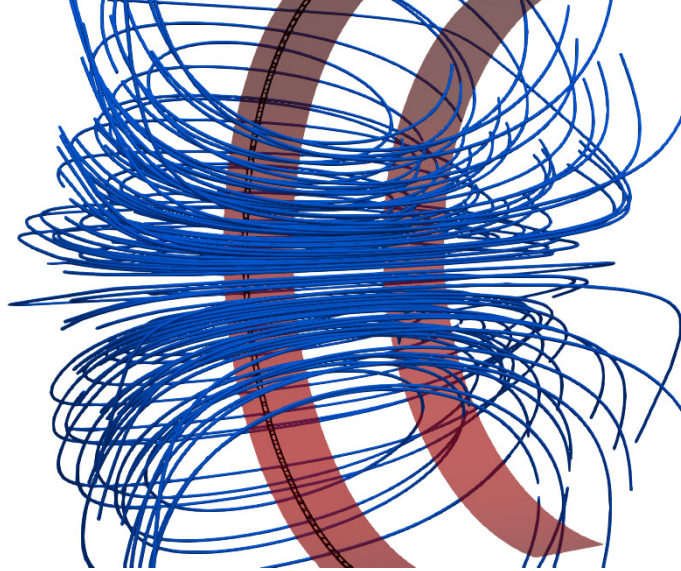


Figure B.3: Illustration of the set that is analyzed. The element drawn as black lines corresponds to set Ψ .

loop using Equation B.14.

$$\mathcal{U} = \int_{\text{loop}} \mathbf{E} \cdot d\mathbf{l} \quad (\text{B.14})$$

The integral in Equation B.14 can be discretized using the centroidal element values [79] which gives

$$\mathcal{U} = \sum_{j=1}^{N_{\Psi}} (\Delta l_{\parallel,j} E_{\parallel,j} + \Delta l_{\perp,j} E_{\perp,j}). \quad (\text{B.15})$$

In this equation, l_{\perp} and l_{\parallel} are the element length in perpendicular and parallel direction relative to the coil. Furthermore, E_{\perp} and E_{\parallel} are the perpendicular and parallel components of the electric field relative to the coil, respectively. Assuming that the loop is a perfect circle this can be further simplified to

$$\mathcal{U} = \sum_{j=1}^{N_{\Psi}} \Delta l_{\parallel,j} E_{\parallel,j}. \quad (\text{B.16})$$

Assuming that the element length in angular direction is constant and rewriting gives

$$\mathcal{U} = \frac{\Delta l_{\parallel} N_{\Psi}}{N_{\Psi}} \sum_{\Psi} E_{\parallel} = \frac{L_p}{N_{\Psi}} \sum_{j=1}^{N_{\Psi}} E_{\parallel,j}, \quad (\text{B.17})$$

where N_{Ψ} is the number of elements in Ψ and L_p is the perimeter of the coil. The same derivation can be done for all loops in the coil shown in Figure B.3. The voltage can

averaged using Equation B.7, combining the average voltage with Equation B.17 gives

$$\mathcal{U}_{\text{av}} = \frac{1}{N_{\Psi}} \frac{L_p}{N_{\text{loops}}} \sum_{j=1}^{N_{\text{loops}} \cdot N_{\Psi}} E_{\parallel,j} = \frac{L_p}{N_{\text{el},c}} \sum_{j=1}^{N_{\text{el},c}} E_{\parallel,j}, \quad (\text{B.18})$$

where $N_{\text{el},c}$ is the total number of elements in the coil and r is the mean radius of the coil. Using Equation B.9 the equation can be modified to obtain

$$\Phi = i \frac{L_p}{N_{\text{el},c}} \sum_{j=1}^{N_{\text{el},c}} E_{\parallel,j}. \quad (\text{B.19})$$

Using $\mathcal{L} = \Phi/\mathcal{I}$ and incorporating the number of windings of the coil, N_w , into the equation gives

$$\mathcal{L} = i \frac{L_p N_w}{N_{\text{el},c} \omega \mathcal{I}} \sum_{j=1}^{N_{\text{el},c}} E_{\parallel,j}. \quad (\text{B.20})$$

This is the expression for the real part of the inductance. Doing the same for the imaginary part of the inductance gives the following expressions

$$\mathcal{L}_{\text{Re}} = \text{Re} \left(i \frac{L_p N_w}{N_{\text{el},c} \omega \mathcal{I}} \sum_{j=1}^{N_{\text{el},c}} E_{\parallel,j} \right) \quad \text{and} \quad \mathcal{L}_{\text{Im}} = \text{Im} \left(i \frac{L_p N_w}{N_{\text{el},c} \omega \mathcal{I}} \sum_{j=1}^{N_{\text{el},c}} E_{\parallel,j} \right). \quad (\text{B.21})$$

Now it is used that $\text{Im}(A) = \text{Re}(A/i)$ and $\text{Im}(Ai) = \text{Re}(-A)$. This can be used to remove the complex number as seen below

$$\boxed{\mathcal{L}_{\text{Re}} = \text{Im} \left(\frac{L_p N_w}{N_{\text{el},c} \omega \mathcal{I}} \sum_{j=1}^{N_{\text{el},c}} E_{\parallel,j} \right)} \quad \text{and} \quad \boxed{\mathcal{L}_{\text{Im}} = \text{Re} \left(-\frac{L_p N_w}{N_{\text{el},c} \omega \mathcal{I}} \sum_{j=1}^{N_{\text{el},c}} E_{\parallel,j} \right)}, \quad (\text{B.22})$$

where the self-inductance can be obtained by taking the values of $\sum_{j=1}^{N_{\text{el},c}} E_{\parallel,j}$ in the actuating coil. On the other hand, the mutual inductance can be obtained by taking the values of $\sum_{j=1}^{N_{\text{el},c}} E_{\parallel,j}$ in the coil that is not excited.

B.3 Current method

Consider a coil that has been sliced in a radial direction two times. The elements that remain left represent a cross-section of the coil. This idea is illustrated in Figure B.4 where the elements of interest are represented by black squares. These elements will be referred to as the set Ξ . The following definition is used to calculate the current over some cross-section, \mathcal{I}_C

$$\mathcal{I}_C = \int_{\mathcal{A}_c} \mathbf{J} \cdot d\mathbf{A}, \quad (\text{B.23})$$

where \mathcal{A}_c is the cross-sectional area of the coil. Discretization of Equation B.23 and rewriting gives

$$\mathcal{I}_C = \sum_{j=1}^{N_{\Xi}} \mathbf{J}_j \cdot \mathbf{A}_j = \sum_{j=1}^{N_{\Xi}} \mathbf{J}_j \cdot \frac{V_j}{l_j} = \sum_{j=1}^{N_{\Xi}} J_{\parallel} \frac{V_j}{l_{\parallel}} + J_{\perp} \frac{V_j}{l_{\perp}}. \quad (\text{B.24})$$

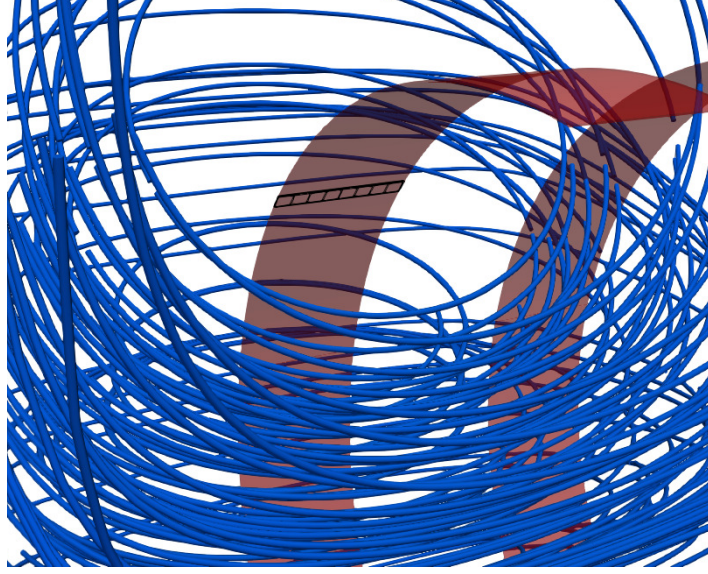


Figure B.4: Illustration of the region that is analyzed. The set Ξ is illustrated with black lines.

Where the subscripts \perp and \parallel refer to the the components perpendicular and parallel to the coil. Next, it is assumed that the element length in parallel direction is constant as well as that the current density in normal direction to the coil, J_{\perp} , is zero. This gives

$$\mathcal{I}_C = \frac{1}{l_{\parallel,j}} \sum_{j=1}^{N_{\Xi}} J_{\parallel,j} A_j. \quad (\text{B.25})$$

The average current over all cross-sections parallel to the one shown in Figure B.4 can be written as

$$\mathcal{I}_{\text{av}} = \frac{1}{N_C} \sum_{j=1}^{N_C} \mathcal{I}_{C,i}, \quad (\text{B.26})$$

where $N_{c,m}$ is the number of modelled cross sections. The number of modeled cross sections is equal to the total number of cross sections, N_C , divided by the symmetry multiplier, k_{sym} .

$$N_{c,m} = \frac{N_C}{k_{\text{sym}}} \quad (\text{B.27})$$

Combining Equations B.25 and B.26 and using that only a quarter of the circumference is simulated gives

$$\mathcal{I} = \frac{1}{\frac{1}{k_{\text{sym}}} 2\pi r} \sum_{j=1}^{N_{\text{el},c}} J_{\parallel,j} V_j, \quad (\text{B.28})$$

where $N_{\text{el},c}$ is the number of elements in the coil in the simulation. Using the equation for voltage, $\mathcal{U} = \mathcal{R}\mathcal{I}$, and for resistance, $\mathcal{R} = L_p/A_C\sigma$, gives

$$\mathcal{U} = k_{\text{sym}} \frac{L_p}{L_p A_C \sigma} \sum_{j=1}^{N_{\text{el},c}} J_{\parallel,j} V_j, \quad (\text{B.29})$$

where A_C is the area of the cross-section of the coil and σ is the conductivity. Using Equation B.9 means the expression can be rewritten to

$$\Phi = i \frac{k_{\text{sym}}}{A_C \sigma \omega} \sum_{j=1}^{N_{\text{el},c}} J_{\parallel,j} V_j. \quad (\text{B.30})$$

Using $\mathcal{L} = \Phi/\mathcal{I}$ and incorporating the number of windings of the coil into the equation gives

$$\mathcal{L} = i \frac{k_{\text{sym}} N_w}{\mathcal{I} A_C \sigma \omega} \sum_{j=1}^{N_{\text{el},c}} J_{\parallel,j} V_j, \quad (\text{B.31})$$

where the complex inductances can be expressed as

$$\mathcal{L}_{\text{Re}} = \text{Re} \left(i \frac{k_{\text{sym}} N_w}{\mathcal{I} A_C \sigma \omega} \sum_{j=1}^{N_{\text{el},c}} J_{\parallel,j} V_j \right) \quad \text{and} \quad \mathcal{L}_{\text{Im}} = \text{Im} \left(i \frac{k_{\text{sym}} N_w}{\mathcal{I} A_C \sigma \omega} \sum_{j=1}^{N_{\text{el},c}} J_{\parallel,j} V_j \right). \quad (\text{B.32})$$

Now it is used that $\text{Im}(A) = \text{Re}(A/i)$ and $\text{Im}(Ai) = \text{Re}(-A)$. This can be used to remove the complex number as seen below

$$\boxed{\mathcal{L}_{\text{Re}} = \text{Im} \left(\frac{k_{\text{sym}} N_w}{\mathcal{I} A_C \sigma \omega} \sum_{j=1}^{N_{\text{el},c}} J_{\parallel,j} V_j \right)} \quad \text{and} \quad \boxed{\mathcal{L}_{\text{Im}} = \text{Re} \left(-\frac{k_{\text{sym}} N_w}{\mathcal{I} A_C \sigma \omega} \sum_{j=1}^{N_{\text{el},c}} J_{\parallel,j} V_j \right)}, \quad (\text{B.33})$$

where the self-inductance can be obtained by taking the values of $\sum_{j=1}^{N_{\text{el},c}} J_{\parallel,j} V_j$ in the actuating coil. On the other hand, the mutual inductance can be obtained by taking the values of $\sum_{j=1}^{N_{\text{el},c}} J_{\parallel,j} V_j$ in the coil that is not excited. Note that if for example a quarter of the coil is modeled then the value of k_{sym} has a value of 4.

C. High frequent theoretical inductance calculations

C.1 Theoretic expression self-inductance

In the following study, the exciting coil is excited with different frequencies. The resulting real and imaginary inductances obtained from simulations can be seen in Figure A.3 and A.4, respectively. Apart from the simulated inductances also an analytical expression is used to calculate the inductance for different frequencies. This expression will be derived below. The voltage when there is no induced voltage, \mathcal{U}_0 , is given by

$$\mathcal{U}_0 = \mathcal{I}_0 \mathcal{R}. \quad (\text{C.1})$$

Where \mathcal{I}_0 is the current excitation and where \mathcal{R} is given by

$$\mathcal{R} = \frac{l}{\sigma A_w}. \quad (\text{C.2})$$

Where l is the length of the wire, which is a function of the number of windings, N_w , and is given by $l = N_w 2\pi r$. A_w is the area of the wire which is given by $A_w = A_c / N_w$, where A_c is the cross-section of the coil. This can be used to write the \mathcal{R} as

$$\mathcal{R} = N_w^2 \frac{2\pi r}{\sigma A_c}. \quad (\text{C.3})$$

When an EMF is created the reduced current can be calculated using

$$\mathcal{I}_{red} = \frac{\mathcal{U}_0}{\mathcal{Z}}. \quad (\text{C.4})$$

Where \mathcal{Z} is the impedance and is given by $\mathcal{Z} = \mathcal{R} + j\omega \mathcal{L}_{11,lf}$. Next, the low-frequency self-inductance value can be used to express the magnetic potential in the reduced current using, $\mathcal{L}_{11,lf} = \Phi / \mathcal{I}_{red}$. This expression can be used to express the actual self-inductance which is defined as $\mathcal{L}_{11} = \Phi / \mathcal{I}_0$. Combining these expression for self inductance with Equations C.4 and C.1 gives

$$\mathcal{L}_{11} = \frac{\mathcal{L}_{11,lf} \mathcal{I}_0 \mathcal{R}}{\mathcal{R} + j\omega \mathcal{L}_{11,lf}}. \quad (\text{C.5})$$

This can be used to obtain a frequency-dependent expression for the real self-inductance, $\mathcal{L}_{11,re}$, and imaginary self-inductance, $\mathcal{L}_{11,im}$,

$$\boxed{\mathcal{L}_{11,im}(\omega) = \text{Im} \left(\frac{\mathcal{U}_0 \mathcal{R}}{\mathcal{I}_0 \omega (\mathcal{R} + j\omega \mathcal{L}_{11,lf})} \right)} \text{ and} \quad (\text{C.6})$$

$$\boxed{\mathcal{L}_{11,re}(\omega) = \text{Re} \left(\frac{\mathcal{U}_0 \mathcal{R}}{\mathcal{I}_0 \omega (\mathcal{R} + j\omega \mathcal{L}_{11,lf})} \right)}. \quad (\text{C.7})$$

Where \mathcal{R} is given in Equation C.3 and $\mathcal{L}_{11,lf}$ is given by Equation A.6 in D. The resulting values of $\mathcal{L}_{11,re}(\omega)$ and $\mathcal{L}_{11,im}(\omega)$ can be seen in figures A.3 and A.4, respectively.

C.2 Theoretic expression mutual inductance

In this part, an expression will be derived for the mutual inductance. In this section, the subscript e refers to the exciting coil and the subscript n refers to the non-excited coil. For some initial voltage, the reduced current in the exciting coil can be found using

$$\mathcal{I}_{\text{red,e}} = \frac{\mathcal{U}_{0,e}}{\mathcal{Z}_e}. \quad (\text{C.8})$$

This can then be used to calculate the voltage in the exciting coil using

$$\mathcal{U}_{\text{red,e}} = \mathcal{I}_{\text{red,e}} \mathcal{R}_e. \quad (\text{C.9})$$

The voltage in the non-excited coil can then be calculated using [80]. In 12.56 in [80] an expression is given for the current in a perfect coupled conductor as a function of the voltage. The expression is repeated below.

$$\mathcal{I}_n = \frac{\mathcal{U}_{\text{red,e}}}{j\omega \frac{\mathcal{M}^2 - \mathcal{L}_n \mathcal{L}_e}{\mathcal{M}} - \frac{\mathcal{L}_e \mathcal{R}_n}{\mathcal{M}}} \quad (\text{C.10})$$

Where \mathcal{L}_n and \mathcal{L}_e are the low frequency self inductances of the non-excited and excited coil, respectively. Furthermore, \mathcal{M} , is the low frequency mutual inductance and will be written as $\mathcal{L}_{12,\text{lf}}$. Using that the voltage in the non excited coil, \mathcal{U}_n , is given by $\mathcal{U}_n = \mathcal{I}_n \mathcal{R}_n$ and rewriting gives

$$\frac{\mathcal{U}_n}{\mathcal{U}_{\text{red,e}}} = \frac{\mathcal{L}_{12,\text{lf}} \mathcal{R}_n}{j\omega \left(\mathcal{L}_{12,\text{lf}}^2 - \mathcal{L}_{11,\text{lf,n}} \mathcal{L}_{11,\text{lf,e}} \right) - \mathcal{L}_{11,\text{lf,e}} \mathcal{R}_n}. \quad (\text{C.11})$$

Combining equations C.8, C.9 and C.11 gives

$$\mathcal{U}_n = \frac{\mathcal{U}_{0,e} \mathcal{R}_e}{\mathcal{Z}_e} \frac{\mathcal{L}_{12,\text{lf}} \mathcal{R}_n}{j\omega \left(\mathcal{L}_{12,\text{lf}}^2 - \mathcal{L}_{11,\text{lf,n}} \mathcal{L}_{11,\text{lf,e}} \right) - \mathcal{L}_{11,\text{lf,e}} \mathcal{R}_n}. \quad (\text{C.12})$$

Using that the current in the non-excited coil is given by $\mathcal{U}_n = \mathcal{I}_n \mathcal{R}_n$ and that the resistance of both coils is equal gives

$$\mathcal{I}_n = \frac{\mathcal{U}_{0,e} \mathcal{R}_e}{(\mathcal{R}_e + j\omega \mathcal{L}_{11,\text{lf,e}})} \frac{\mathcal{L}_{12,\text{lf}}}{j\omega \left(\mathcal{L}_{12,\text{lf}}^2 - \mathcal{L}_{11,\text{lf,n}} \mathcal{L}_{11,\text{lf,e}} \right) - \mathcal{L}_{11,\text{lf,e}} \mathcal{R}_n}. \quad (\text{C.13})$$

Using that $\Phi = \mathcal{L}_{11,\text{lf,n}} \mathcal{I}_n$ and that $\mathcal{L}_{12} = \Phi / \mathcal{I}_{0,e}$ gives

$$\mathcal{L}_{12,\text{re}}(\omega) = \text{Re} \left(\frac{\mathcal{U}_{0,e} \mathcal{L}_{11,\text{lf,n}} \mathcal{R}_e}{\mathcal{I}_{0,e} (\mathcal{R}_e + j\omega \mathcal{L}_{11,\text{lf,e}})} \frac{\mathcal{L}_{12,\text{lf}}}{j\omega \left(\mathcal{L}_{12,\text{lf}}^2 - \mathcal{L}_{11,\text{lf,n}} \mathcal{L}_{11,\text{lf,e}} \right) - \mathcal{L}_{11,\text{lf,e}} \mathcal{R}_n} \right), \quad (\text{C.14})$$

$$\mathcal{L}_{12,\text{re}}(\omega) = \text{Re} \left(\frac{\mathcal{U}_{0,e} \mathcal{L}_{11,\text{lf,n}} \mathcal{R}_e}{\mathcal{I}_{0,e} (\mathcal{R}_e + j\omega \mathcal{L}_{11,\text{lf,e}})} \frac{\mathcal{L}_{12,\text{lf}}}{j\omega \left(\mathcal{L}_{12,\text{lf}}^2 - \mathcal{L}_{11,\text{lf,n}} \mathcal{L}_{11,\text{lf,e}} \right) - \mathcal{L}_{11,\text{lf,e}} \mathcal{R}_n} \right). \quad (\text{C.15})$$

When both resistances and self-inductance are equal. The equations can be simplified into

$$\mathcal{L}_{12,\text{re}}(\omega) = \text{Re} \left(\frac{\mathcal{U}_{0,e} \mathcal{L}_{11,\text{lf,e}}}{\mathcal{I}_e (\mathcal{R} + j\omega \mathcal{L}_{11,\text{lf,e}})} \frac{k \mathcal{R}}{\mathcal{R} + j\omega \mathcal{L}_{11,\text{lf}} (1 - k^2)} \right) \text{ and} \quad (\text{C.16})$$

$$\mathcal{L}_{12,\text{im}}(\omega) = \text{Im} \left(\frac{\mathcal{U}_{0,\text{e}} \mathcal{L}_{11,\text{lf}}}{\mathcal{I}_{\text{e}} (\mathcal{R} + j\omega \mathcal{L}_{11,\text{lf}})} \frac{k\mathcal{R}}{\mathcal{R} + j\omega \mathcal{L}_{11,\text{lf}}(1 - k^2)} \right). \quad (\text{C.17})$$

Where \mathcal{R} is given in Equation C.3 and $\mathcal{L}_{11,\text{lf}}$ is given by Equation A.6 in D. The resulting values of $\mathcal{L}_{12,\text{re}}(\omega)$ and $\mathcal{L}_{12,\text{im}}(\omega)$ can be seen in figures A.3 and A.4, respectively.

D. Low frequent theoretical inductance calculations

D.1 Mutual inductance

In this subsection the mutual inductance for two equal coils will be given. This will be done by calculating the mutual inductance for two coaxial loops according to [81] and correcting for geometry according to [82]. The mutual inductance of two coaxial, M_0 , circles can be calculated using Equation D.1.

$$M_0 = f \cdot a \quad (\text{D.1})$$

$$k'^2 = \frac{d^2}{a^2 + d^2} \quad (\text{D.2})$$

Where a is the radius of the loops in cm and d is the distance between the planes of the loop in cm. The value of M_{12} has units μH . The value of f of is related to k'^2 through Table 2 in [81]. The interpolation between the values is done using linear interpolation, because the relation between k'^2 and f is almost linear near the origin. The correction due to the shape of the coils is made using Rosa's formula, which is Equation 49 in [82]. It is repeated below for convenience.

$$\begin{aligned} \Delta M = & 4\pi a \left[\frac{b^2}{12d^2} \left(1 + \frac{3d^2}{8a^2} \left[\log \frac{8a}{d} - \frac{11}{6} \right] - \frac{45d^4}{256a^4} \left[\log \frac{8a}{d} - \frac{97}{60} \right] \right. \right. \\ & \left. \left. + \frac{1050d^6}{128^2 a^6} \left[\log \frac{8a}{d} - \frac{3793}{2520} \right] \right) + \frac{1}{60} \frac{b^4}{d^4} \left(1 + \frac{1}{16} \frac{d^4}{a^4} \left[\log \frac{8a}{d} - \frac{187}{60} \right] \right) + \right. \\ & \frac{2100}{128^2} \left(\log \frac{8a}{d} - \frac{893}{420} \right) + \frac{1}{168} \frac{b^6}{d^6} \left(1 + \frac{3}{160} \frac{d^2}{a^2} - \frac{3}{1024} \frac{d^4}{a^4} \right) + \\ & \left. \frac{1}{360} \frac{b^8}{d^8} \left(1 + \frac{1}{112} \frac{d^2}{a^2} \right) \right] \quad (\text{D.3}) \end{aligned}$$

Where b is the axial length of the coil in cm and ΔM is the correction in inductance in μH . The effective mutual inductance, M_{12} , can then be calculated using

$$M_{12} = N^2 (M_0 + \Delta M) \quad (\text{D.4})$$

Where N is the number of loops in the coil. The resulting value for M_{12} is 2.7133 [mH].

D.2 Self inductance

In [82] two different suitable formulas can be found to calculate the self inductance. The first formula assumes the coil to be an infinitely thin sheet and can be found in Equation

70 in [82]. It is repeated below for convenience.

$$L = 4\pi a N^2 \left[\log \frac{8a}{b} - \frac{1}{2} + \frac{b^2}{32a^2} \left[\log 8ab + \frac{1}{4} \right] - \frac{1}{1024} \frac{b^4}{a^4} \left(\log \frac{8a}{b} - \frac{2}{3} \right) \right. \\ \left. + \frac{10}{131072} \frac{b^6}{a^6} \left(\log \frac{8a}{b} - \frac{109}{120} \right) - \frac{35}{4194304} \frac{b^8}{a^8} \left(\log \frac{8a}{b} - \frac{431}{420} \right) \right] \quad (D.5)$$

Again the dimensions of inductance and dimensions are in μH and cm, respectively. The second formula takes into account the cross section of the coil. This formula can be found as Equation 88 in [82]. It is repeated below for convenience.

$$L = 4\pi a N^2 (\lambda + \mu) \quad (D.6)$$

Where

$$\lambda = \log \frac{8a}{c} + \frac{1}{12} - \frac{\pi x}{3} - \frac{1}{2} \log (1 + x^2) + \frac{1}{12x^2} \log (1 + x^2) + \\ \frac{1}{12} x^2 \log \left(1 + \frac{1}{x^2} \right) + \frac{2}{3} \left(x - \frac{1}{x} \arctan x \right) \quad (D.7)$$

$$\mu = \frac{c^2}{96a^2} \left[\left(\log \frac{8a}{c} - \frac{1}{2} \log (1 + x^2) \right) (1 + 3x^2) + 3.45x^2 + \frac{221}{60} \right. \\ \left. - 1.6\pi x^3 + 3.2x^3 \arctan x - \frac{1}{10} \frac{1}{x^2} \log (1 + x^2) + \frac{1}{2} x^4 \log \left(1 + \frac{1}{x^2} \right) \right] \quad (D.8)$$

Where c is the thickness of the coil and $x = \frac{b}{c}$. Again the dimensions of inductance and dimensions are in μH and cm, respectively. The resulting value of the self-inductance from equations D.5 and D.6 are 12.018 and 11.967 [mH], respectively. For further comparisons the value from Equation D.6, 11.976 mH, will be used, because this takes into account the cross section of the coil.

E. Anti-symmetry test

To make sure defining no boundary condition result in anti-symmetry a benchmark problem is modelled. In the benchmark two equal wires with opposing currents are modeled, as shown in Figure E.1. This situation has an anti-symmetry axis. To test whether Abaqus can properly account for anti-symmetry two simulations are done. In the first simulation, the full domain is considered, see the right subfigure in Figure E.2. In the first simulation, half of the domain is considered and on the axis of anti-symmetry no boundary conditions are defined, see the left subfigure in Figure E.2. It can be recognized that both the shape and magnitude of the magnetic field are equal.

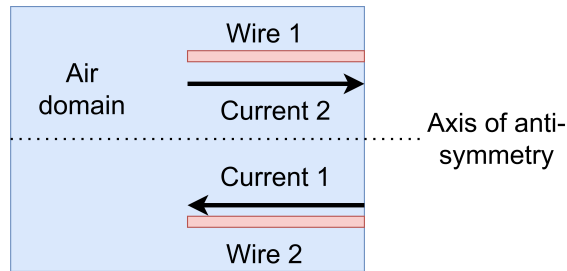


Figure E.1: A schematic overview of the benchmark to test whether Abaqus properly incorporates the anti-symmetry condition.

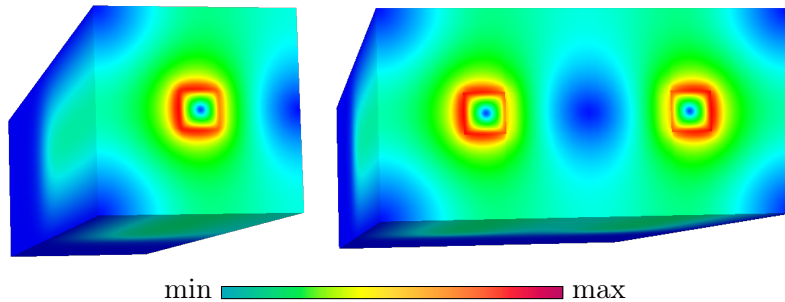


Figure E.2: The magnitude of the magnetic field. For both images, the maximum and minimum magnitude are $3.429e-7$ and $2.707e-12$, respectively.

F. Phasor notation

F.1 Phasor derivation

Before any derivations can be done it will be shown how a time harmonic expression can be expressed in terms of its phasor. This is done using an arbitrary example variable, X . This variable can be defined using

$$\mathbf{X}(x, y, z, t) = \mathbf{X}_1(x, y, z) \sin \omega t + \mathbf{X}_2(x, y, z) \cos \omega t. \quad (\text{F.1})$$

This expression can be simplified as

$$\mathbf{X}(x, y, z, t) = \mathbf{X}_1(x, y, z) \cos(\omega t + \alpha) \quad (\text{F.2})$$

This can be written in Euler form and be rewritten as shown below.

$$\mathbf{X}(x, y, z, t) = X_0(r) \text{Re} \left(e^{j(\omega t + \alpha)} \right) \quad (\text{F.3})$$

$$\mathbf{X}(x, y, z, t) = \text{Re} \left(\mathbf{X}_0(r) e^{j\alpha} e^{j\omega t} \right) \quad (\text{F.4})$$

$$\mathbf{X}(x, y, z, t) = \text{Re} \left(\underset{\sim}{\mathbf{X}}(\mathbf{r}) e^{j\omega t} \right) \quad (\text{F.5})$$

In this case $\underset{\sim}{\mathbf{X}}(\mathbf{r}) = X_0(r) e^{j\alpha}$ is the phasor of the X .

F.2 Power derivation

The goal of this section will be to express the power density in terms of the phasors. This will be done using the example of the dissipated power, P_d , however, the same applies to the magnetically stored energy, W_m . The expression for P_d is given by

$$P_d = \int \sigma |\mathbf{E}(\mathbf{r}, t)|^2 dV \quad (\text{F.6})$$

In this Equation the power density can be defined as, $\mathbf{S}(\mathbf{r}, t)$. Furthermore, page 15 in [36] can be used to obtain $|\mathbf{E}(\mathbf{r}, t)|^2 = \mathbf{E}(\mathbf{r}, t) \cdot \mathbf{E}(\mathbf{r}, t)^*$. This gives the following expression for the power.

$$\mathbf{S}(\mathbf{r}, t) = \mathbf{E}(\mathbf{r}, t) \cdot \mathbf{E}(\mathbf{r}, t)^* \quad (\text{F.7})$$

Writing the terms into phasor notation gives

$$\mathbf{S}(\mathbf{r}, t) = \text{Re} \left[\underset{\sim}{\mathbf{E}}(\mathbf{r}) e^{j\omega t} \right] \cdot \text{Re} \left[\underset{\sim}{\mathbf{E}}(\mathbf{r}) e^{j\omega t} \right]^* \quad (\text{F.8})$$

Using $\text{Re}[X] = \frac{1}{2}[X + X^*]$ gives

$$\mathbf{S}(\mathbf{r}, t) = \frac{1}{2} \left[\underline{\mathbf{E}}(\mathbf{r})e^{j\omega t} + \left[\underline{\mathbf{E}}(\mathbf{r})e^{j\omega t} \right]^* \right] \cdot \frac{1}{2} \left[\underline{\mathbf{E}}(\mathbf{r})e^{j\omega t} + \left[\underline{\mathbf{E}}(\mathbf{r})e^{j\omega t} \right]^* \right] \quad (\text{F.9})$$

Writing all the terms out gives

$$\mathbf{S}(\mathbf{r}, t) = \frac{1}{4} \underline{\mathbf{E}}(\mathbf{r}) \cdot \underline{\mathbf{E}}(\mathbf{r})^* + \frac{1}{4} \underline{\mathbf{E}}(\mathbf{r})^* \cdot \underline{\mathbf{E}}(\mathbf{r}) + \frac{1}{4} \underline{\mathbf{E}}(\mathbf{r}) \cdot \underline{\mathbf{E}}(\mathbf{r}) e^{2j\omega t} + \frac{1}{4} \left[\underline{\mathbf{E}}(\mathbf{r}) \cdot \underline{\mathbf{E}}(\mathbf{r}) e^{2j\omega t} \right]^* \quad (\text{F.10})$$

Again using $\text{Re}[X] = \frac{1}{2}[X + X^*]$ and using the property of the dot product $a \cdot b = b \cdot a$ gives

$$\mathbf{S}(\mathbf{r}, t) = \frac{1}{2} \underline{\mathbf{E}}(\mathbf{r}) \cdot \underline{\mathbf{E}}(\mathbf{r})^* + \frac{1}{2} \text{Re} \left(\underline{\mathbf{E}}(\mathbf{r}) \cdot \underline{\mathbf{E}}(\mathbf{r}) e^{2j\omega t} \right) \quad (\text{F.11})$$

Now it will be shown that the average power of the second term, $\mathbf{S}_{av,2}(\mathbf{r}, t)$, is equal to zero

$$\mathbf{S}_{av,2}(\mathbf{r}, t) = \lim_{T \rightarrow \infty} \frac{1}{T} \int_0^T \frac{1}{2} \text{Re} \left(\underline{\mathbf{E}}(\mathbf{r}) \cdot \underline{\mathbf{E}}(\mathbf{r}) e^{2j\omega t} \right) dt \quad (\text{F.12})$$

$$\mathbf{S}_{av,2}(\mathbf{r}, t) = \underline{\mathbf{E}}(\mathbf{r}) \cdot \underline{\mathbf{E}}(\mathbf{r}) \lim_{T \rightarrow \infty} \frac{1}{T} \int_0^T \frac{1}{2} \cos(2\omega t) dt \quad (\text{F.13})$$

$$\mathbf{S}_{av,2}(\mathbf{r}, t) = 0 \quad (\text{F.14})$$

This knowledge can be used to obtain the new expression for the power.

$$\mathbf{S}(\mathbf{r}, t) = \frac{1}{2} \underline{\mathbf{E}}(\mathbf{r}) \cdot \underline{\mathbf{E}}(\mathbf{r})^* \quad (\text{F.15})$$

G. The electrical circuit

G.1 The hardware

In Figure G.1 an overview is shown of the electrical hardware used in the experiments. The idea is that the current from the coils goes back to the voltage generator (indicated as Osc on the board). Another port measures the voltage over a 1 ohm resistor which will give the current in the transmitting coil. It has been observed that the location of this

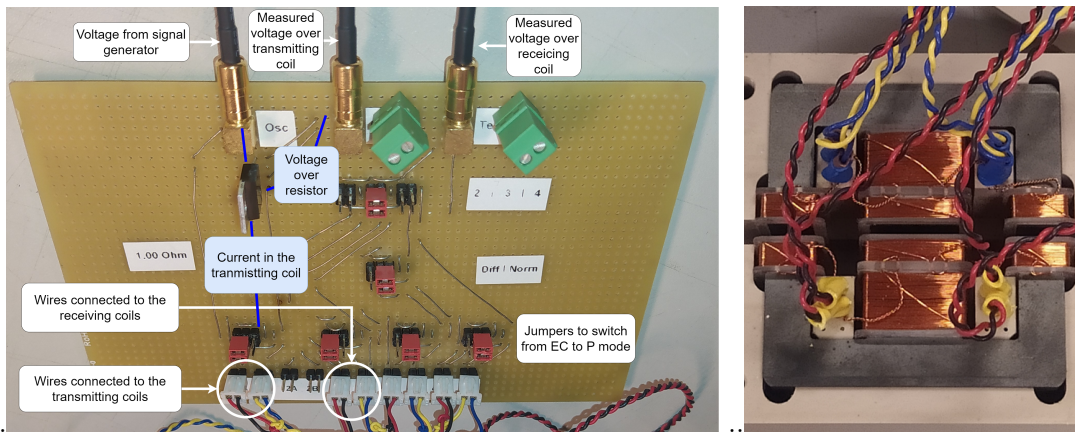


Figure G.1: The electrical circuit used in the experiments (left). The sensor used in the experiments (right).

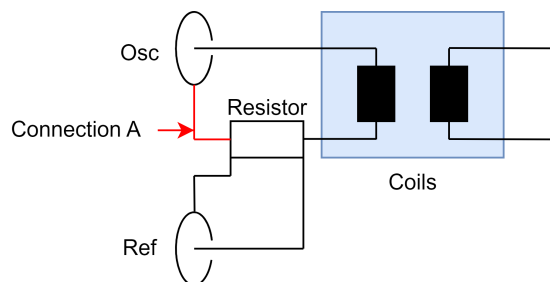


Figure G.2: A schematic diagram illustrating the location of the connection which should be carefully considered.

resistor is very important. The reason is that if the wired connection from the resistor to the signal output port Osc (Connection A in Figure G.2) is too long this will cause a significant inductance (in the order of hundreds of nH). This will lead to part of the current going through the REF port. This will cause a shift in phase of the measured signal over the resistor. To prevent this effect the resistance in Connection A should be made as low as possible. This can be done by for example reducing the length of the connection.

G.2 Deriving the transfer function

The approach to find the equivalent electrical circuit is based on the work done by Peter Bax and Shiyu Feng in [44]. The initial circuit of the sensor set-up is shown in the left side of Figure G.3. The circuit is shorted, which means perfect coupling is assumed. This is a rather big assumption and unlikely to be fully accurate.

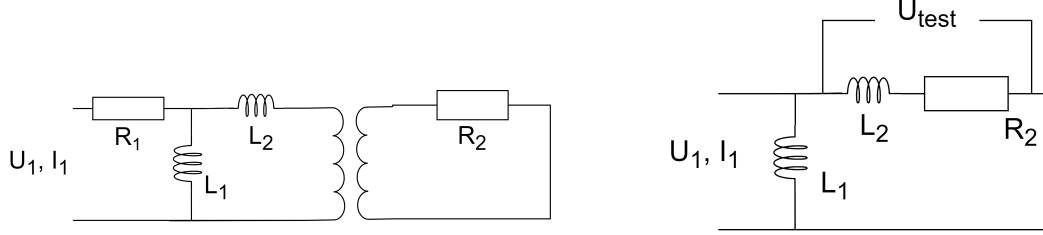


Figure G.3: The initial equivalent circuit (left) the final equivalent electrical circuit (right).

The transfer function can then be derived using Kirchoffs laws. These are given below

$$U_1 = j\omega L_1(I_1 - I_2) \quad (\text{G.1})$$

$$R_2 I_2 + I_2 j\omega L_2 + (I_2 - I_1)j\omega L_1 = 0 \quad (\text{G.2})$$

First, equation G.2 is used to isolate I_1 , which gives

$$I_1 = \frac{1}{j\omega L_1} (j\omega L_1 I_2 + j\omega L_2 I_2 + R_2 I_2) \quad (\text{G.3})$$

Using $I_2 = U_{test}/(R_2 + j\omega L_2)$ to remove I_2 and rewriting gives

$$I_1 = U_{test} \frac{1}{j\omega L_1 (R_2 + j\omega L_2)} (j\omega [L_1 + L_2] + R_2) \quad (\text{G.4})$$

Using that U_{ref} is equal to the I_1 means the equation can be written as

$$\frac{U_{test}}{U_{ref}} = \frac{j\omega L_1 (R_2 + j\omega L_2)}{j\omega (L_1 + L_2) + R_2} \quad (\text{G.5})$$

H. Fitting simulated curves

In this section some problems about the fitting techniques are highlighted. In Figure H.1 it can be seen least square curve fitting gives poor results. This is caused by the fact that the equivalent circuit model does not describe all the occurring phenomena well enough. The same can be observed in Figure H.3 in which there are two minima in the phase. These can not be described by the simple equivalent electrical circuit model.

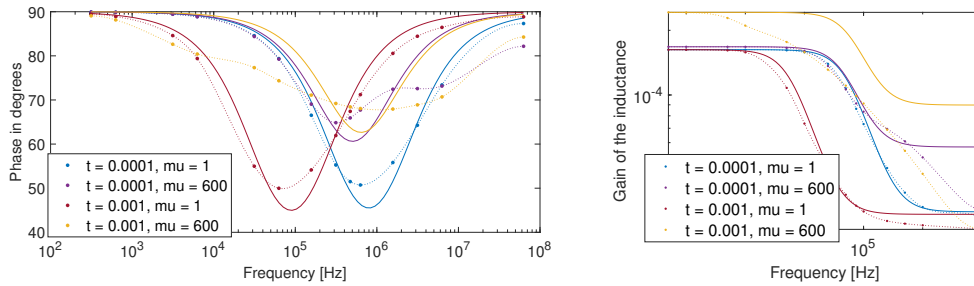


Figure H.1: Figure showing the the fit when done with least squares curve fitting.

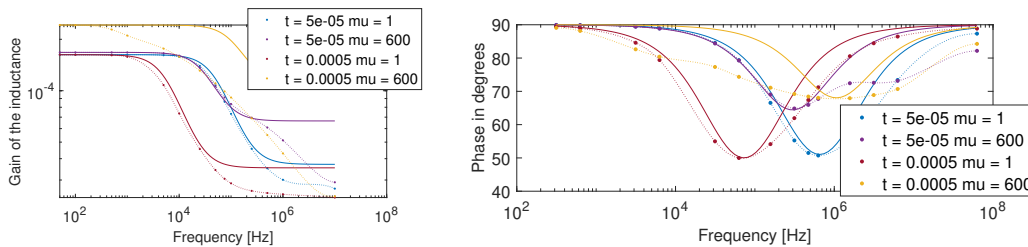


Figure H.2: The differences between the fit of the electrical circuit and the fem model.

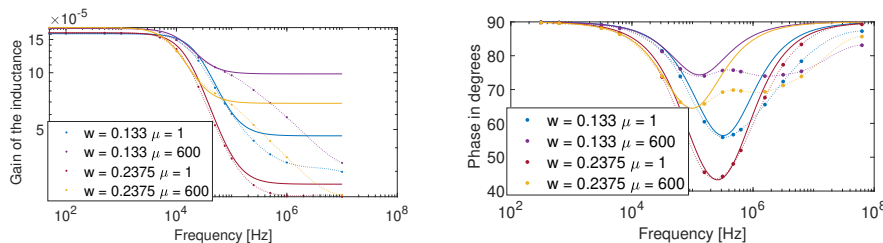


Figure H.3: The differences between the fit of the electrical circuit and the fem model.

I. Sensor signal interpretation

In the experiments the sensor signal exists out of two signals. These will be defined as the gain of the inductance, G , and the phase of inductance, θ . In the experimental set-up the two signals are determined by measuring the voltage in the receiving coil, \mathcal{U}_{rec} , and the current in the transmitting coil, $\mathcal{I}_{\text{trans}}$. The equations that are used to calculate the signal values are

$$G = \left| \frac{\mathcal{U}_{\text{rec}}}{\mathcal{I}_{\text{trans}}} \frac{1}{\omega} \right| \quad \theta = \angle \mathcal{U}_{\text{rec}} - \angle \mathcal{I}_{\text{trans}} \quad (\text{I.1})$$

This means the results from Section 2.6 must be converted to receiver voltage and transmitter current. The voltage in the receiver can be calculated in accordance with Equation 2.10 which gives

$$\mathcal{U}_{\text{rec}} = -\mathcal{M}_c \omega j. \quad (\text{I.2})$$

Obtaining the current for the transmitter from the simulations is less straightforward. The reduced current of the transmitter in the model can be calculated using the electromotive force as

$$\mathcal{I}_{\text{transmitter}} = \mathcal{I}_{0,\text{transmitter}} + \mathcal{E}MF/\mathcal{R}. \quad (\text{I.3})$$

The resistance of the coil, $R = l/A\sigma$, is very high because the conductivity of the coils was set to 1 [S/m]. This means the induced currents in the transmitter in the simulations are negligible. For this reason the second term can be dropped. This can be used together with the fact that a current of 1A is applied to obtain.

$$G = \left| \frac{-\mathcal{M}_c \omega j}{1} \frac{1}{\omega} \right| = \mathcal{M}_c \quad \theta = \angle -\mathcal{M}_c \omega j - 0 = \angle \mathcal{M}_c - 90^\circ \quad (\text{I.4})$$